

# **Bioparticle Separation in Microfluidic Devices**

for in-Line Application



# **Bioparticle Separation in Microfluidic Devices**

## for in-Line Application

Proefschrift

ter verkrijging van de graad van doctor  
aan de Technische Universiteit Delft,  
op gezag van de Rector Magnificus Prof. dr. ir. J.T. Fokkema,  
voorzitter van het College voor Promoties,  
in het openbaar te verdedigen  
op vrijdag 20 november 2009 om 10.00 uur  
door

Lujun ZHANG

Master of Science  
Royal Institute of Technology, Stockholm, Sweden  
Bachelor of Engineering  
Tongji University, Shanghai, China  
geboren te Shanghai, China

Dit proefschrift is goedgekeurd door de promotor:

Prof. dr. P.J. French

Copromotor:

Dr. ir. A. Bossche

Samenstelling promotiecommissie:

Rector Magnificus	voorzitter
Prof. dr. P.J. French	Technische Universiteit Delft, promotor
Dr. ir. A. Bossche	Technische Universiteit Delft, copromotor
Prof. dr. P.M. Sarro	Technische Universiteit Delft
Prof. dr. ir. A. van den Berg	Universiteit Twente
Prof. dr. ir. M.J. Vellekoop	Vienna University of Technology
Prof. dr. P.D.E.M. Verhaert	Technische Universiteit Delft
Prof. dr. ir. J. Westerweel	Technische Universiteit Delft

Reservelid:

Prof. dr. K.A.A. Makinwa	Technische Universiteit Delft
--------------------------	-------------------------------

Het onderzoek beschreven in dit proefschrift is financieel ondersteund door de Stichting voor Technische Wetenschappen (STW).

ISBN 978-90-813316-7-8

Copyright © 2009 by L. Zhang

All rights reserved. No part of the material protected by this copyright notice may be reproduced or utilized in any form or by any means, electronic or mechanical, including photocopying, recording or by any information storage and retrieval system, without the prior permission of the author.

Printed in the Netherlands

Dedicated to my parents, and my wife *Jinghua Tang*



# Contents

<b>1</b>	<b>Introduction</b>	<b>1</b>
1.1	Motivation and objectives . . . . .	1
1.2	Organization of this thesis . . . . .	2
<b>2</b>	<b>Theoretical Background</b>	<b>5</b>
2.1	Low Reynolds number flows . . . . .	5
2.2	Electrokinetics . . . . .	6
2.2.1	Electrical double layer . . . . .	6
2.2.2	Electroosmosis . . . . .	8
2.2.3	Electrophoresis . . . . .	9
2.2.4	AC electroosmosis . . . . .	10
2.2.5	Dielectrophoresis . . . . .	10
2.3	Bioparticle separation on microfluidic chips . . . . .	13
2.3.1	Capillary electrophoresis . . . . .	13
2.3.2	Dielectrophoretic separation . . . . .	15
2.3.3	Magnetophoretic separation . . . . .	22
2.3.4	Acoustophoretic separation . . . . .	23
2.3.5	Separation via optical forces . . . . .	25
<b>3</b>	<b>Dielectrophoretic Separation in Iterative Curves</b>	<b>27</b>
3.1	Separation in a curve . . . . .	28
3.1.1	Using a DC electric field . . . . .	28
3.1.2	Using a DC-biased AC electric field . . . . .	31
3.1.3	Separation resolution . . . . .	36

3.2	Concept of the design . . . . .	41
3.3	Particle focusing . . . . .	41
3.3.1	Requirements and options . . . . .	41
3.3.2	Slanted planar electrode arrays . . . . .	43
3.3.3	Top-and-bottom electrode pairs . . . . .	50
3.4	Electro-kinetic DEP separation in iterative curves . . . . .	52
3.4.1	Comparison of focusing schemes . . . . .	53
3.4.2	Simulation results . . . . .	54
3.5	Discussions . . . . .	56
3.5.1	First focusing segment . . . . .	56
3.5.2	Sample plug profile . . . . .	57
3.5.3	Thickness of the insulating film . . . . .	58
3.5.4	AC perturbation on the flow . . . . .	61
3.5.5	Induced charge electroosmosis . . . . .	63
3.5.6	Heterogeneous $\zeta$ -potential . . . . .	64
3.6	Hydrodynamic DEP separation in iterative curves . . . . .	66
3.6.1	Flow profile comparison . . . . .	66
3.6.2	Design principle . . . . .	66
3.6.3	Simulation results . . . . .	67
<b>4</b>	<b>Moving Field Capillary Electrophoresis</b>	<b>71</b>
4.1	Plug dispersion in moving field CE . . . . .	71
4.2	Electrical analogy of fluid system . . . . .	75
4.3	Compensation by an electroosmotic pump . . . . .	76
4.4	Relief of the pump voltage . . . . .	80
4.4.1	By well-designed channel structures . . . . .	80
4.4.2	By gate electrodes . . . . .	83
4.5	Prevention of flow loss . . . . .	86
4.6	Constant electric fields versus dynamic electric fields . . . . .	91
4.7	Single-side electrodes versus double-banked electrodes . . . . .	91
4.8	Flow distortion above floating electrodes . . . . .	92
4.9	Gas venting . . . . .	93
4.10	Moving field CE system . . . . .	94



<b>5</b>	<b>Biomass Concentration Detection</b>	<b>97</b>
5.1	Introduction . . . . .	97
5.2	Design principle . . . . .	98
5.3	Viable yeast cell trapping . . . . .	99
5.3.1	Model of the yeast cell . . . . .	99
5.3.2	Induced dipole strength calculation . . . . .	100
5.3.3	Dielectrophoretic trapping . . . . .	103
5.4	Contactless 4 electrode detection . . . . .	104
5.4.1	Electrical model of the detector . . . . .	106
5.4.2	Readout circuits . . . . .	106
5.4.3	Measurement setup . . . . .	108
<b>6</b>	<b>Device Fabrication</b>	<b>109</b>
6.1	Standard processes . . . . .	109
6.1.1	Layer deposition . . . . .	109
6.1.2	Plasma etching . . . . .	110
6.1.3	Photolithography . . . . .	110
6.2	Materials used . . . . .	111
6.2.1	Glass wafer . . . . .	111
6.2.2	Titanium . . . . .	112
6.2.3	Silicon dioxide . . . . .	112
6.2.4	Dry film resist . . . . .	112
6.2.5	SU-8 . . . . .	114
6.3	Rapid prototyping of the moving field CE device . . . . .	115
6.3.1	Process flow . . . . .	115
6.3.2	Critical processing steps . . . . .	118
6.3.3	Fabrication results . . . . .	118
6.3.4	Hydraulic pressure test . . . . .	118
6.4	Fabrication of the DEP device . . . . .	120
6.4.1	Process flow . . . . .	120
6.4.2	Critical processing steps . . . . .	122
6.4.3	Fabrication results . . . . .	125

<b>7</b>	<b>Experimental Results</b>	<b>129</b>
7.1	Device holder . . . . .	129
7.2	Experiments on the DEP device . . . . .	129
7.2.1	Measurement setups . . . . .	129
7.2.2	Dielectrophoretic focusing . . . . .	132
7.2.3	Dielectrophoretic repelling in the curve . . . . .	132
7.2.4	Measured separation . . . . .	134
7.3	Experiments on the moving field CE device . . . . .	137
7.3.1	Measurement setups . . . . .	137
7.3.2	Measured flow distortion compensation . . . . .	137
<b>8</b>	<b>Conclusions and Future Work</b>	<b>141</b>
8.1	Conclusions . . . . .	141
8.2	Future work . . . . .	143
8.2.1	DEP separation in iterative curves . . . . .	143
8.2.2	Moving field CE . . . . .	144
8.2.3	Biomass concentration detecton . . . . .	144
8.2.4	System integration . . . . .	144
	<b>Bibliography</b>	<b>147</b>
	<b>Summary</b>	<b>155</b>
	<b>Samenvatting</b>	<b>157</b>
	<b>Acknowledgements</b>	<b>159</b>
	<b>List of Publications</b>	<b>161</b>
	<b>About the author</b>	<b>165</b>

# Chapter 1

## Introduction

### 1.1 Motivation and objectives

There was an explosive growth in the bioprocess industry market during the last decade. The tight control of these processes is often very critical in order to optimize the process efficiency (the quantity and quality of products) or even achieve the right product. For instance, protein characterization of beer during fermentation is very useful in quality control, since proteins and peptides in beer are responsible for nutritional value and stability of beer. There is an increasing need for fast, reliable and inexpensive analytical techniques, which can operate without supervision and outside laboratory facilities. Specifically in the bioprocess industry there is a need for continuous monitoring of relevant analytes with minimal sample and reagent consumption.

Therefore, our ultimate goal is to develop a working prototype of a chip-based self-supporting analytical system, capable of clean-up, separating and detecting mixtures of well-defined analytes. The system will consist of a sampling and sample pre-treatment unit, a separation unit and a detection unit. And the system will be optimized for a particular application and be capable of running that application only.

Until now many analytical techniques have been developed for monitoring bioprocess. Biosensors [1–3] used for monitoring single chemical compounds are limited to a few specific applications. (e.g. for oxygen or glucose detection). Spectroscopy [4, 5] is capable of monitoring a couple of specified compounds during the process run, however it is still not enough for understanding the process. High performance liquid chromatography (HPLC) has been critically discussed in the literature [6, 7] as it appears not to be appropriate for real time process control.

As a powerful separation technique widely used for biochemical analysis [8–11],

Capillary Electrophoresis (CE) might be a potential candidate to perform the separation in the analytical system. However, CE has only been used in laboratory situations for off-line measurements until now. It still hasn't found its way to inline application, not even after the microchip CE was developed. One of the major barriers hindering its way to inline application is the high separation voltages required (1500-3000 V). The objective of this project is to develop a new separation method which could perform batch separation and compound analysis as well as CE but does not suffer from the high separation voltage requirements. With lower separation voltages, the separation unit will get more easily integrated with the detection unit and the readout electronics. And it might also be possible to integrate the voltage generator within a small volume with commercially available components.

## 1.2 Organization of this thesis

This thesis mainly deals with the investigation and development of new separation methods that can be used for industrial in-line application.

In Chapter 2, the fundamental theories on the microfluidics are introduced with an emphasis on the electrokinetics. Subsequently, the bioparticle separation methods that are most commonly used on microfluidic chips are reviewed.

Chapter 3 proposes a particle batch separation in iterative curves, based on dielectrophoresis (DEP). The curve where the dielectrophoretic separation occurs is firstly investigated in the presence of a DC electric field and a DC biased AC electric field, respectively. It is presented that the separation sensitivity can be significantly increased by applying a DC biased AC electric field with a large ratio of AC to DC amplitudes. To bring all the particles to an equal entering point for the next curve, focusing segments are required between successive curves. Two different electrode configurations are investigated with respect to their focusing performance. The results of particle tracing for both electrokinetic and hydrodynamic DEP separation in the iterative curves are also presented in this chapter.

To relieve the high voltage requirement of the traditional CE, the moving field CE is proposed in Chapter 4. This method is based on the fact that the electric field will be still sufficiently strong when a low voltage is applied over electrodes with very small spans. However, applying a voltage over a fraction of the channel induces plug dispersion. This chapter explains the reason why plug dispersion occurs and deals with a plug dispersion compensation technique which involves the coupling of an electroosmotic pump (EOP). Aspects regarding the relief of EOP driving voltage, flow loss prevention, electrode configuration, and gas venting are discussed. The concept of a complete CE system is described at the end of this chapter.

Chapter 5 proposes a biomass concentration detector for the monitoring of the

fermentation process. Based on the simplified homogeneous sphere model, the frequency dependence of the induced dipole strength of the yeast cell is studied by computer methods. The threshold DEP forces required to dominate over the Brownian motion for cell trapping is investigated. To achieve accurate and sensitive detection, a contactless 4-electrode conductivity detector is recommended to be used.

Chapter 6 mainly introduces two different fabrication processes for the DEP device and the moving field CE device, respectively. It is presented that the DEP device containing top-and-bottom microelectrodes is formed by the bonding of two processed substrates together with an SU-8 layer sandwiched in between. A rapid method of prototyping the moving field CE device is described, which is conducted by using a dry film lamination technique.

Chapter 7 contains the experimental results. The experimental setups for the two proposed separation methods are described, respectively. The measured retention time for 2  $\mu\text{m}$  and 4  $\mu\text{m}$  polystyrene particles in the DEP device is presented. The 4  $\mu\text{m}$  particles turn out to take an average 10% longer retention time than the 2  $\mu\text{m}$  particles. The measured flow distortion compensation for the moving field CE device is also presented in this chapter.

In the last chapter of the thesis, Chapter 8, the conclusions of the presented work are drawn and the suggestions for future work are given.



# Chapter 2

## Theoretical Background

### 2.1 Low Reynolds number flows

Flow in channels generally can be classified as a laminar flow regime, a turbulent flow regime, or a transition flow regime. In the laminar flow regime, the flow is dominated by the viscous effect and the fluid stream follows regular paths. In the turbulent flow regime, the unsteady flow stream is mainly determined by inertial but also viscous effects. The region between the laminar and turbulent flow is called the transition region, where the unsteady laminar flow is observed with both viscous and inertial energy dissipation effects.

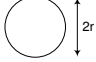
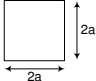
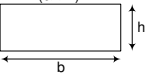
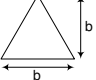
The ratio of the inertial force density to the viscous force density, known as the Reynolds number, is normally used to identify the regime of the flows.

$$Re = \frac{\rho v D}{\eta} \quad (2.1)$$

where  $D$  is the hydraulic diameter of the channel,  $v$  is the characteristic flow velocity,  $\rho$  is the mass density of the fluid, and  $\eta$  is the viscosity of the fluid. When the  $Re$  is lower than 1000, the flow in the channel is laminar. In this regime there is a linear relation between the pressure drop over the channel and the flow rate in the channel. When the  $Re$  is above 2000, the flow in the channel is turbulent and there is no longer a linear relation between the pressure drop and the flow rate. When the  $Re$  is between 1000 and 2000, the flow is in the transition regime.

In the laminar flow regime, the linear relation between the pressure drop ( $\Delta P$ ) over the channel and the flow rate ( $Q$ ) in the channel takes this formula  $\Delta P = R_{fl} Q$ , where  $R_{fl}$  is the flow resistance of the channel. For various channel cross-sections, the flow resistance of the channel can be calculated as listed in Table 2.1.

Table 2.1: Flow resistance and hydraulic diameter of various channel cross-sections in the laminar flow regime.

Channel cross-section	Flow resistance ( $Nsm^{-5}$ )	Hydraulic diameter $D_h$ (m)
	$\frac{8\eta L}{\pi r^4}$	$2r$
	$\frac{1.78\eta L}{a^4}$	$2a$
	$\frac{12\eta L}{bh^3}$	$2h$
	$\frac{17.4\eta L}{(b/2)^4}$	$0.52b$

## 2.2 Electrokinetics

Among all non-mechanical fluid manipulation techniques in microfluidic regimes, electrokinetics is almost the most widely used. Historically, early microfluidic devices were designed for capillary electrophoretic separation, where the electroosmotic flow (EOF) was used to pump as well as to separate. In this section, the basic physics of electrokinetics will be introduced.

### 2.2.1 Electrical double layer

A solid surface in contact with an electrolyte will introduce a surface charge depending on the characteristics of both the solid and the liquid. For instance, at the interface between a glass surface and a liquid such as water, silanol molecules ( $\text{SiOH}$ ) on the glass surface react with free hydroxyl ions ( $\text{OH}^-$ ) in the water, forming  $\text{Si}(\text{OH})_2^-$  and leaving the glass surface negatively charged. Ions charged oppositely to the surface, so-called counter-ions, are attracted towards the wall, while co-ions having the same charge as the surface are repelled from the surface. The local region near the surface with a net charge associated to it is referred to as the Electrical Double Layer (EDL).

The EDL consists of two layers (Figure 2.1): an inner layer (i.e. stern layer) which includes ions bound strongly to the surface and an outer layer (i.e. diffuse layer) in which the ion distribution is determined by a balance of electrostatic forces and random thermal motion. Therefore, the potential in this region decays as the distance from the surface increases until, at sufficient distance, it reaches the bulk solution value, conventionally taken to be zero. The characteristic thickness of the



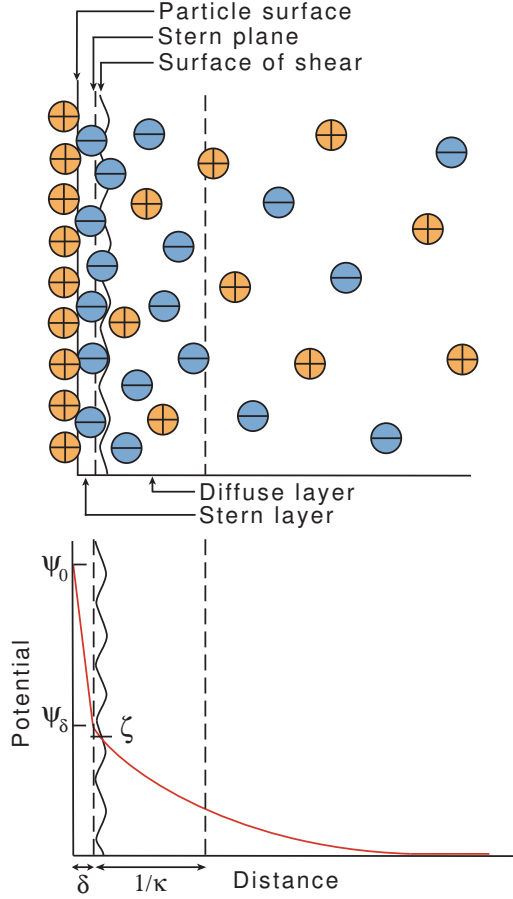


Figure 2.1: Electrical double layer.

EDL is called the Debye length and is given by the inverse of the Debye-Huckel parameter [12]

$$\lambda_D = \frac{1}{\kappa} = \sqrt{\frac{\varepsilon k_b T}{2z^2 e^2 n_\infty}} \quad (2.2)$$

with  $\kappa$  as the Debye-Huckel parameter,  $\varepsilon$  the permittivity of the liquid,  $k_b$  the Boltzmann constant,  $T$  the absolute temperature,  $z$  the valence of ion,  $e$  the charge of an electron, and  $n_\infty$  the background concentration of ions. Typically, the Debye length is in the range of 1-100 nm.

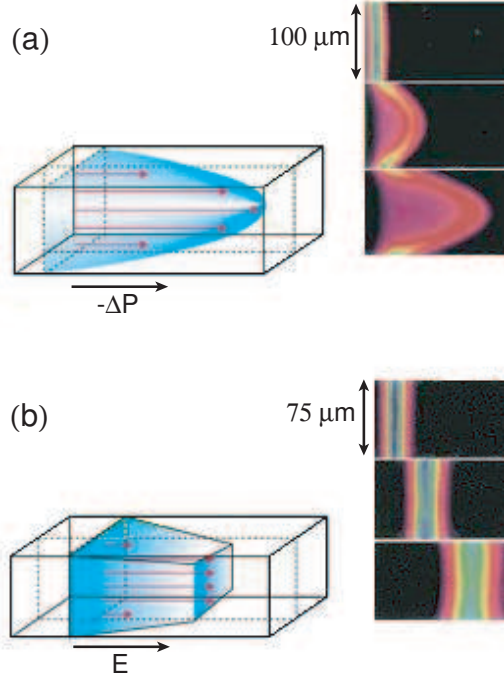


Figure 2.2: Illustration of a fundamental difference between pressure driven flow and electroosmotic flow. The fluorescent images on the right side show the reduced sample dispersion for (b) electroosmotic flow as compared to (a) pressure-driven flow.

### 2.2.2 Electroosmosis

When an external electric field  $E$  is applied along a charged surface, the ions in the diffuse layer gives rise to an electric body force also tangent to the surface. Viscous interactions between these ions and the fluid in the channel results in net fluid flow with a velocity that varies linearly with the applied field  $E$ .

$$v_{eof} = -\frac{\varepsilon\zeta}{\eta}E \quad (2.3)$$

where  $\zeta$  is the potential drop over the diffuse layer known as the zeta potential. In practise, zeta potentials are usually negative, i.e. the surface is negatively charged, but they can lie anywhere in the range from -100 to +100 mV.

Most microfluidic systems rely on two modes of fluid transport: pressure-driven flow and electroosmotic flow. Electroosmotic flow is more widely used in microfluidic chips because of its several advantages over pressure driven flow. Chiefly,

electroosmotic flow produces a nearly uniform flow profile, which results in reduced sample plug dispersion as compared to the velocity gradients associated with pressure-driven flow. The comparison between pressure-driven flow and the electroosmotic flow is demonstrated in Figure 2.2. In electroosmotic flow systems, fluid pumping and valving can be controlled without moving parts and simple devices are capable of a large variety of processes including mixing, molecular separation, and the generation of pressure work. Ease of fabrication allows for the rapid development of system design concepts and evolution in the functionality of electroosmotic flow systems.

### 2.2.3 Electrophoresis

Electrophoresis is the migration of colloidal particles or molecules suspended in liquid solution under the influence of an applied electric field. Electrophoresis occurs because particles dispersed in liquid almost always carry an electric surface charge. According to double layer theory, a diffuse layer with counter-ions will be formed around the particle. The movement of the diffuse layer under the influence of the electric field will exert a force to the particle surface through viscous stress. This force is called electrophoretic retardation force. The electrophoretic velocity of the particles is a function of the electrostatic force on the surface charge, the fluid friction force, and the electrophoretic retardation force. For a wide range of cases where the particle diameter-to-Debye length ratio is large so that, locally, the ionic cloud near the particle surface can be approximated by the EDL relations for a flat plate, the velocity of an electrophoretic particle will be

$$v = \frac{\varepsilon\zeta E}{\eta} \quad (2.4)$$

For the electrophoresis of ions and molecules whose characteristic diameter are much smaller than the Debye length of the solution, the electrophoretic retardation force can be negligible. The motion of these molecules can be described as a simple balance between the electrostatic force and the fluid drag force on the molecule. As a result, the electrophoretic mobility of molecules is a function of the molecule's charge and size.

$$v = \frac{qE}{6\pi\eta R_p} \quad (2.5)$$

where  $q$  is the total charge on the molecule,  $E$  is the applied electric field, and  $R_p$  is the radius of the molecule.

## 2.2.4 AC electroosmosis

It has been demonstrated that nonuniform AC electric fields generated by a pair of co-planar microelectrodes produce a steady fluid flow in electrolytes [13–15]. The fluid moves from the highest field regions on the edges of the electrodes onto the surface of the electrodes. A schematic diagram of the mechanism of AC electroosmosis is depicted in Figure 2.3a. At a certain time, the situation is as shown in the figure: the induced charges accumulate in the diffuse double layer with a sign opposite to the electrode charge. Subjecting to the tangential component of the electric field, the charges migrate from the center of the gap onto the electrode surface, which in turn produces fluid motion due to fluid viscosity. Because charges in the double layer and electric field change signs simultaneously, AC electroosmosis produces two steady, counter-rotating local vortices above the electrode pair as can be seen in Figure 2.3b.

Nadal and co-workers [16] studied the electroosmosis slip velocity and the size of the roll-cells established in the vicinity of microelectrodes for AC fields. It was revealed that the electroosmosis vanishes at both very low and very high frequencies. At very low frequencies, the double layer capacitance formed by the ions in the electrolyte will screen out the electric field in the bulk fluid. At high frequency, the free charge density vanishes due to the finite diffusion time required to build up the diffuse layer.

## 2.2.5 Dielectrophoresis

Dielectrophoresis (DEP) is the movement of the particle induced by a non-uniform electric field. When a particle is subjected to an electric field, the particle becomes polarized along the direction of the electric field. In a non-uniform electric field, the electrostatic forces on opposite ends of the particle are different and the net force results in movement of the particle. If the electrical polarizability of the particle is larger than that of the surrounding medium, the particle moves towards the high intensity field region, which is called positive dielectrophoresis (pDEP). If, on the contrary, the polarizability of the particle is lower than that of the surrounding medium, the particle moves towards the low intensity field region, which is called negative dielectrophoresis (nDEP). The time-averaged dielectrophoretic force acting on a spherical particle, immersed in a medium and exposed to a spatially non-uniform electric field can be described by

$$\langle \vec{F}_{DEP} \rangle = 2\pi\epsilon_m R_p^3 \text{Re}[K(\omega)] \nabla |\vec{E}_{rms}|^2 \quad (2.6)$$

where  $|\vec{E}_{rms}|^2$  is the root mean square value of the electric field squared,  $\epsilon_m$  is the permittivity of the suspending medium,  $R_p$  is the radius of the particle, and

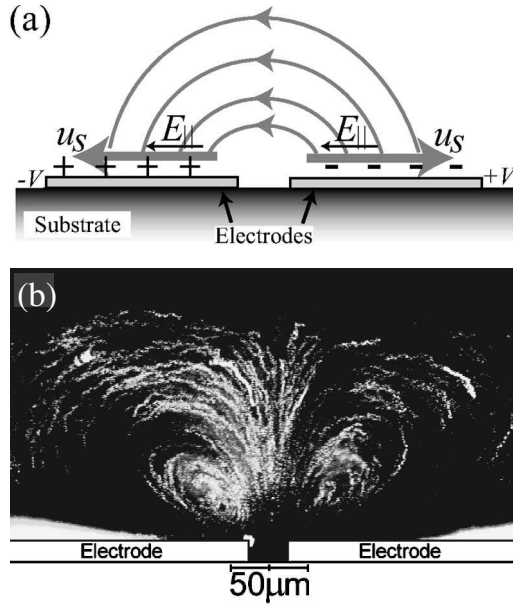


Figure 2.3: AC electroosmosis over coplanar electrodes (adapted from [17]). (a) A schematic diagram of mechanism. (b) Image of particle track over time in the AC electroosmosis, obtained by superimposing successive video frames from footage of fluid flow.

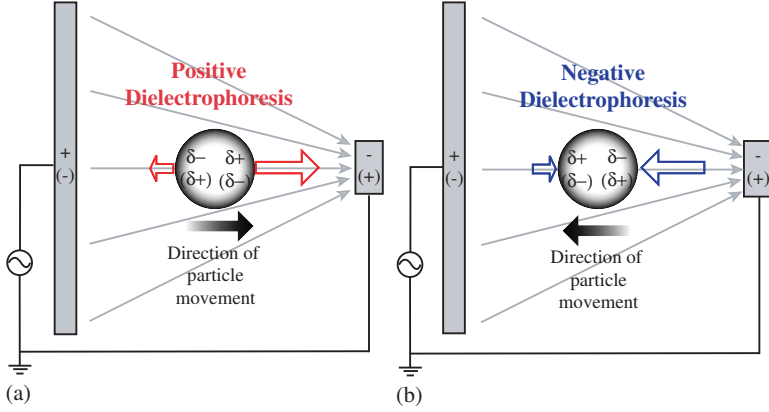


Figure 2.4: Principle of dielectrophoresis, direction of molecule movement depends on DEP response: (a) positive DEP and (b) negative DEP.

$$K(\omega) = \frac{\varepsilon_p^* - \varepsilon_m^*}{\varepsilon_p^* + 2\varepsilon_m^*} \quad (2.7)$$

$K(\omega)$  is the frequency dependent Clausius-Mossotti (CM) factor,  $\varepsilon_p$  and  $\varepsilon_m$  represent the frequency dependent complex permittivities of the particle and medium, respectively, The complex permittivity is defined as  $\varepsilon^* = \varepsilon + \sigma/(j\omega)$ , where  $j = \sqrt{-1}$ ,  $\varepsilon$  is the permittivity, and  $\sigma$  is the conductivity of the dielectric.

The Clausius-Mossotti factor not only depends on the dielectric properties of the particle and medium, but also on the frequency of the applied field. Variations in this factor give rise to a dielectrophoretic force that is frequency dependent and unique to a particular particle type. For a sphere, the real part of  $K(\omega)$  is bounded by the limits  $-0.5 < \text{Re}[K(\omega)] < 1$  and varies with the frequency of the applied field and the complex permittivity of the medium. Positive DEP occurs when  $\text{Re}[K(\omega)] > 0$ , the force is toward the high electric field (Figure 2.4a). The converse of this is negative DEP, which occurs when  $\text{Re}[K(\omega)] < 0$ , the force is in the direction of decreasing field intensity (Figure 2.4b).

The use of electrophoresis is related to the manipulation of charged particles under the influence of a DC source and is able to manipulate the particles by using their particular charges. DEP, on the other hand, has attracted more attention because it uses AC, non-uniform electric fields and the materials electric polarizability rather than its net charge to apply manipulating forces, and thus it is applicable to a broader range of materials, including particles without charges in an aqueous solution.

## 2.3 Bioparticle separation on microfluidic chips

Modern particle separation techniques have been fundamental to many advances in cell biology, molecular genetics, biotechnological production, clinical diagnostics, and therapeutics. A number of macroscale methods have been developed to separate particles, including the ubiquitous techniques of filtration, centrifugation, electrophoresis, and both fluorescence-(FACS) and magnetic-activated-cell sorting (MACS), taking advantage of differences in particle size, density, electrical charge, and specific immunological surface markers.

Microfluidic chips have proven ideal tools to precisely and instantly handle small volumes of samples, such as protein or DNA solutions, as well as cell suspensions. In the micro total analysis systems (microTAS) an entire analytical procedure needs to be performed including sample pre-treatment, labelling reactions, separation, downstream reactions and detection. An effective and precise separation is a key factor to realize this ideal case. A large variety of separation methods has been reported, some of them are miniaturized version of larger scale methods, and others are only possible in microfluidic regimes. Particularly, the use of electric fields has attracted significant attention for applications in the separation of bioparticles. Therefore, two main electrokinetic techniques electrophoresis and dielectrophoresis will be emphatically introduced. Moreover, the non-electrokinetic separation methods will be introduced subsequently as well.

### 2.3.1 Capillary electrophoresis

Capillary electrophoresis (CE), also known as capillary zone electrophoresis (CZE), is a powerful analytical technique which has been implemented into many important analytical processes including genetic analysis, pharmaceutical analysis, bioprocess monitoring, ion analysis and complex protein characterization. The separation principle is based on the phenomena that ionized molecules of different mass and charge will travel with different velocities through a capillary under the influence of strong electric field. The CZE separation process is illustrated in Figure 2.5. There are some other related techniques encompassed in the CE family, such as Capillary Gel Electrophoresis (CGE), Isotachopheresis (ITP), Electrokinetic Chromatography (EKC), Micellar Electrokinetic Capillary Chromatography (MEKC), Micro Emulsion EKC (MEEKC), and Non-Aqueous CE (NACE).

Among those CZE is one of the most widely used techniques. The separation is carried out in capillaries filled with a buffer solution. The capillaries normally consist of fused silica are typically several to several tens centimeter long with a diameter of 25 to 100  $\mu\text{m}$ . Due to the small size of CE capillaries, convection is hindered in CE. Thus field strengths up to 1 kV/cm can be used during operation. The sample is injected to the separation column through the sample reservoir. Under the influence of the applied voltage, the analytes migrate towards the

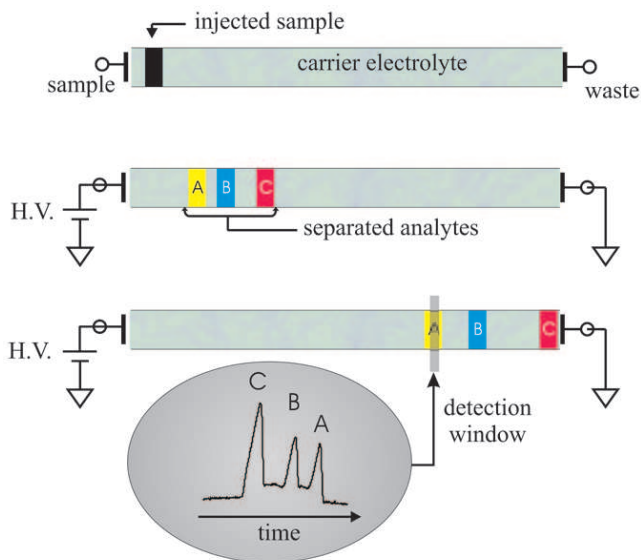


Figure 2.5: Capillary zone electrophoresis: injection, separation, and detection.

waste reservoir and form different zones due to their different mobilities. The detection window at the end of the separation column measures the amount of analytes in the different zones which arrives sequentially. In the electropherogram, the amplitude of the peaks is related to the amount of the analytes, and the species of the analyte are identified by the times at which the peaks occur.

The electrophoretic mobility of the analyte depends on the electrical force moving the molecule forward and the frictional force slowing it down. By balancing these two forces, the electrophoretic mobility can be described as

$$\mu_e = \frac{q}{6\pi r\eta} \quad (2.8)$$

where  $q$  is the ion charge,  $r$  is the ion radius, and  $\eta$  is the solution viscosity. However, the movement of the analyte through the capillary is not just due to its electrophoretic mobility. Migration also has a component from the electroosmotic flow in the capillary. This arises because of a build up of cations near the negatively charged silica wall. Under the influence of an applied electric field, these cations move through the capillary and drag buffer behind them. This results in a bulk movement of buffer. The magnitude of this movement is given by

$$\mu_{eof} = -\frac{\varepsilon\zeta}{\eta} \quad (2.9)$$



where  $\mu_{eof}$  is the EOF mobility,  $\zeta$  is zeta potential and  $\varepsilon$  is the dielectric constant. Thus, the overall mobility of an ion will be

$$\mu = \mu_e + \mu_{eof} \quad (2.10)$$

Figure 2.6 illustrates the mobilities of different types of ions. The electrophoretic mobility of the cations and the anions are opposite in the direction while the neutrals stay static. In the presence of the electroosmotic flow, all of them are brought to the end of the separation column with different velocities. According to their total migration mobility, the sequence of the ions arriving at the detector at the cathode can be expected as high mobility cations, low mobility cations, all neutrals, low mobility anions, and high mobility anions.

The application of capillary electrophoretic separation on microchips was first performed as early as 1992 [18, 19]. Up till now, the microchip capillary electrophoresis has been applied for quantitative analysis of various samples including inorganic ions, like the determination of nitrite in water [20], calcium in urine [21], lithium in blood [22], and ions in tap water [23]. Different organic molecules have also been analyzed, for example 4-amino-3-methyl-N-ethyl-N-( $\beta$ -methanesulfonamidoethyl)aniline in photographic developer [24], oxalate in urine [25], carnitines in water [26], taurine in energy and sport drinks [27], levoglucosan in aerosols [28], phenols in landfill leachate [29] and pharmacologically active ingredients in sweet potato [30].

### 2.3.2 Dielectrophoretic separation

Dielectrophoresis occurs in non-uniform electric fields and can be utilized for particle separation. When a particle is subjected to an electric field, charges of opposite signs are induced and the particle becomes polarized along the direction of the electric field. In a uniform electric field, the electrostatic forces on opposite ends of the dipole are equal and therefore no movement occurs. While in a non-uniform electric field, the electrostatic forces on opposite ends are different and the net force causes movement of the particle. The movement can be towards or away from the high field region. If the electrical polarizability of the particle is larger than that of the surrounding medium, the particle will move to high field region, this is called positive dielectrophoresis (pDEP). If, on the other hand, the electrical polarizability of the particle is lower than that of the surrounding medium, the particle will be driven to low field region, this is known as negative dielectrophoresis (nDEP). Based on this phenomenon, the particles exhibiting different polarizability can be easily separated from each other. The dielectrophoretic force is also proportional to the volume of the particle and the electric field gradient. Thus, DEP separation can also be based on the differences in the size of the particles. In the following part, different separation methods which are based on dielectrophoresis will be introduced.

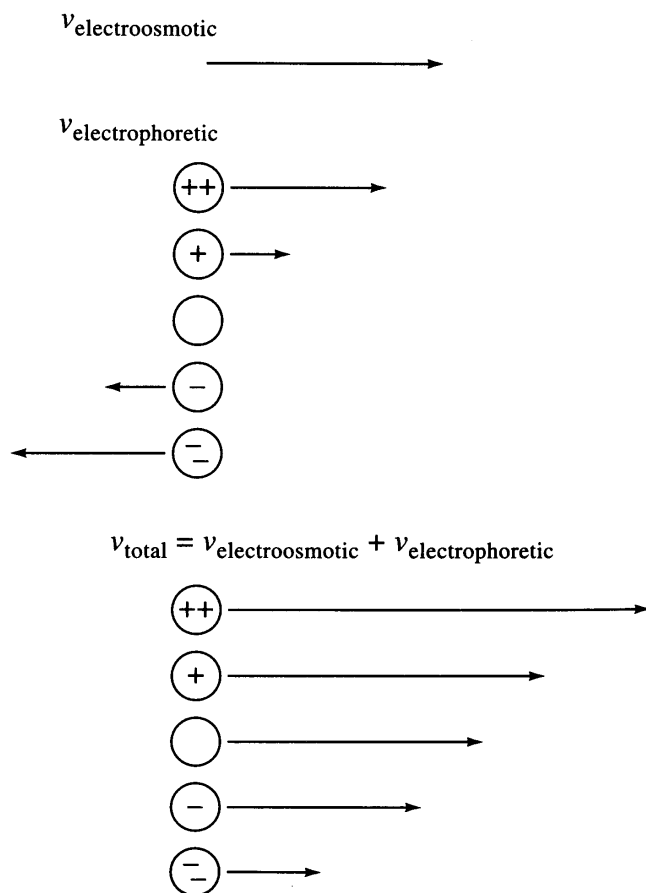


Figure 2.6: Particle mobility in CE.

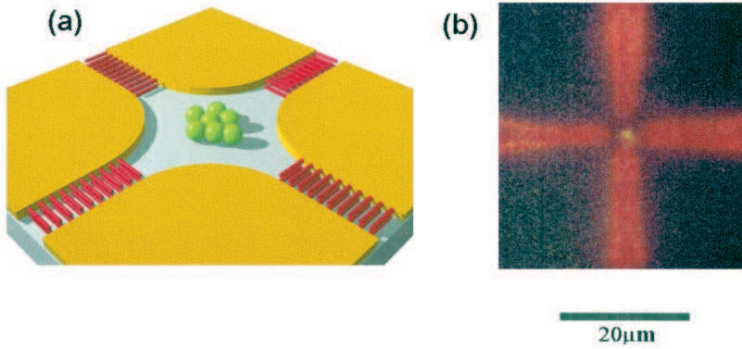


Figure 2.7: (a) Diagram and (b) photograph illustrating the separation of Tobacco Mosaic Virus (+DEP) and Herpes Simplex Virus (-DEP) in a polynomial electrode (adapted from [31]).

### DEP migration

DEP migration can be utilized to isolate different particles from particle mixture through their migration to, and collection in, different field regions. The most commonly used electrode geometry to generate the non-uniform electric field is shown in Figure 2.7a. Four electrodes are utilized to produce a quadrupole geometry where the electrodes are offset by 90 degree. Voltage application is accomplished by wiring electrodes diagonally opposite one another identically. The spatial separation of Tobacco Mosaic Virus and Herpes Simplex Virus was studied in this electrode geometry [31]. The Herpes Simplex Virus is trapped under negative DEP forces at the field minimum in the center of the electrode array, while simultaneously Tobacco Mosaic Virus experiences positive DEP and collects at the electrode edges. This is illustrated schematically in Figure 2.7a and the photograph of the observation is shown 2.7b. The principal drawback of this method is that particles cannot be separately collected for further downstream process.

### DEP affinity/DEP retention

In DEP affinity or DEP retention, a strong positive DEP force selectively traps target particles from a particle mixture at electrode edges and holds them against an imposed fluid flow stream, while a negative DEP force repels other particles from the electrodes so that they are levitated in the channel and subsequently swept out of the chamber by fluid flow.

Figure 2.8 shows the typical electrodes utilized in DEP affinity or DEP retention devices. As shown in the figure, castellated electrodes can be configured in two manners: directly opposite or with offset. In either case, the device is wired so that every other electrode has the same voltage input. In the case of castellated

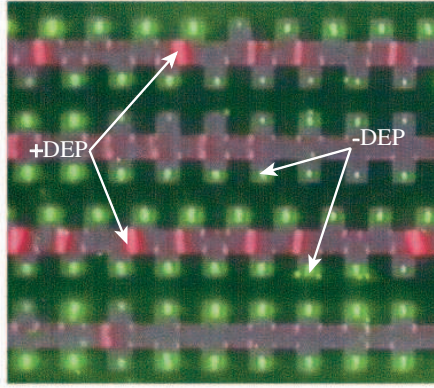


Figure 2.8: Image showing the separation of the red 216 nm latex particles (+DEP) and the green 557 nm latex particles (-DEP) in a castellated electrode array (adapted from [31]).

electrodes that are directly opposite each other, particles focused in the positive dielectrophoresis region will be found between the faces of the electrodes located across each other. Negative dielectrophoresis will congregate particles in the rectangular areas between the castellated electrodes. In the case of castellated electrodes with offset, the positive dielectrophoretic particle collection again occurs in the region between castellated electrodes located across each other, the difference being that the positive region is now found between the corners of the electrode faces. And the negative dielectrophoresis region is located in the rectangular wells between electrodes. Based on the castellated electrodes, G.H. Markx proposed to use gradients in conductivity to separate particles with different dielectric properties [32]. The conductivity of the flushing liquid is gradually and continuously increased so as to produce a conductivity gradient with time. The particles trapped by positive DEP force will be released from the electrodes according to their own dielectric properties and as a function of flow rate and medium conductivity.

### DEP field-flow-fractionation

Dielectrophoretic field-flow-fractionation (DEP-FFF) has been demonstrated to exhibit a high and electrically controllable discrimination for particle separation. DEP forces produced by microelectrodes are used to levitate particles in a thin chamber to equilibrium heights where sedimentation forces balance the vertical DEP force components. A carrier fluid moves through the chamber and establishes a parabolic hydrodynamic velocity profile causing cells of different dielectric and density properties levitated to different equilibrium heights to be transported through the chamber at different velocities and thereby being separated.

### Traveling wave DEP fractionation

Traveling wave dielectrophoresis (TWD) is the motion of polarizable particles induced by high-frequency traveling electric fields. Traveling electric fields are generated by rows of parallel electrodes addressed with three-phase or quadrature sinusoidal potentials, in which particles are induced to move asynchronously at speeds of up to 100  $\mu\text{m/s}$ . The dielectrophoretic force in the vertical direction, which is determined by the real part of the CM factor, balances the other vertical forces levitating the particles in the chamber. The TWD force inducing the movement of the particle is given by [33]

$$F_{TWD} = -\frac{4\pi\epsilon_m R_p^3 \text{Im}[K(\omega)] E^2}{\lambda} \quad (2.11)$$

where  $\lambda$  is the wavelength of the traveling wave and is usually equal to the distance between electrodes which have signals of the same phase applied.

### Continuous flow DEP separation

In the method of continuous flow DEP separation, the non-uniform electric field, normally generated by microelectrodes, induces a dielectrophoretic force field orthogonal to the direction of flow. The particles with different polarizability and/or size respond differently to this force field and are thus deflected to different outlets. Such devices are usually operated with alternating current in order to minimize electrolysis at the microelectrodes inside the channel. Because the dielectrophoretic force drops dramatically with the decrease of the particle size, continuous flow DEP separation has so far only been applied to a small range of samples, mainly polymer beads and yeast cells [34–37].

### Electrodeless DEP

The electrodeless dielectrophoresis is also known as insulator-based dielectrophoresis, since the nonuniform field was usually generated by applying a voltage along a channel that contained insulating obstacles. The applied voltage is normally DC voltage, therefore sometimes it is also called DC-dielectrophoresis. At low frequencies, because the dominant electrostatic effect is conduction, the CM factor depends solely on the conductivity of the particle and suspending medium. In many practical systems, at frequencies below 100 kHz, the CM factor can be approximated in terms of the real conductivities as

$$K(\omega) = \frac{\sigma_p - \sigma_m}{\sigma_p + 2\sigma_m} \quad (2.12)$$

where  $\sigma_p$  and  $\sigma_m$  represent the conductivities of the particle and medium, respectively. So, if the conductivity of the particle is greater than the conductivity of the medium, the particle will exhibit positive DEP, and vice versa.

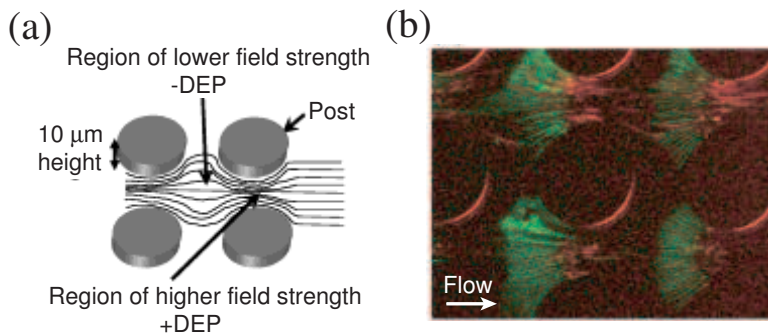


Figure 2.9: (a) Diagram showing how the insulating posts modify the field distribution. (b) Epifluorescence image of selective trapping of *E. coli* (labeled green) and *B. megaterium* (labeled red). (Adapted from [41])

In [38, 39], C.F. Chou and his fellows reported an alternative way to construct DEP traps by patterning geometrical constrictions in an insulating substrate instead of metallic microelectrodes and demonstrated DNA trapping using this device. The constriction is used to squeeze the electric field in a conductive solution, such as ionic buffer, thereby creating a high electrodeless dielectrophoresis.

Meanwhile, Cummings and Singh revealed dielectrophoretic concentration of latex particles in microchips containing arrays of insulating posts [40]. The post arrays with different post shapes are investigated including diamond posts, square posts and circular posts. The dielectrophoretic enhancement or depletion of particles in these three cases was experimentally demonstrated.

Later, Cummings's colleague Lapizco-Encinas utilized the insulator-based dielectrophoresis to separate and concentrate selectively mixtures of two species of live bacteria simultaneously [41]. A diagram showing how the insulating posts modify the field distribution is shown in Figure 2.9(a). The high electric field intensity region is located between the insulators where the electric field is compressed. And the low electric field density region is located at the crossroad of the insulators where the electric field is less compressed. At an applied field of 50 V/mm *B. megaterium* was still flowing while *E. coli* are seen trapped (Figure 2.9b).

In the above-mentioned methods, the target particles are selectively trapped at the constriction region by a strong dielectrophoretic force while the other particles are flushed away by the fluid flow. In order to release the target particles, the applied voltage has to be lowered down or cut off. Therefore, the particles are not continuously collected, which affects the throughput of the separation.

In 2006, Kang and co-workers [42] developed a continuous flow dielectrophoretic separation device, in which a 300  $\mu\text{m}$  channel was narrowed to 60  $\mu\text{m}$  by a rec-

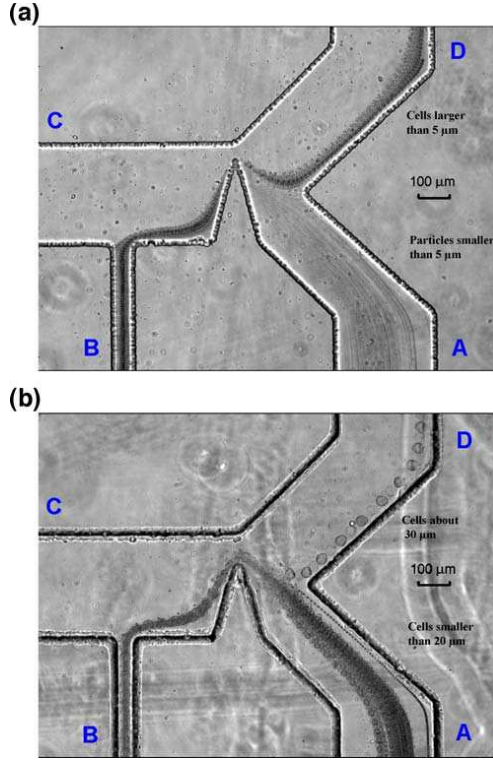


Figure 2.10: Separation of the cells with a triangular hurdle (adapted from [43]). (a) Separation of the white blood cells (larger than  $5\ \mu\text{m}$ ) from the debris. (b) Separation of the large breast stem cells from the other breast cells.

tangular hurdle. The negative DEP particle deviated from the streamline at the corner of the hurdle, where the local electric field strength is the highest. The degree of deviation depends on the DEP force (i.e. the particle size). The authors demonstrated the separation of  $5.7\ \mu\text{m}$  and  $15.7\ \mu\text{m}$  diameter particles into two downstream exits. Very recently, they proposed an improved design [43]. A triangular hurdle was used instead of the rectangular hurdle for effective separation of live cells with a low voltage (Figure 2.10).

Instead of the fixed obstacles, an oil droplet whose size can be dynamically changed was used to form the nonuniform electric field [44]. By adjusting the droplet size, particles of three different diameter sizes,  $1\ \mu\text{m}$ ,  $5.7\ \mu\text{m}$  and  $15.7\ \mu\text{m}$ , were successfully separated in a PDMS microfluidic chip.

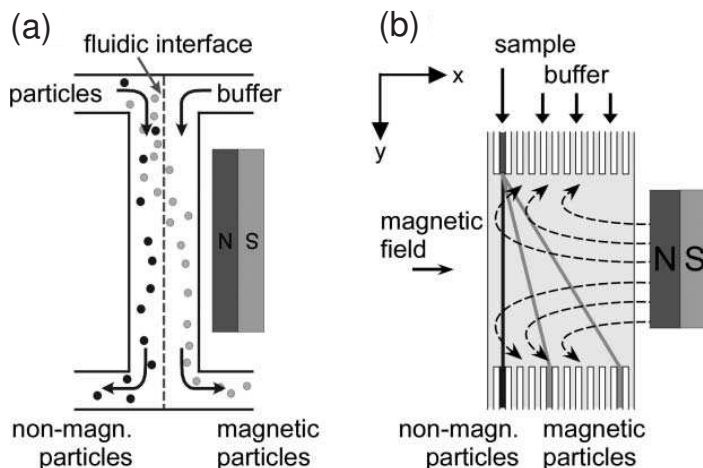


Figure 2.11: Continuous flow magnetophoretic separations. (a) Sorting of magnetic particles via two outlets. (b) Free-flow magnetophoresis of different magnetic particles via multiple outlets.

### 2.3.3 Magnetophoretic separation

As nonuniform electric field causes dielectrophoresis, nonuniform magnetic field will induce the movement of a magnetically susceptible object, such as a magnetic microparticle or a magnetically labelled cell. The magnetic force depends on the gradient of the applied magnetic field, the volume and magnetization of the particle. Therefore, particles of different size and/or different magnetization can be separated.

Early in 1990, Miltenyi *et al.* reported a high gradient magnetic cell separation with MACS [45]. In his method, the high gradient magnetic field in a column of steelwool (average diameter of  $50\ \mu\text{m}$ ) was generated by an external permanent magnet. The cells labelled with magnetic beads were trapped in the column while the unlabelled cells were eluted. Later, continuous separation of magnetic particles from a sample suspension in a microchannel network with two outlets was reported [46]. The magnetic particles were subjected to the magnetic force perpendicular to the direction of flow and were thus deflected from the sample suspension and could be collected at the other outlet (Figure 2.11a). To flexibly control on/off and the strength of the magnetic field, the electromagnets were introduced. Different methods to integrate the electromagnets with the microfluidic channel have been reported [47, 48]. The separators with multiple outlets is called free-flow magnetophoresis (Figure 2.11b). They could not only separate magnetic from non-magnetic particles but also separate magnetic particles of different size and/or magnetization [49, 50].



Magnetic manipulation has following advantages over electric manipulation: The magnetic field is applied externally, therefore the magnet will not have contact with liquid or particles; Unlike electrically induced forces, magnetic forces are not significantly influenced by ionic concentration, pH or surface charges; Magnetic manipulation is mild and normally does not do any harm to biological samples. However, magnetic manipulation only works on magnetically susceptible objects. Most materials do not exhibit intrinsic magnetism and hence must be labeled with magnetic particles.

### 2.3.4 Acoustophoretic separation

The particles in an acoustic standing wave field will experience both the primary and secondary radiation forces. The primary radiation force contributes the strongest acoustic force on the particles. Secondary forces are caused by the waves scattered by the surrounding particles, thus these forces are small and only happen when there are multiple particles in a suspension. The primary radiation force component which drives the particles to either the nodes or the antinodes of the acoustic wave is given by

$$F_r = -\left(\frac{\pi p_0^2 V_p \beta_m}{2\lambda}\right)\phi(\beta, \rho)\sin(2kx) \quad (2.13)$$

where  $p_0$  is the acoustic pressure amplitude,  $V_p$  is the volume of the particle,  $\beta_m$  is the compressibility of the medium solution,  $k$ , defined by  $2\pi/\lambda$ , is the wave number, and  $x$  is the distance from a pressure node.  $\phi$ , the acoustic contrast factor, takes the form

$$\phi(\beta, \rho) = \frac{5\rho_p - 2\rho_m}{2\rho_p + \rho_m} - \frac{\beta_p}{\beta_m} \quad (2.14)$$

$\rho_p$  and  $\rho_m$  are the density of the particle and the medium, respectively.  $\beta_p$  and  $\beta_m$  are the compressibility of the particle and the medium, respectively. The sign of  $\phi$  determines the direction of the acoustic force and thus whether the particle moves towards the node or towards the antinode (Figure 2.12).

The focusing of  $+\phi$  particles to the node of the standing wave was demonstrated with 5  $\mu\text{m}$  yeast cells by Hawkes and Coakley [51]. The yeast cells focused to the center of the channel could be collected in a central outlet, thereby getting separated from the bulky suspension.  $+\phi$  particles can be separated from  $-\phi$  particles in a standing wave. This was utilized for purification of blood from lipid droplets during open heart surgery [52]. The red blood cells which exhibit  $+\phi$  are driven to the wave node while the lipid droplets which exhibit  $-\phi$  are repelled to the wave antinode. It was also demonstrated that various size particles could be separated by acoustophoresis. A mixture of polystyrene particles with the

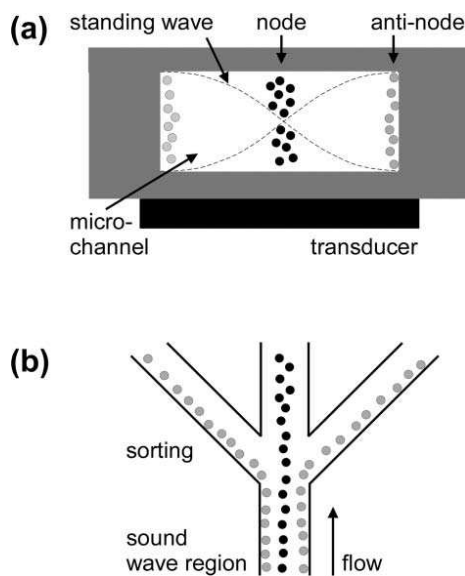


Figure 2.12: (a) Cross-sectional view and (b) top view of the channel in which the particles are focused towards either the node or antinode of the acoustic waves, depending on the sign of their acoustic contrast factors.

diameters of  $2\text{ }\mu\text{m}$ ,  $5\text{ }\mu\text{m}$ ,  $8\text{ }\mu\text{m}$ , and  $10\text{ }\mu\text{m}$  was separated and the particles are collected in different outlets [53].

Acoustic manipulation offers a method of non-contact particle handling, which avoids the direct interaction between the liquid and the transducer. All types of particles are susceptible to the acoustic standing wave if their acoustic properties are different from the surrounding medium. The acoustic manipulation has not been shown to damage cells or biological samples.

### 2.3.5 Separation via optical forces

Optical tweezers are capable of manipulating nano- and micro-sized dielectric particles by exerting very small optical forces via a highly focused laser beam. The dielectric particles tend to be attracted to the center of the narrowest point of the focused beam which is known as the beam waist. Particles differing in size, shape, or refractive index will have differences in the affinity to a stationary optical energy landscape. These affinity differences would lead to the particle sorting and separation in the absence of fluid flow. The Bessel light field has proven to be an interesting form of optical landscape which can be used for the sorting of erythrocytes and lymphocytes [54]. At a laser power of 550 mW, erythrocytes flipped and aligned to the rings of the Bessel beam becoming trapped in the outer rings, while lymphocytes moved directly to the beam center and get separated from the erythrocytes. In the presence flow, the particles can be continuously separated by means of an optical interference pattern, a so-called optical lattice. MacDonald and his coworkers demonstrated the sorting of two types of particles with different refractive indexes [55]. In an H-shaped channel device, a buffer solution was introduced, as well as a suspension with a mixture of  $2\text{ }\mu\text{m}$  silica particles ( $n=1.73$ ) and  $2\text{ }\mu\text{m}$  polymer particles ( $n=1.58$ ). When passing through the optical field, the polymer particles were deflected into the buffer carrying stream, whereas the silica particles flowed straight on. More recently, the same group demonstrated the separation of a mixture of four different size silica particles ( $2.3\text{ }\mu\text{m}$ ,  $3.0\text{ }\mu\text{m}$ ,  $5.17\text{ }\mu\text{m}$  and  $6.84\text{ }\mu\text{m}$ ) [56].



## Chapter 3

# Dielectrophoretic Separation in Iterative Curves

What makes capillary electrophoresis (CE) such a powerful separation technique is that it could achieve separation and analysis of hundreds of compounds efficiently in one run. However, the plug dispersion that usually occurs in the curves of the very long serpentine channel will seriously degrade the separation. Besides, the requirement of thousands volt high separation voltage hampers its way to the in-line application. On the other hand, dielectrophoresis (DEP) has been demonstrated to have excellent capabilities of manipulating microparticles and even nowadays nanoparticles. The dielectrophoretic separation which has already been demonstrated are either non-flow separation (e.g. DEP migration or DEP affinity) where particles cannot be collected for downstream detection and analysis, or continuous flow separation where the induced dielectrophoretic force field is orthogonal to the direction of flow and deflects the particles to different outlets. In these cases, the number of the analyte types which can be analyzed is very limited compared with CE. So far, dielectrophoresis has rarely been demonstrated for particle batch separation. The electric field gradient in the curves which causes separation deterioration in capillary electrophoresis is found can be utilized for dielectrophoretic separation. Therefore, we would like to develop a dielectrophoretic based separation which can do batch separation as well as CE, but does not suffer from the curves and does not require such high separation voltages as CE does. To this end, the dielectrophoretic separation in iterative curves is proposed. Before introducing the dielectrophoretic separation in iterative curves, the dielectrophoretic separation in a single curve is firstly investigated.

## 3.1 Separation in a curve

### 3.1.1 Using a DC electric field

The time-averaged dielectrophoretic force acting on a spherical particle, immersed in a medium and exposed to a spatially non-uniform electric field can be described by [57]

$$\langle \vec{F}_{DEP} \rangle = 2\pi\epsilon_m R_p^3 \text{Re}[K(\omega)] \nabla |\vec{E}_{rms}|^2 \quad (3.1)$$

where  $\nabla |\vec{E}_{rms}|^2$  is the gradient of electric field squared,  $\epsilon_m$  is the permittivity of the suspending medium,  $R_p$  is the radius of the particle, and

$$K(\omega) = \frac{\epsilon_p^* - \epsilon_m^*}{\epsilon_p^* + 2\epsilon_m^*} \quad (3.2)$$

$K(\omega)$  is the frequency dependent Clausius-Mossotti (CM) factor,  $\epsilon_p^*$  and  $\epsilon_m^*$  represent the frequency dependent complex permittivities of the particle and medium, respectively, The complex permittivity is defined as  $\epsilon^* = \epsilon + \sigma/(j\omega)$ , where  $j = \sqrt{-1}$ ,  $\epsilon$  is the permittivity, and  $\sigma$  is the conductivity of the dielectric.

At low frequency, because the dominant electrostatic effect is conduction,  $\text{Re}[K(\omega)]$  depends solely on the conductivity of the particle and suspending medium. In many practical systems, at frequency below 100 kHz, the CM factor can be approximated in terms of the real conductivities as

$$K(\omega) = \frac{\sigma_p - \sigma_m}{\sigma_p + 2\sigma_m} \quad (3.3)$$

where  $\sigma_p$  and  $\sigma_m$  represent the conductivities of the particle and medium, respectively. So, if the conductivity of the particle is greater than the conductivity of the medium, the particle will exhibit positive DEP, and vice versa.

For small particles (low Reynolds numbers) ignoring Brownian motion and the buoyancy force, the DEP force moving the particle is balanced with the fluid drag force slowing it down, which is given by

$$F_{DEP} = -F_{drag} = 6\pi\eta R_p v_p \quad (3.4)$$

where  $v_p$  is the particle velocity and  $\eta$  is the medium viscosity. Thus for a spherical particle the dielectrophoretic mobility will be

$$\mu_{DEP} = \frac{R_p^2 \epsilon_m \text{Re}[K(\omega)]}{3\eta} \quad (3.5)$$

in the direction of  $\nabla|\vec{E}_{rms}|^2$ . It can be seen that for a spherical particle moving in an electric field gradient, the dielectrophoretic mobility is proportional to the surface area of the particle and the CM factor and the direction of the particle movement is dependent on the sign of CM factor.

The basic principle of the separation in the curve is illustrated in Figure 3.1 By applying a DC voltage over the curve, a non-uniform electric field is generated, whose gradient directs towards the center of curvature of the curve. The sample mixture is driven along the channel by the electroosmotic flow. Due to the different DEP force magnitudes and directions, the particles with different DEP responses move continuously to the different location across the channel as they flow, thus get continuously separated into the different outlets. In the micro-channels the Reynolds number is low enough for inertial effects to be irrelevant so that the centrifugal force on the particles could be ignored. Thus along the radius direction, as expressed in (3.5), the particle mobility depends on the CM factor and the particle size for a given suspending medium. The particles with positive DEP response  $Re[K(\omega)] > 0$ , will be attracted towards the center of curvature. While the particles with negative DEP response  $Re[K(\omega)] < 0$ , will be driven away from the center of curvature. As a result, the positive DEP particles will deflect towards the inner sidewall while the negative DEP particles will deflect towards the outer sidewall. For the particles with the same DEP polarity, the larger particle will have higher DEP mobility and thus will experience larger deflection in the transverse direction.

In the flow direction, the low Reynolds number particles adapt to the fluid flow instantly. Since the velocity of the electroosmotic flow in the channel is proportional to the electric field intensity, the flow velocity at the inner side of the channel will be faster than that at the outer side of the channel. The particles with different CM factor and/or size will follow different paths and therefore will get separated in the time domain, as shown in Figure 3.1.

To track the particle movement in the curve, the trajectory calculations were implemented in Matlab 7.0 after the field calculations were performed with Comsol Multiphysics 3.4. The 3D model of the curved channel built in Comsol Multiphysics 3.4 is with an inner curvature radius of 50  $\mu\text{m}$ , an outer curvature radius of 100  $\mu\text{m}$  and a channel height of 20  $\mu\text{m}$ . When a 10 V DC voltage was applied over the channel, the simulated electric field gradient inside the channel is shown in Figure 3.2a. The DEP force normalized to polarizability  $\nabla|\vec{E}_{rms}|^2$ , as depicted in Figure 3.2b, directs towards the center of curvature everywhere in the channel. The magnitude of the normalized DEP force drops dramatically as the radius increases.

For the spherical low Reynolds number particles running in the uniform viscous flow with dielectrophoretic force acting on them, the velocity of the particles can be calculated as

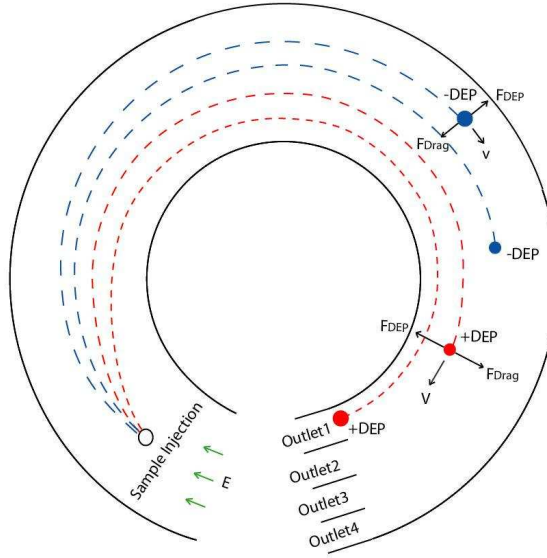


Figure 3.1: Schematic diagram of the DEP separation in a curve by applying a DC electric field.

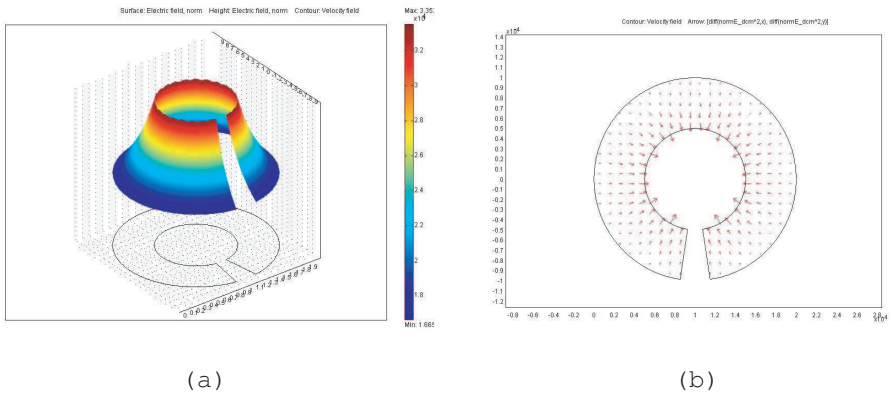


Figure 3.2: Simulation of (a) electric field distribution and (b) normalized DEP force in a curve.



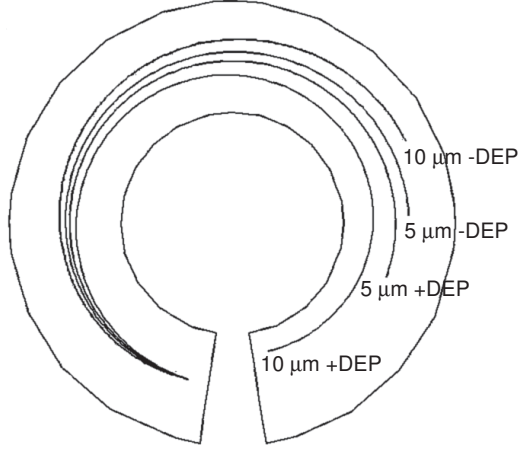


Figure 3.3: Simulated trajectories of 4 different types of particles in a timeframe of 2 seconds.

$$\vec{v}_{particle} = \frac{\vec{F}_{DEP}}{6\pi R_p \eta} + \vec{v}_{fluid} \quad (3.6)$$

The position of the particle after a certain time can be approximated by summing the distances traveled in a short period of time using the velocities calculated by above formula. Four types of particles with different sizes and dielectric properties were simulated. They are 5  $\mu\text{m}$  and 10  $\mu\text{m}$  radius pDEP particles and 5  $\mu\text{m}$  and 10  $\mu\text{m}$  nDEP particles. The retrieved trajectories of these four types of particles in a timeframe of 2 seconds are shown in Figure 3.3, which proves the concept. By a number of simulations, the angular displacement of these four particles versus time was obtained and is shown in Figure 3.4a, which verifies the particle separation in the time domain. The transverse displacement of the particles at the channel outlets was also simulated with respect to different voltage levels applied over the curve, as shown in 3.4b, which demonstrates the separation in the spatial domain. It can be seen from the figure that the voltage applied over the curve imposes significant influences on the separation, since the DEP force acting on particles has a second order dependence on the strength of the electric field.

### 3.1.2 Using a DC-biased AC electric field

In the case of DC dielectrophoresis, the DC voltage applied over the curve generates the electroosmotic flow and the dielectrophoretic force simultaneously, both of which are proportional to the voltage level. When the DC voltage is increased, the sample mixture will be driven faster forward by the enlarged electroosmotic

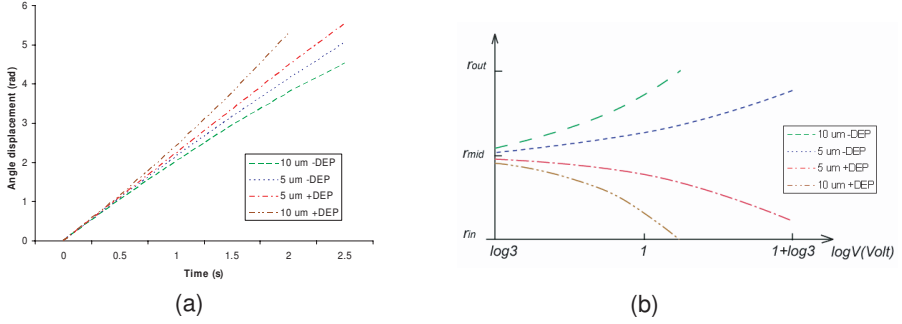


Figure 3.4: (a) Angular displacement of 4 different types of particles as a function of time. (b) Transverse position of 4 different types of particles at the channel outlets as a function of the applied voltage,  $r_{in}$  and  $r_{out}$  represent the inner sidewall and the outer sidewall, respectively.

flow and thus the time for separation will become less. This makes it not so efficient for sub-micron particle separation, since an extremely high voltage might be required. The solution we found to decouple the dielectrophoresis from the electroosmosis is by applying an AC voltage with a small DC offset. The AC voltage is responsible for the DEP separation while it doesn't give any momentum to the sample mixture in the flow direction. The small DC offset drives the sample mixture slowly forward to the outlets. By controlling the ratio between the AC and the DC voltages, the separation of various size distributions can be achieved.

To mathematically describe the particle behavior in the curve with applied DC-biased AC field, a model describing the hydrodynamic and dielectrophoretic force was developed to determine the particle movement in the micro-channel. These forces are actuated by a DC-offset AC electric field with a single AC frequency.

$$\alpha = \frac{|\vec{E}_{ac}|}{|\vec{E}_{dc}|} \quad (3.7)$$

$\alpha$  is the ratio of AC to DC electric field amplitudes. Therefore the time-averaged dielectrophoretic force acting on a spherical particle takes the form

$$\langle \vec{F}_{DEP} \rangle = 2(\alpha^2 + 1)\pi\epsilon_m R_p^3 \text{Re}[K(\omega)] \nabla |\vec{E}_{dc}|^2 \quad (3.8)$$

A DC voltage applied over the curve generates an electric field as

$$|\vec{E}_{dc}| = \frac{V_{dc}}{\pi r} \quad (3.9)$$

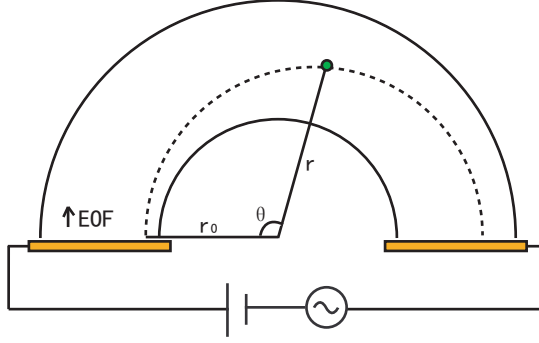


Figure 3.5: Movement of the particle in the radial and angular coordinates.

The gradient of the square electric field in the curve is along the radial direction to inside and can be calculated as

$$\frac{\partial |\vec{E}_{dc}|^2}{\partial r} = -\frac{2V_{dc}^2}{\pi^2 r^3} \quad (3.10)$$

where  $V_{dc}$  is the DC voltage applied over the curve and  $r$  is the radial position as shown in Figure 3.5. Electroosmosis is the bulk flow of fluid owing to the motion of ions in the diffuse double layer. Assuming that ion distributions can be described by Boltzmann statistics, we obtain the following result to describe the velocity of fluid inside the curve

$$v_{EO} = -\frac{\varepsilon_m \zeta}{\eta} \vec{E}_{dc} = -\frac{\varepsilon_m \zeta V_{dc}}{\eta \pi r} \quad (3.11)$$

where  $\zeta$  is the zeta potential and  $\eta$  is the viscosity of the liquid. The fluid flow caused by electroosmosis in turn generates a viscous drag on the particles and the drag force can be described by Stokes law as

$$F_{drag} = 6\pi\eta R_p(v_{EO} - v) \quad (3.12)$$

For small Reynolds number particles, the DEP force is balanced by the viscous drag force at steady state.

$$F_{DEP} + F_{drag} = 0 \quad (3.13)$$

Substituting  $F_{DEP}$  and  $F_{drag}$  with (3.8) and (3.12) yields the motion of the particles in the radial and angular coordinates.

$$\begin{cases} v_r = \frac{dr}{dt} = -\frac{2(\alpha^2 + 1)\varepsilon_m R_p^2 Re[K(\omega)]V_{dc}^2}{3\eta\pi r^3} \end{cases} \quad (3.14)$$

$$\begin{cases} w = \frac{d\theta}{dt} = -\frac{\varepsilon_m \zeta V_{dc}}{\eta\pi r^2} \end{cases} \quad (3.15)$$

Solving the differential equation (3.14), the radial position of the particles as a function of time takes the form

$$r(t) = \sqrt[4]{r_0^4 - \frac{8(\alpha^2 + 1)\varepsilon_m R_p^2 Re[K(\omega)]V_{dc}^2}{3\eta\pi^2} t} \quad (3.16)$$

here  $r_0$  is the radial position of the starting point, as shown in Figure 3.5. The radial displacement of the particles in a time period of  $t$  can be derived by  $r(t) - r_0$ . By inserting (3.16) to (3.15) and integrating  $w$  over  $t$ , we obtain the angular displacement of the particles as a function of time, which is plotted in Figure 3.6 for four different size particles.

$$\theta = \int w dt = \frac{3\pi\zeta}{4(\alpha^2 + 1)R_p^2 Re[K(\omega)]V_{dc}} \left( \sqrt[4]{r_0^4 - \frac{8(\alpha^2 + 1)\varepsilon_m R_p^2 Re[K(\omega)]V_{dc}^2}{3\eta\pi^2} t} - r_0 \right) \quad (3.17)$$

It can be seen from the figure that the difference in the particle angular displacement increases along time. Let  $\theta = \pi$ , the obtained  $t$ , by solving (3.16), will be the retention time of the particle in the curve. That is

$$T = -\frac{2(\alpha^2 + 1)Re[K(\omega)]\eta\pi^2 R_p^2}{3\varepsilon_m \zeta^2} - \frac{\eta\pi^2 r_0^2}{\varepsilon_m \zeta V_{dc}} \quad (3.18)$$

Assuming the size difference between each type of particles to be very small, the separation sensitivity here defined by the increment in time per increment in the particle size can be expressed with the derivative of (3.18) with respect to  $R_p$ .

$$\frac{\partial T}{\partial R_p} = -\frac{4(\alpha^2 + 1)Re[K(\omega)]\eta\pi^2 R_p}{3\varepsilon_m \zeta^2} \quad (3.19)$$

From (3.19) it can be concluded that the separation sensitivity does not depend on the position of the starting point, which means that no matter where the particles enter the curve from, the retention time difference of two types of particles will be the same. The sensitivity also does not depend on either the AC or the DC amplitude, but has a second order dependence on the ratio of AC to DC

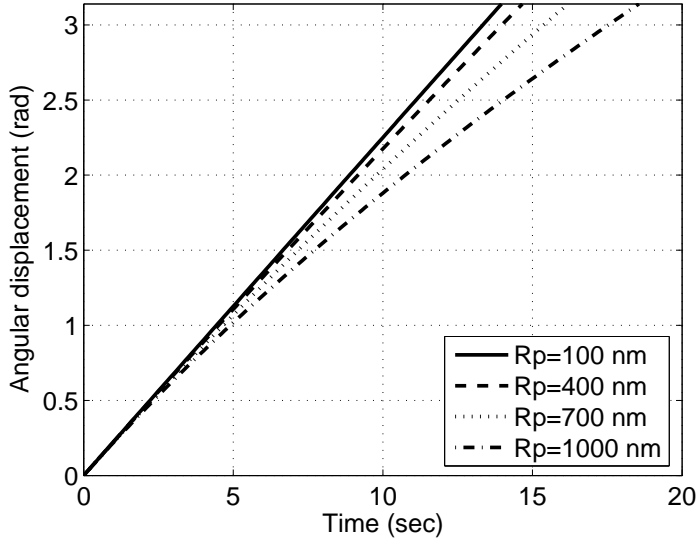


Figure 3.6: Angular displacement of four different size particles versus time variation.

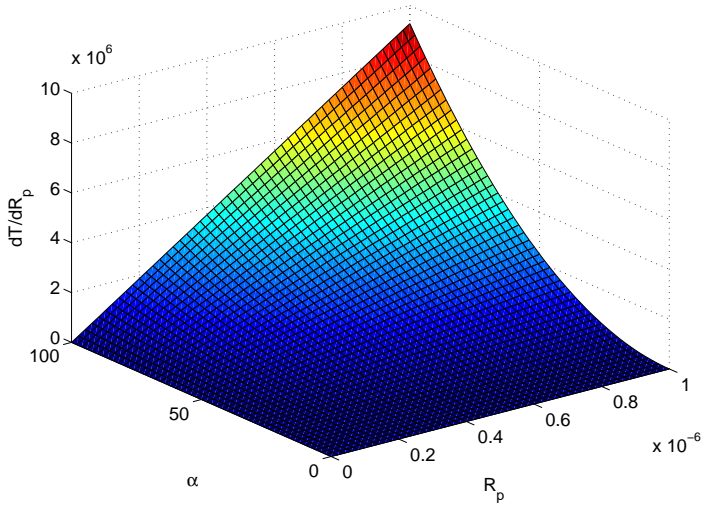


Figure 3.7: Separation resolution versus the ratio of AC to DC field amplitudes and the particle size.

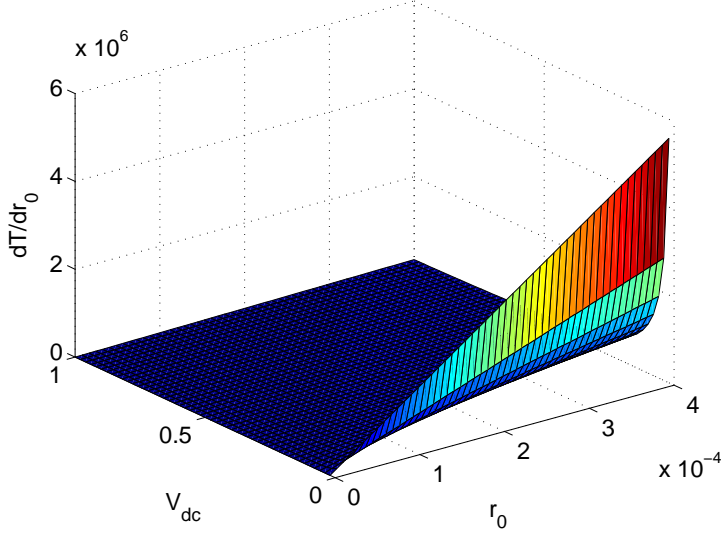


Figure 3.8: Sensitivity to the starting point deviation versus the position of the starting point and the applied voltage level.

amplitudes ( $\alpha$ ) and a linear dependence on the particle size (Figure 3.7). When the separation of very small particle is desired,  $\alpha$  must be raised high enough to render a detectable separation.

The retention time of the particles is sensitive to the starting position deviation. When the starting position of the particles differs from each other, deterioration will occur to the separation. The sensitivity to the starting point deviation could be found by differentiating the time in (3.18) with respect to  $r_0$ .

$$\frac{\partial T}{\partial r_0} = -\frac{2\eta\pi^2 r_0}{\epsilon_m \zeta V_{dc}} \quad (3.20)$$

From (3.20) it can be concluded that by increasing the applied voltage level or shifting the starting point closer to the inner sidewall, the sensitivity to the starting point deviation can be reduced (Figure 3.8).

### 3.1.3 Separation resolution

The separation resolution is limited by Brownian motion and is voltage dependent. Brownian motion is the movement of particles induced by the constant and random collision from molecules of the liquid. The non-deterministic force driven by

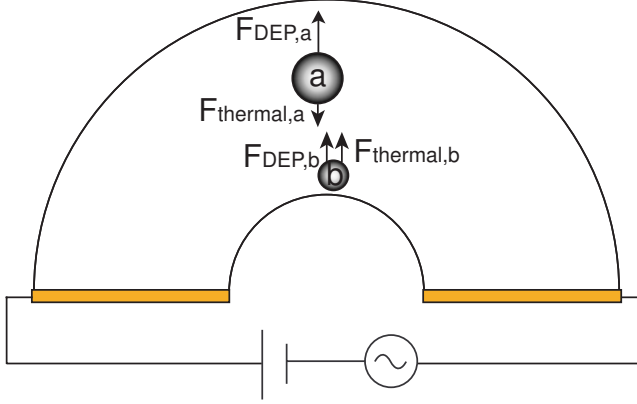


Figure 3.9: Force diagram showing the worst moment for the separation of two types of particles in the presence of Brownian motion.

the Brownian motion will take a significant effect, especially when the particles are scaled down to sub-micron size. To achieve a desired separation resolution, the voltage applied on the curve has to be sufficiently high to make the DEP force acting on the particle dominate over the Brownian motion which can be treated as a random force whose maximum value is given roughly by

$$F_{thermal} \approx k_B T / 2R_p \quad (3.21)$$

where  $k_B$  is the Boltzmann constant,  $T$  is the temperature, and  $R_p$  is the particle radius. Thus, the ratio of the DEP force to the thermal force is proportional to the fourth power of the particle radius.

Let us consider the separation of two different types of particles whose radius are  $R_{p,a}$  and  $R_{p,b}$ , respectively, and  $R_{p,a} > R_{p,b}$ . The thermal forces acting on the particles change direction all the time with a maximum amplitude given by (3.21). The worst moment for the separation is that the thermal force on the larger particle slows down its dielectrophoretic movement when the thermal force on the smaller particle accelerates its, as shown in Figure 3.9. If the larger particle is driven faster towards the outer sidewall than the smaller particle at this worst moment, the separation will certainly be achieved and will increase with the increase of time.

$$v_{r,a} > v_{r,b} \quad (3.22)$$

The velocity of the particles can be described by means of a balance of the dielectrophoretic force, the thermal force due to Brownian motion, and the fluid drag force. So, (3.22) becomes

$$\frac{F_{DEP,a} - F_{thermal,a}}{6\pi\eta R_{p,a}} > \frac{F_{DEP,b} + F_{thermal,b}}{6\pi\eta R_{p,b}} \quad (3.23)$$

Substituting  $F_{DEP}$  and  $F_{thermal}$  with (3.8) and (3.21) yields

$$(\alpha^2 + 1)\nabla|\vec{E}_{dc}|^2 > \frac{k_B T}{2\pi\epsilon_m} \frac{\frac{1}{R_{p,a}^2} + \frac{1}{R_{p,b}^2}}{R_{p,a}^2 - R_{p,b}^2} \quad (3.24)$$

Let  $R_{p,a} = 200$  nm and  $R_{p,b} = 100$  nm, (3.24) becomes:

$$(\alpha^2 + 1)\nabla|\vec{E}_{dc}|^2 > 3.98 \times 10^{15} (V/m^2)^2 \quad (3.25)$$

Inserting (3.10) to (3.25), we get:

$$(\alpha^2 + 1)V_{dc}^2 > 4.24 \times 10^3 V^2 \quad (3.26)$$

Neglecting the DC component due to the large ratio of AC to DC amplitudes, we obtain that the root mean square value of the AC voltage is larger than 64 V ( $V_{rms} > 64$  V). This means when the voltage applied over the curve is above 64 V, the 100 nm and 200 nm radius particles can have a deterministic separation. Below 64 V, the DEP separation will be degraded by the Brownian motion. Assuming that the radius of the smallest particles in the sample mixture is  $R_{p,min}$ , and the size difference between types of particles is  $\Delta R_p$ , the threshold voltage required to achieve an appreciable separation can be derived as:

$$V_{rms,th} = \sqrt{\frac{\pi r^3 k_B T}{4\epsilon_m} \frac{\frac{1}{(R_{p,min} + \Delta R_p)^2} + \frac{1}{R_{p,min}^2}}{\Delta R_p (2R_{p,min} + \Delta R_p)}} \quad (3.27)$$

The threshold voltage as a function of  $R_{p,min}$  and  $\Delta R_p$  is plotted in Figure 3.10. It can be seen from the figure that a decrease in either  $R_{p,min}$  or  $\Delta R_p$  will increase the threshold voltage. A rather high voltage will be required, if the particles are not only small but also have very little size difference. The threshold voltages for achieving different separation resolutions were calculated and are shown in Table 3.1. This table reveals the possibility of separating nano-particles by applying sufficiently high voltages over the curve. For the micrometer size particles, the threshold voltage is much less due to their much weaker Brownian mobility.

Alternatively, the random displacement of a particle due to Brownian motion over time can be described as a distribution which follows a Gaussian profile with a mean squared displacement (in three dimension) given by [58]



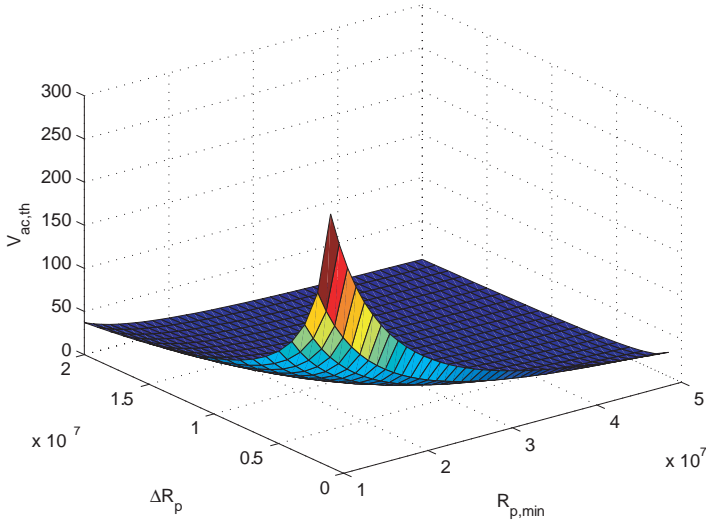


Figure 3.10: Threshold voltage versus the smallest particle radius and the particle size difference.

Table 3.1: Calculated threshold voltage for achieving different separation resolutions

Min. radius ( $R_{p,min}$ )	Size difference ( $\Delta R_p$ )	Threshold voltage ( $V_{rms,th}$ )
100 nm	50 nm	107.1 V
100 nm	100 nm	64.3 V
200 nm	50 nm	42.5 V
200 nm	100 nm	26.8 V
300 nm	50 nm	24.3 V
300 nm	100 nm	15.7 V
400 nm	50 nm	16.2 V
400 nm	100 nm	10.6 V
500 nm	50 nm	11.7 V
500 nm	100 nm	7.8 V
500 nm	250 nm	4.3 V
500 nm	500 nm	2.6 V

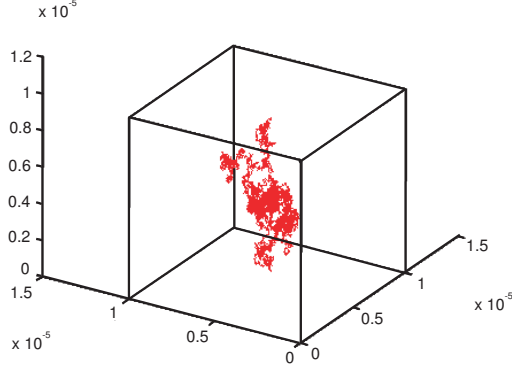


Figure 3.11: Simulated Brownian motion of a 100 nm radius particle in 1 second

$$\lambda = \sqrt{6Dt} \quad (3.28)$$

where  $D$  is the diffusion coefficient. For a spherical particle of radius  $R_p$ , this is given by

$$D = \frac{k_B T}{6\pi\eta R_p} \quad (3.29)$$

Figure 3.11 shows the simulated Brownian motion of a 100 nm radius particle in stationary liquid in a timeframe of 1 second with  $\Delta t = 1$  ms in calculation.

The velocity of a particle moving in the presence of the fluid drag, dielectrophoretic force, and Brownian motion in a 3-D coordinate system is therefore given by

$$\begin{cases} V_x = V_{liq,x} + \frac{\varepsilon_m R_p^2 \text{Re}[K(\omega)]}{3\eta} \frac{\partial |E_{rms}|^2}{\partial x} + \sqrt{\frac{6D}{\Delta t}} \cos \alpha \cos \beta \\ V_y = V_{liq,y} + \frac{\varepsilon_m R_p^2 \text{Re}[K(\omega)]}{3\eta} \frac{\partial |E_{rms}|^2}{\partial y} + \sqrt{\frac{6D}{\Delta t}} \cos \alpha \sin \beta \\ V_z = V_{liq,z} + \frac{\varepsilon_m R_p^2 \text{Re}[K(\omega)]}{3\eta} \frac{\partial |E_{rms}|^2}{\partial z} + \sqrt{\frac{6D}{\Delta t}} \sin \alpha \\ \alpha = \text{rand}[0, 2\pi], \beta = \text{rand}[0, 2\pi] \end{cases} \quad (3.30)$$

Implementing above equations in Matlab 7.0, the trajectories of the particles can be approximated by adding the distances traveled in a short  $\Delta t$  time. The

trajectories of five 100 nm and five 200 nm particles in the presence of Brownian motion were simulated and are shown in Figure 3.12. When  $V_{rms}$  applied over the curve is 30 V, the trajectories of these two types of particles overlap each other (Figure 3.12a). When  $V_{rms}$  is increased to 70 V, the separation between these two types of particles becomes clearly visible (Figure 3.12b). This simulation result is in a very good agreement with the calculated threshold voltage which is 64 V.

## 3.2 Concept of the design

To achieve a larger separation, we would like to propose a novel design in which a number of curves are connected in series. The principle schematic of the design is illustrated in Figure 3.13. A small DC voltage applied over the complete length of the channel governs a slow electroosmosis and drives the sample mixture slowly forward along the channel. The AC voltages applied over the curves generate high non-uniform electric fields locally in the curves. For the negative DEP particles, the DEP force acts along the radius of the curves to the outer side and thus the larger particles will be driven more to the outer side of the curves. Since the electroosmotic flow at the inner side of the channel is faster than that at the outer side of the channel, the larger particles following the outer paths will be left behind. Since the curves are bended in the opposite directions, the separation will be canceled to a great extent in the next curve. Therefore, the concentrators in the straight segments are employed to bring all the particles to the same entering point for the next curve. After a number of iterative curves, particles will get fully separated.

## 3.3 Particle focusing

### 3.3.1 Requirements and options

The function of the focusing elements in the straight segments is to concentrate all the particles to an equal entering point for the next curve. They should meet the following requirements:

- All the particles in the sample mixture should be tightly focused.
- The separation should not be adversely affected by the focusing elements.

If the particles are not focused tightly in the straight segments, a large starting point deviation will occur, which will in turn affect the separation quality in the curves as explained before. In the curves, the larger nDEP particles are supposed to flow behind the smaller nDEP particles. But, if the smaller particles are slowed down more than the larger particles in the focusing segments, the separation

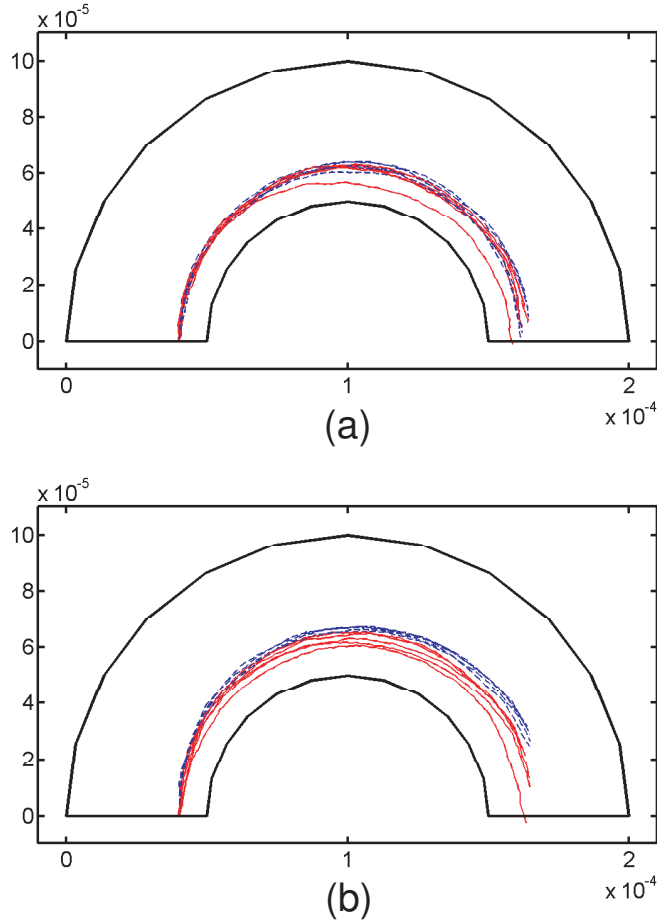


Figure 3.12: Simulated trajectories of two different types of particles (five 200 nm radius particles in dashed lines and five 100 nm radius particles in solid lines) taking into account the Brownian effect. (a) When  $V_{rms} = 30$  V, these two types of trajectories overlap together. (b) When  $V_{rms} = 70$  V, the 100 nm radius particles are separated from the 200 nm radius particles.

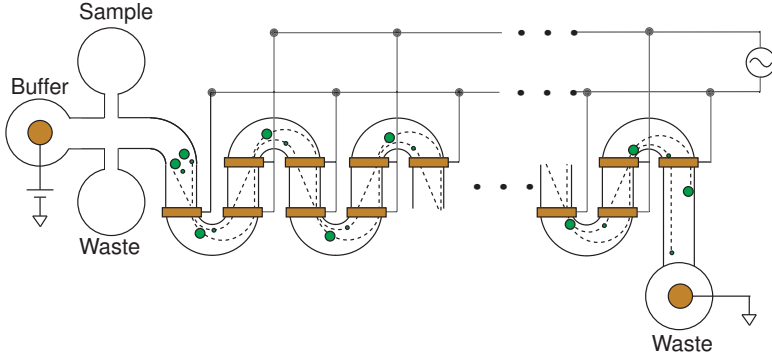


Figure 3.13: Principle schematic of the electrokinetic DEP separation in iterative curves.

will be decreased or even be destroyed. Dielectrophoretic focusing has attracted our significant attention, since it can perform particle focusing without disturbing the fluid flow in the channel. Therefore, we will investigate two dielectrophoretic methods in which the nonuniform fields are generated by two types of electrode configurations: the slanted planar electrode arrays and the top-and-bottom electrode pairs.

### 3.3.2 Slanted planar electrode arrays

It was concluded that a top-and-bottom electrode structure performs superior to the planar array for negative DEP [59] because stronger electric field gradients are generated and particles are forced away from walls where nonuniform flow and nonspecific particle adhesion can occur. However, compared with a simple planar electrode array, top-and-bottom electrodes are more difficult to fabricate because the array must be aligned and sealed carefully. Custom systems must be designed for these purposes, and the overall process is slow. As an alternative, a planar electrode array allows fast prototyping by using dry film resists as described later in Chapter 6.

In this section, we report the investigation on the particle deflection in the slanted planar electrode arrays subjected to different electric field frequencies in the presence of the fluid flow. It is proved by simulations and experiments that the particles deflect to opposite directions at low and high frequencies due to the different working mechanisms which are AC electroosmosis (ACEO) and dielectrophoresis, respectively. The particle behaviors under the domination of ACEO or DEP will be explained and discussed.

### Experimental results

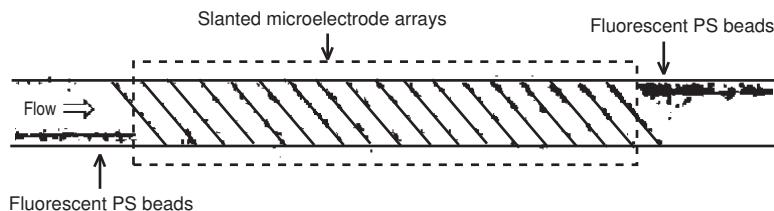


Figure 3.14: Inverted fluorescence image of the polystyrene beads being deflected across the channel.

The particles used in the experiments are carboxylated polystyrene spheres with a diameter of  $2\text{ }\mu\text{m}$ . After the flow velocity was stabilized at around  $600\text{ }\mu\text{m/s}$ , a  $100\text{ KHz}$  AC voltage was applied over the adjacent electrodes. Instantly, the deflection of the particle in the transverse direction was observed. When the peak-to-peak voltage was increased to  $27\text{ V}$ , all the particles were deflected across the  $100\text{ }\mu\text{m}$  wide channel and focused to the other side of the channel as they move along the microchannel, as shown in Figure 3.14. Several slanted microelectrode arrays are placed in series with some distance away from each other. The focused incoming particle stream in Figure 3.14 is formed by the previous electrode array which slants in the opposite direction.

The required voltage level to fully deflect the particles across the  $100\text{ }\mu\text{m}$  channel was measured at different flow velocities and is plotted in Figure 3.15. When the flow velocity was decreased to  $190\text{ }\mu\text{m/s}$ ,  $22\text{ V}$  peak-to-peak voltage became enough. It also can be seen from the figure that the required voltage is almost linearly proportional to the flow velocity.

When decreasing the frequency of the electric field, the deflection of the particles was found enlarged. Therefore, the amplitude of the voltage required to focus the particles to the other side of the channel can be reduced as the frequency of the voltage decreases, as shown in Figure 3.16. At frequencies above  $1\text{ MHz}$ , deflection of the particles to the opposite direction was observed.

### nDEP dominating

AC electroosmosis vanishes at very high frequencies (e.g. above  $1\text{ MHz}$  in the experiments), since the free charge density vanishes due to the finite diffusion time required to build up the diffuse layer. Therefore, dielectrophoresis dominates the behavior of the particles in this frequency range. When the particles suspended in liquid flow continuous across an array of slanted, planar, interdigitated electrodes, the particles experience a transverse dielectrophoretic force, which will deflect them to one side of the channel. Particles exhibiting nDEP will be forced away from the electrode structures toward the channel top (Figure 3.17).

At the top height of the channel, the highest electric field region is located at the middle of the electrode gaps and the lowest electric field region is located at the

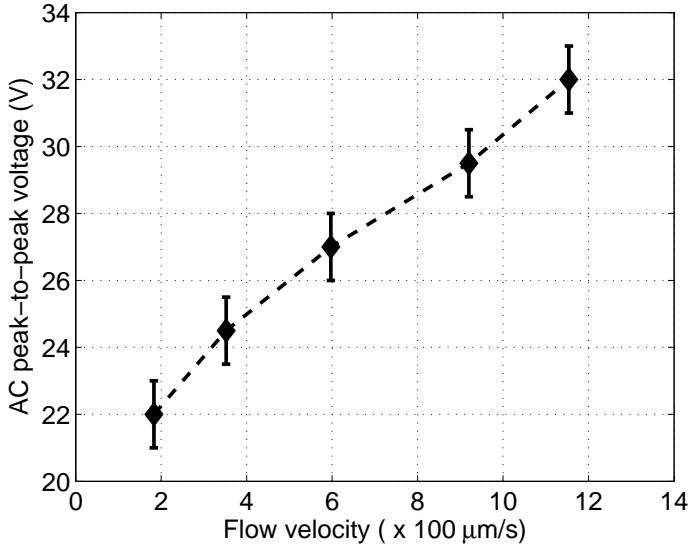


Figure 3.15: Required voltage level versus the flow velocity for fully deflecting the  $2 \mu\text{m}$  particles across the  $100 \mu\text{m}$  wide channel.

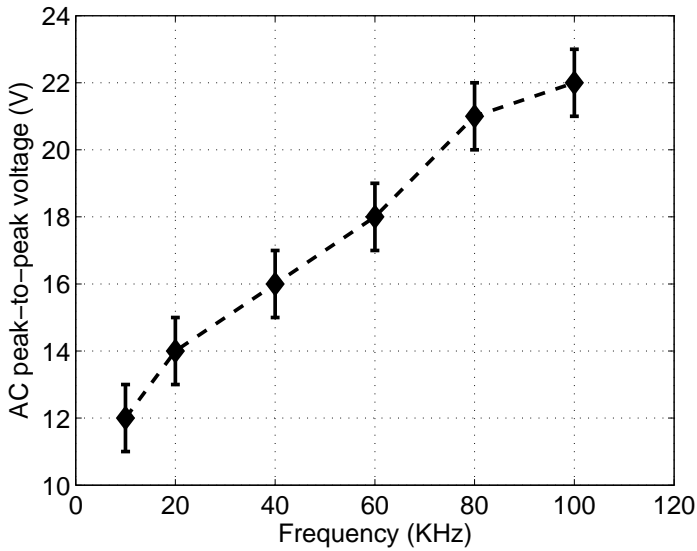


Figure 3.16: Required voltage amplitude at different frequencies for fully deflecting the  $2 \mu\text{m}$  particles across the  $100 \mu\text{m}$  wide channel.

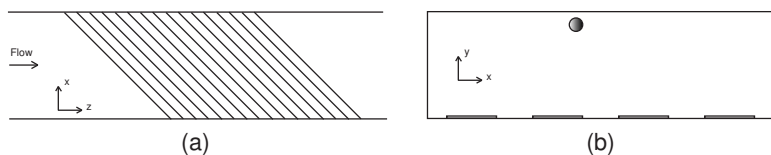


Figure 3.17: (a) A top view of the channel showing the slanted planar electrode array and the direction of the flow, and (b) a cross-sectional view of the channel showing the location of the particle during operation.

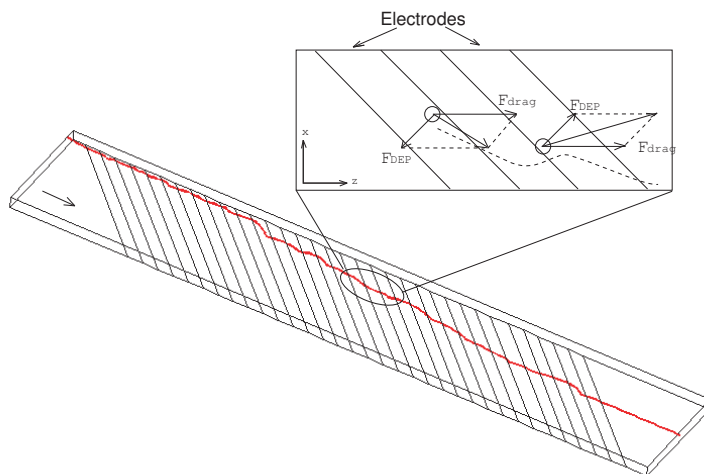


Figure 3.18: Simulated particle trajectory in the slanted planar electrode arrays under the influence of nDEP, with combination of a force diagram showing how the DEP force deflects the particle.

middle of the electrodes. Before the particle reaches the middle of the electrode gap, the component of the DEP force in the flow direction slows down the particle and the DEP force component in the transversal direction drives the particle to -x direction. After the particle passes the middle of the electrode gap, the DEP force changes to the opposite direction, as shown in Figure 3.18, and will give a rise to the particle speed in the flow direction and drive the particle to the +x direction in the transversal direction. Since the travel time the particle takes before the middle of the electrode gap is longer than after it, the short time difference will give particles a small displacement in the transversal direction. The particles will shift to the slanting direction of the electrodes as shown in Figure 3.18.

Figure 3.19 is the numerical simulation data which shows the effects of voltage and flow velocity on the transverse displacement of  $4 \mu\text{m}$  particles after a 1 mm



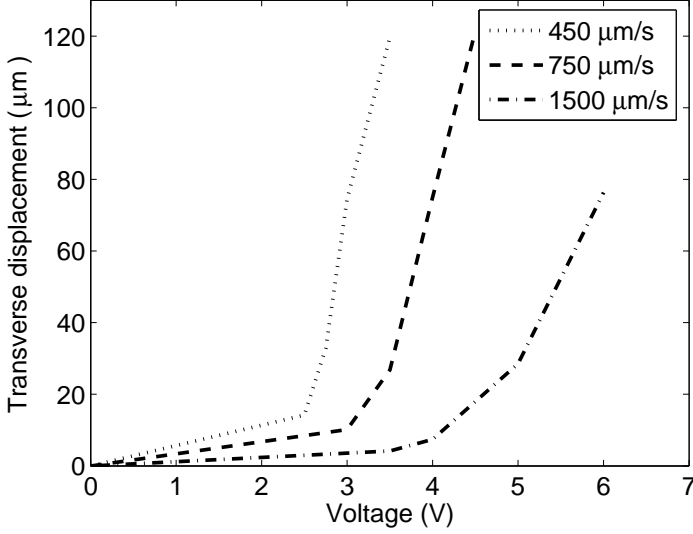


Figure 3.19: Simulated data showing the effects of voltage and flow velocity on the transverse displacement (after 1 mm long array) of 4  $\mu\text{m}$  particles.

long array. A larger transverse displacement happens at a lower flow velocity for a given voltage level. At small voltage levels, the increment of the voltage has very small effect on the transverse deflection while at the voltage level above a particular value it has a rather large effect on the transverse displacement.

Values of the square of the electric field from the channel top in the x-direction were extracted from the numerical model and closely resembled as sine wave with a period equal to the electrode space (Figure 3.20). Moreover, to map the field along the length of the channel (the z-direction), a term was added adjusting the phase of the field with the position in the channel. The resulting approximation to the square field gradient for 45° slant angle electrodes takes the form

$$|E^2| = AV^2 \sin\left(\frac{2\pi z}{\lambda_z} - \frac{2\pi x}{\lambda_x}\right) + AV^2 \quad (3.31)$$

The amplitude of the wave is  $A$ ,  $V$  is the voltage applied at the electrodes, and  $\lambda$  is the width of the electrode plus the electrode spacing. At steady status, the DEP force is balanced with the fluid drag force.

$$F_{DEP} + F_{drag} = 6\pi\eta R_p(v_{liq} - v) + 2\pi\epsilon_m R_p^2 \text{Re}[K(\omega)]|\nabla|E^2| = 0 \quad (3.32)$$

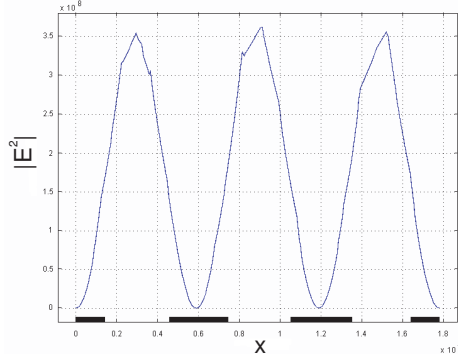


Figure 3.20: Square of the electric field above the microelectrode arrays at the top of the channel.

By inserting the approximation into  $|E^2|$ , the particle velocity in transverse and length direction can be obtained, i.e. the following ordinary differential equations

$$\begin{cases} v_x = \frac{dx}{dt} = \frac{2\pi R_p^2}{3\eta\lambda_x} \epsilon_m \text{Re}[K(\omega)] AV^2 \cos\left(\frac{2\pi z}{\lambda_z} - \frac{2\pi x}{\lambda_x}\right) \\ v_z = \frac{dz}{dt} = v_{liq} - \frac{2\pi R_p^2}{3\eta\lambda_z} \epsilon_m \text{Re}[K(\omega)] AV^2 \cos\left(\frac{2\pi z}{\lambda_z} - \frac{2\pi x}{\lambda_x}\right) \end{cases} \quad (3.33)$$

Solving the ordinary differential equation, the particle displacement at the end of the array takes the form

$$x_{out} = \frac{1}{2} \left( \frac{2\pi}{3\eta\lambda_x} \epsilon_m \text{Re}[K(\omega)] A \right)^2 L \frac{R_p^4 V^4}{v_{liq}^2} \quad (3.34)$$

$L$  is the longitudinal length of the electrode array. The particle transverse displacement turns out to have a fourth-order dependence on voltage and particle size and a second order dependence on flow velocity.

### ACEO dominating

AC electroosmosis (ACEO) vanishes at both very low and very high frequencies. At intermediate frequencies (e.g. 10-100 KHz in the experiments), AC electroosmosis dominates the movement of the particles in the microchannel. The AC electroosmosis generated by the microelectrode array produces roll-cells orientated as illustrated schematically in Figure 3.21. The particles are driven forward along the channel by the fluid drag force, meanwhile, they fluctuate up and down in the channel under the influence of the AC electroosmosis. As the particles follow the

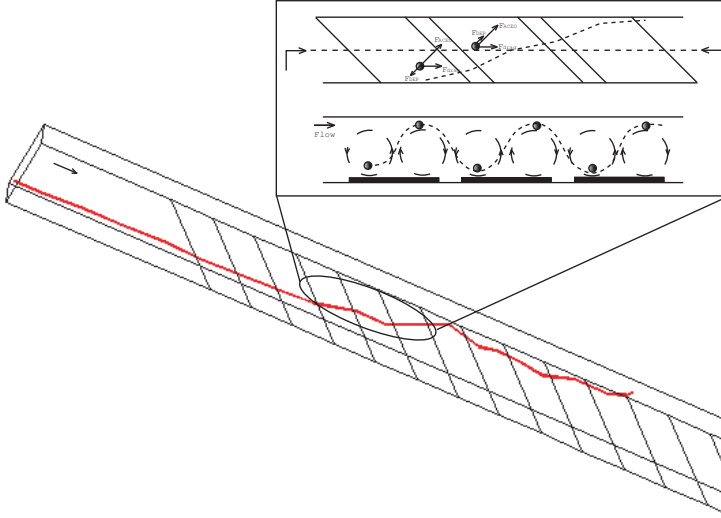


Figure 3.21: Simulated particle trajectory under the influence of ACEO, together with a schematic diagram showing how the ACEO deflects the particle.

vortices and the electroosmotic slip velocity is in the direction of the tangential electric field component, the particles deflect to the direction perpendicular to the electrodes. Alternate in and out of the focus of the microscope observed in the experiments proves the fluctuating movement of the particles above the electrode arrays.

The trajectory was calculated with Matlab after the field simulation was performed in Comsol Multiphysics. The particle deflects to the same side as what was seen in the experiments when it moves through the electrode arrays, as shown in Figure 3.21. Compared with the trajectory under the influence of nDEP as shown in Figure 3.18, the trajectory under the influence of ACEO deflects just in an opposite direction.

When the Stokes force on the particles induced by AC electroosmosis is comparable to the DEP force, the particle elevation will be determined by the vertical component of the DEP force and the vertical component of the electroosmotic force. In order to understand the lateral movement of the PS particles, the coupling between the lateral composite force and vertical composite force must be considered, which is beyond the scope of this thesis.

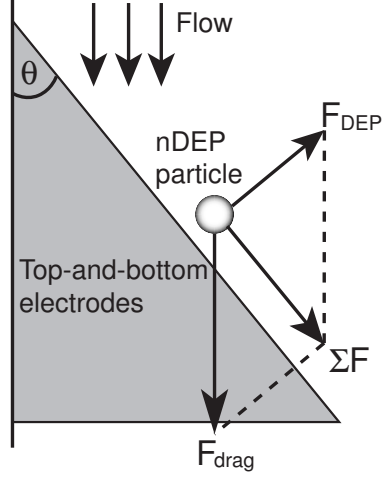


Figure 3.22: Top-view force diagram for a nDEP particle fully repelled by a top-and-bottom electrode pair.

### 3.3.3 Top-and-bottom electrode pairs

It has been shown that the cells or microparticles can be focused in three dimensions using electric field cages generated by pairs of electrodes on the top and bottom sides of the micro-channel [60, 61]. The performance of different electrode configurations for microparticle sorting was compared, which shows that the top-and-bottom electrodes perform better than the planar electrodes and the top-and-bottom electrodes extending all the way to the sidewall will have the highest sorting efficiency [59]. Hence, the possibilities of focusing different size particles especially nanoparticles by using this top-and-bottom electrodes configuration will be investigated in this section.

As a particle approaches a triangular top-and-bottom electrode pair, the dielectrophoretic force which is always in the direction orthogonal to the electrode edges increases. When the dielectrophoretic force becomes large enough to balance the fluid drag force component perpendicular to the electrode edges, the particle will follow the outline of the electrodes, as shown in Figure 3.22. During the movement, the viscous drag will appear on the particle and keep the particle moving at a constant velocity. So, the forces meet the following requirement

$$|\vec{F}_{\text{DEP}}| = |\vec{F}_{\text{drag}}| \sin \theta \quad (3.35)$$

where  $\theta$  is the angle of the electrode edge with respect to the channel sidewall. From the equation we could see that the required dielectrophoretic force has to be

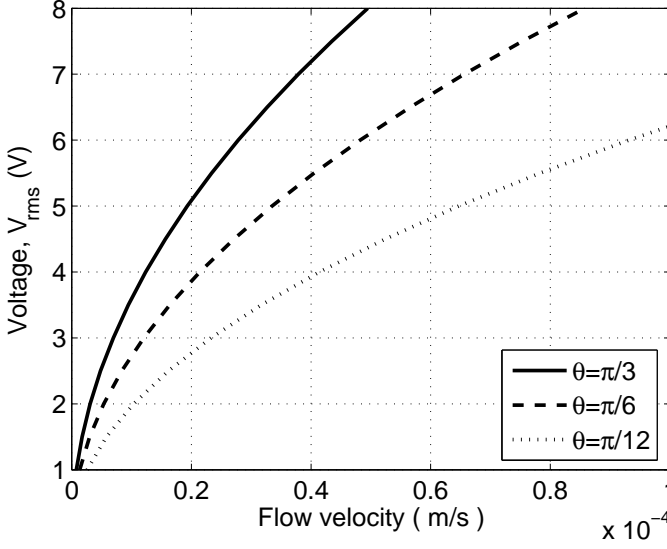


Figure 3.23: Curves showing the effects of flow velocity and  $\theta$  on required voltage for focusing 100 nm radius particles.

increased if increasing the electrode angle  $\theta$ . Inserting (3.8) and (3.12) to (3.35), we obtain

$$\nabla |\vec{E}|^2 = \frac{3\eta \sin\theta v_{liq}}{\varepsilon_m \text{Re}[K(\omega)] R_p^2} \propto V_{ac}^2 \quad (3.36)$$

The voltage required on the electrodes for effective focusing is proportional to the flow velocity and inversely proportional to the radius of the particle.

By means of finite element simulation, the highest electric field gradient around the top-and-bottom electrode edges in a 10  $\mu\text{m}$  deep channel was achieved. And in turn the required voltage on the electrodes for focusing of 100 nm radius particles at different flow velocities could be calculated based on (3.36), and is shown in Figure 3.23. Three types of lines correspond to the electrodes with three different angles. From this figure, it can be seen that to successfully focus 100 nm radius particles with a moderate voltage the flow velocity has to be very low. And a smaller electrode angle can also relieve the voltage required for focusing. At a given flow velocity (i.e. 100  $\mu\text{m/s}$ ), the voltage required for focusing of different size particles is shown in Figure 3.24. For the nanoparticles, the required voltage increases dramatically along with the decrease of the particle size. For 100 nm radius particles, around 6 V can be sufficient for focusing with 15 degree electrodes, which is in good agreement with the data in Figure 3.23.

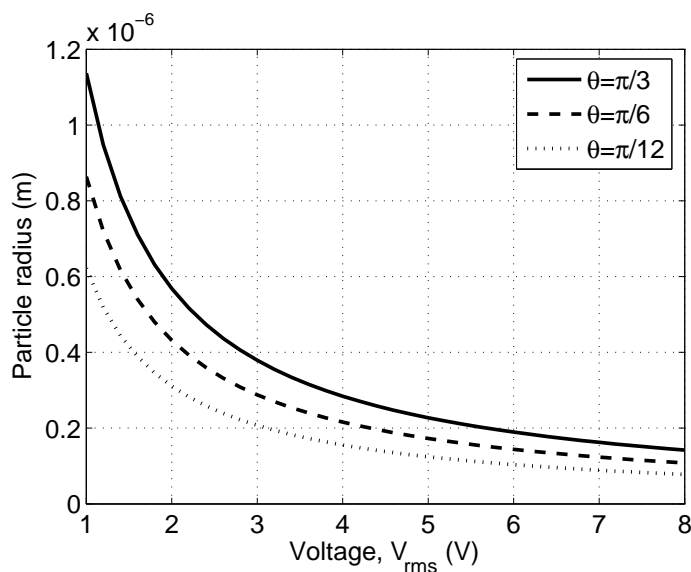


Figure 3.24: Curves showing the effects of particle size and  $\theta$  on required voltage for particle focusing at the flow velocity of  $100 \mu\text{m/s}$ .

The electrothermal effect can cause unusual particle motion particularly near electrode edges. The electrothermal flow was simulated for this focusing element but found to be negligible, since the majority of the particles are sufficiently far from the electrode edges and also the conductivity of the solution is very low. At higher conductivities, Joule heating may lead to significant electrothermal effects, especially at the relatively high voltages used for the focusing of nanometer particles.

### 3.4 Electro-kinetic DEP separation in iterative curves

The separation in a single curve has already been proved previously by simulation and analytical calculation. Particle focusing by different electrode configurations was also investigated. In contrast with the planar electrode arrays, focusing by the top-and-bottom electrodes was found more efficient and controllable. Therefore, the straight segments with top-and-bottom focusing electrodes will be used to connect the curves. In this section, the results of particle tracing in iterative curves will be presented. The reason why the particles are preferably focused to the channel center will be explained first.

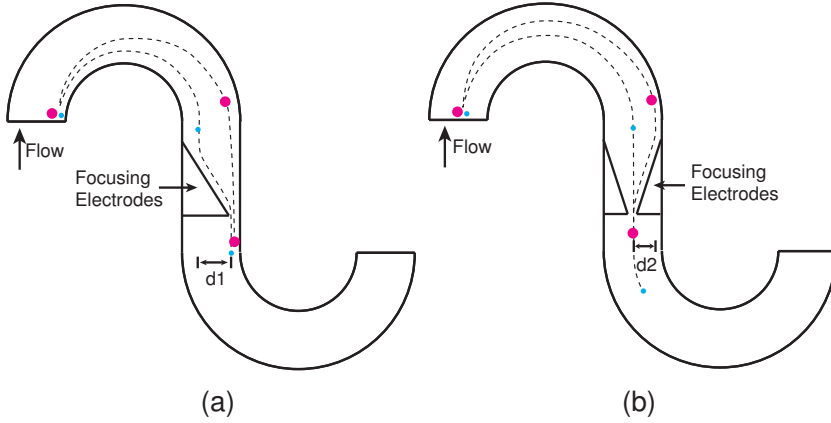


Figure 3.25: Comparison between two focusing schemes: (a) focusing to the inner sidewall and (b) focusing to the channel center.

### 3.4.1 Comparison of focusing schemes

If the particles are focused closely to the inner sidewall of the curve, as shown in Figure 3.25a, the particles can experience the strongest field gradient and thus can have a large separation. Besides, the width of the channel can be fully utilized for the DEP repelling, since all the nDEP particles will be driven to the outer tracks in the curves. But there is a significant disadvantage of this focusing scheme. In the following straight segment, all the particles have to be repelled to the opposite side of the channel to keep the same entering point for the next curve. If assuming that there are two different size particles traveling in the channel as shown in Figure 3.25a, and the lateral distance of the smaller and the larger particles needs to be shifted by the focusing electrodes are defined as  $d_1$  and  $d_2$ , respectively.  $d_1$  will be much larger than  $d_2$  when these two particles have a big difference in size. To render a very small particle undergo a large dielectrophoretic movement by the focusing electrodes is very difficult, because the DEP force scales down with the third power of the particle radius. Furthermore, the DEP force component in the flow direction will slow down the particles. The smaller particles exposed longer time to the DEP forces might decelerate more than the larger particles, so that degradation in the separation might occur.

These problems can be solved if the particles are focused to the channel center before entering the curves, as shown in Figure 3.25b. The nDEP particles will end up in the curve with certain deflection from the channel center. In the following straight segment, the particles are sent back to the channel center by the focusing electrodes. The lateral distance needs to be shifted by the focusing electrodes depends on how far the particle was repelled away from the channel center in the curve. Therefore, the required shift for the smaller particle is smaller than

Table 3.2: Simulation parameters.

Simulation parameter	Value
Voltage on the curves ( $V_{pp}$ )	40 V
Voltage on the focusing electrodes ( $V_{pp}$ )	2 V
EOF velocity	110 $\mu\text{m/s}$
Channel width	50 $\mu\text{m}$
Channel depth	10 $\mu\text{m}$
Curve inner wall radius	50 $\mu\text{m}$
Simulation timeframe	18 s
Time step	50 ms

---

for the larger particles ( $d_1 < d_2$ ). This can release the voltage level required on the focusing electrodes. Moreover, being exposed longer time to the DEP force will slow down the larger particles more than the smaller particles and hence the separation will be enlarged.

### 3.4.2 Simulation results

In Comsol multiphysics 3.4, two electrostatic modules were used for simulation of AC dielectrophoresis and DC electroosmosis, respectively. A Stokes module was selected for flow simulation. A 3D model for a microchannel containing 4 curves was built with the dimensions and the boundary conditions as listed in Table 3.2. The electrode edges and the inner side of the curves were expected to have the highest electric field gradients and therefore the meshes at those places should be defined relatively fine. After meshing, the velocity field was calculated in the global coordinate system with finite element method. After the channel geometry and the field values were imported to the Matlab 7.0, the field-dependent force acting on the particle was calculated which defines the velocity of the particle and in turn the distance it travels in a short time step. Finally, the particle trajectory was retrieved by summing all short distances the particle traveled in a short time.

Figure 3.26 shows the simulated particle trajectories for two types of particles, i.e. 100 nm and 300 nm radius particles, which are fairly in accordance with the theoretical expectation. In the curves, both particle types are repelled to the outer tracks and the 300 nm radius particles are driven more to the outer side than the 100 nm radius particles. In the focusing segments, the particles are driven back to the channel center. After 18 s, the 100 nm radius particle arrives at the end and the 300 nm radius particle is left behind. The retention time for different particles with radii in the range of 100-300 nm was simulated and is listed in Table 3.3. The retention time as a function of the particle size is plotted in Figure 3.27, from which it can be seen that the retention time has an almost linear dependence on the particle radius.



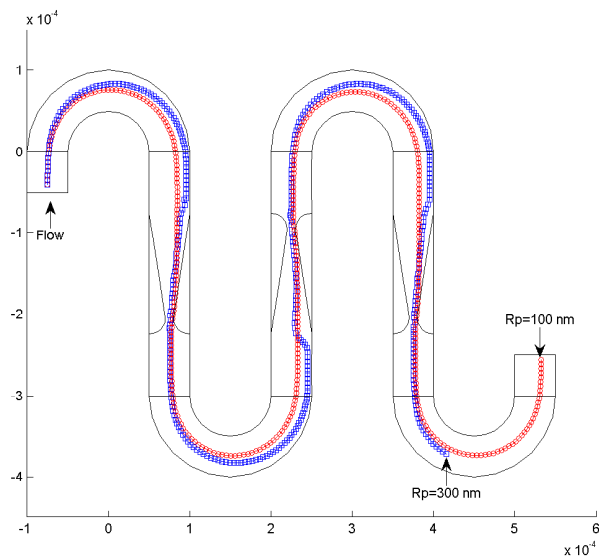


Figure 3.26: Top view of a fragment of the electrokinetic DEP separation channel containing 4 curves and the simulated trajectories for two different types of particles (i.e. 100 nm and 300 nm radius particles).

Table 3.3: Simulated retention time of different size particles.

Particle radius (nm)	Retention time (s)
100	18
150	18.5
200	19.1
250	19.7
300	20.3

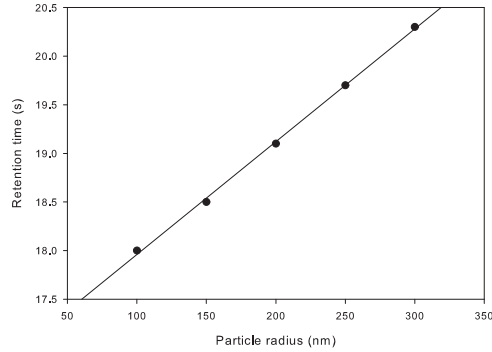


Figure 3.27: Simulated retention time as a function of particle size in the electrokinetic DEP separation channel containing 4 curves.

## 3.5 Discussions

### 3.5.1 First focusing segment

The first focusing segment demands a better focusing performance than the rest focusing segments, which is mainly due to the following reasons:

- The input sample plug of the 1st focusing segment is much wider than that of the rest focusing segments which has already been, to a great extent, concentrated.
- The 1st focusing segment has to shift the smallest particles difficultly from the sidewall to the channel center by dielectrophoresis, while the smallest particles require only an easy push in the rest focusing segments since they are repelled the least away from the channel center in the preceding curves.
- The rest focusing segments even do not have to drive all the particles exactly back to the channel center. The separation will not be affected as long as the larger particles that experience larger DEP forces are shifted across the smaller particles. This will relieve the voltage requirements on the rest focusing electrodes and will increase the range of the particle size that can be analyzed.

Therefore, an effective operation of the first focusing segment is of great importance to the whole separation system. The top-and-bottom electrode configuration introduced in the previous section is able to focus particles whose radiuses are below 100 nm by applying very high electric fields. However, such high electric

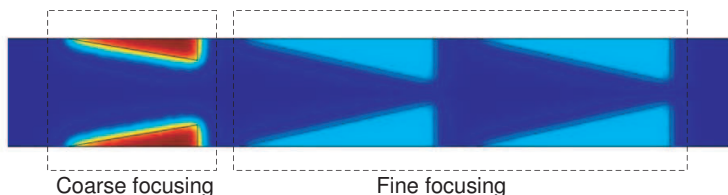


Figure 3.28: Two step focusing in the first straight segment.

fields are prone to block the large particles in the sample mixture. To address this issue, a two step focusing method is proposed, as shown in Figure 3.28. The small electrodes in the front are connected to a higher voltage, so as to generate a larger field gradient and repel the small particles coarsely towards the center. Since the field gradient reduces dramatically at the places far from the electrodes, the large particles can still pass through. The following large electrodes that stretch more to the channel center are connected to a lower voltage and will therefore finely focus all the particles to the channel center.

### 3.5.2 Sample plug profile

In practical operation, the sample mixture is delivered to the separation channel by a cross injection or a double-T injection and the profile of the sample plug appears as shown in Figure 3.29a. After passing through the first focusing electrode pairs, the sample plug will be stretched in the flow direction, with the particles from channel center leading in front and those from two sides left behind (Figure 3.29b). In the next phase, the separation among different analytes increases continuously under the influence of dielectrophoresis. But some parts of the analytes are still overlapped together, as can be seen in Figure 3.29c. Finally, separated zones will form, containing each only single type of analyte having the same mobility (Figure 3.29d). At the end of the separation channel, a detection window measures the amount of analytes and peaks are observed.

Inevitably, plug broadening will occur during operation. However, the degree of the broadening is very limited, since it only occurs in the first focusing segment. Thereafter, the dielectrophoretic forces will not broaden the plug of each analyte any more but will increase the separation between different analytes. When the DEP separation becomes large enough to yield distinct zones, the importance ingredients in the sample mixture will be identified.

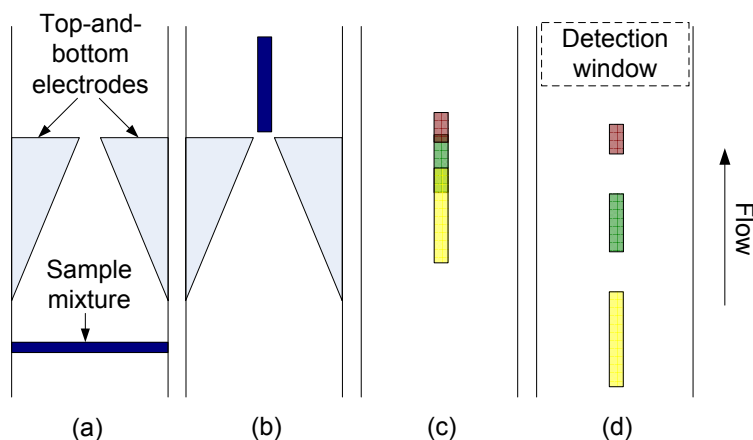


Figure 3.29: Schematic view showing the change of the plug profile during separation process.

### 3.5.3 Thickness of the insulating film

When a DC voltage is applied over the entire channel to generate the EOF, the potential in the liquid decreases linearly along the channel. If the focusing electrodes and the electrodes on the curves contact directly with the liquid, the DC offset of each electrodes has to be set precisely to the local potential in the channel to avoid the disturbance on the EOF, which is difficult to be implemented. The way to solve this problem is by insulating all the AC electrodes inside the channel with a dielectric layer. The insulating film has to withstand the voltage difference on each every electrode. Therefore a minimal breakdown strength is required for the film.

Figure 3.30 illustrates the potential in the channel and the potential on the electrodes distributed along the channel. From the figure, it can be seen that the maximum potential difference  $\Delta V_{max}$  happens to the electrodes which are closest to the EOF driving electrodes. The breakdown voltage of the silicon oxide deposited by CVD process found in literature is  $10^6$  V/cm. If the thickness of the oxide film is  $d_{is}$ , in order to prevent the breakdown, the potential difference should meet:

$$\Delta V_{max} < 10^8 d_{is} \quad (3.37)$$

The electrical model of two insulated electrodes in the liquid is shown in Figure 3.31.  $C_{is}$  is the capacitance of the insulating film,  $C_{liq}$  is the capacitance of the liquid and  $R_{liq}$  is the resistance of the liquid. Apparently, the voltage on the liquid is only part of the voltage applied on the electrodes due to the voltage drop over

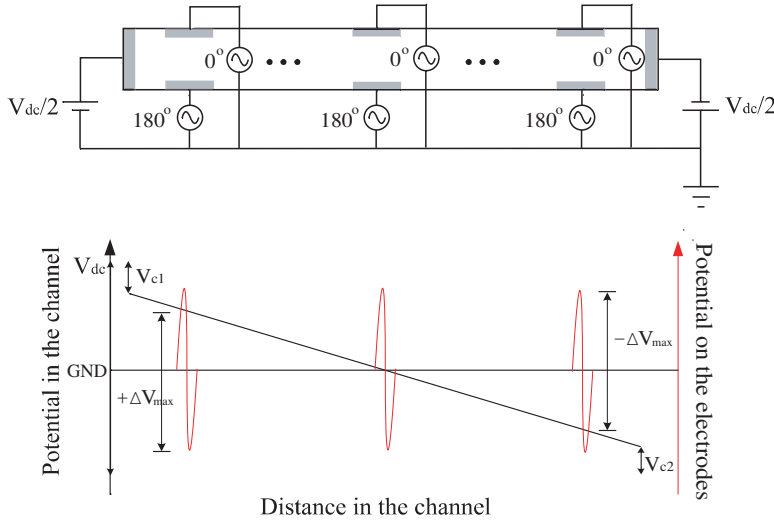


Figure 3.30: Schematic view of the electrical potential in the channel and the electrical potential on the electrodes distributed along the channel.

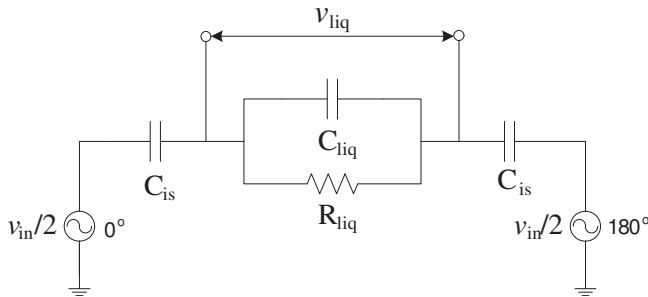


Figure 3.31: Equivalent electrical circuit of the DEP actuator.

the insulating films. The thicker the insulating film is, the higher voltage will be required to keep the same voltage drop on the liquid. The relation between the voltage applied on electrodes and the voltage difference over the liquid is given by

$$v_{liq} = \frac{Z_{liq}}{Z_{liq} + 2Z_{is}} v_{in} \quad (3.38)$$

When the liquid used is DEMI water which has a conductivity of around  $1\mu\text{S}/\text{m}$ , the  $R_{liq}$  will be much larger than the  $C_{is}$  at the frequency above MHz. The electrical model for the liquid can be simplified to a capacitor  $C_{liq}$ . To have a  $v_{liq}$  on the liquid, the  $v_{in}$  applied on the electrodes will be

$$v_{in} = v_{liq} \left( 1 + 2 \frac{C_{liq}}{C_{is}} \right) \quad (3.39)$$

The capacitance can be retrieved by considering it as a parallel plate capacitor whose dimension is related to the electrodes' area  $A$  and to the material thickness  $d$ .

$$C = \varepsilon_0 \varepsilon_r \frac{A}{d} \quad (3.40)$$

For the top-and-bottom focusing electrodes, assuming the depth of the channel  $d_{liq}$ , the dielectric constant of the liquid  $\varepsilon_{liq}$  and the dielectric constant of the insulating film  $\varepsilon_{is}$ , (3.39) becomes

$$v_{in} = v_{liq} \left( 1 + 2 \frac{\varepsilon_{liq}}{\varepsilon_{is}} \frac{d_{is}}{d_{liq}} \right) \quad (3.41)$$

Given the peak to peak voltage required on the liquid is  $V_{pp}$ , the maximum difference between the potential on the electrode and the local DC potential in the channel therefore takes this form

$$\Delta V_{max} = \frac{V_{pp}}{2} \frac{\varepsilon_{liq}}{\varepsilon_{is}} \frac{d_{is}}{d_{liq}} + \frac{V_{pp}}{4} + \frac{V_{dc} - V_{c1} - V_{c2}}{2} \quad (3.42)$$

$V_{c1}$  and  $V_{c2}$  are the contact voltage drops at the anode and at the cathode, respectively. Thus,  $V_{dc} - V_{c1} - V_{c2}$  is the voltage drop on the separation channel.  $\Delta V_{max}$  as a function of  $d_{is}$  is plotted in Figure 3.32, which is a straight line with a slope of  $\frac{\varepsilon_{liq} V_{pp}}{2 \varepsilon_{is} d_{liq}}$ . The film thickness required to avoid breakdown at different  $\Delta V_{max}$  is also marked in the same figure, which is in the dark area below the straight line with the slope of  $10^8$ . When the slope of (3.42) is larger than  $10^8$  (e.g. when a very high  $V_{pp}$  is required), breakdown will definitely happen no matter how thick the insulating film is. When the slope is smaller than  $10^8$ , as shown in Figure 3.32, the required minimum film thickness can be calculated by solving the cross

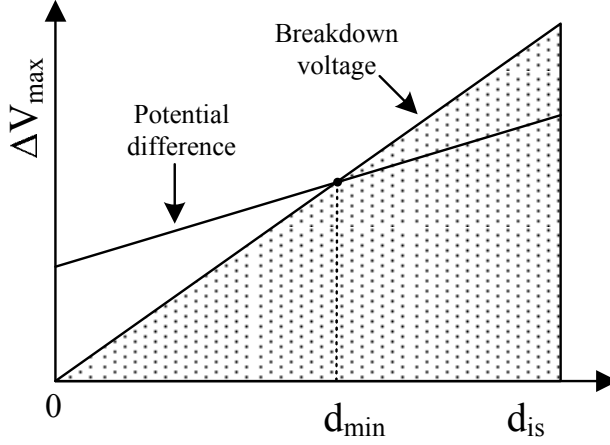


Figure 3.32:  $\Delta V_{max}$  as a function of  $d_{is}$  plotted together with the breakdown voltage.

point of these two lines. For instance, given  $d_{liq} = 20 \mu\text{m}$ ,  $\epsilon_{liq} = 80$ ,  $\epsilon_{is} = 4$ ,  $V_{pp} = 20 \text{ V}$  and  $V_{dc} - V_{c1} - V_{c2} = 40 \text{ V}$ , at least 278 nm oxide has to be used for prevention of breakdown in the focusing segments.

For the electrodes on two sides of the curves, they are quite far away from each other. Since the liquid capacitance between the electrodes is much lower than the capacitance of the insulating film, the voltage on the liquid is almost equal to the voltage applied to the electrodes. If the maximum potential on the AC electrodes is  $\pm 20 \text{ V}$ , an insulating film which withstands 30 V will be sufficient to avoid the breakdown. Based on (3.37), the minimal oxide thickness for prevention of breakdown in the curves is 300 nm.

Comparing the minimum required oxide thickness in the curves with that in the focusing segments, the larger one will be the minimum required oxide thickness for the whole device. As it was calculated above,  $d_{min} = 300 \text{ nm}$  in the curves (to have an effective peak to peak voltage of 40 V on the liquid) is larger than  $d_{min} = 278 \text{ nm}$  in the focusing segments (to have an effective peak to peak voltage of 20 V on the liquid), 300 nm will be chosen as the minimum oxide thickness for the device.

### 3.5.4 AC perturbation on the flow

At the time the electric field is applied on the microchannel, the ions in the diffuse double layer start moving along the field. The momentum is transferred to the bulk flow by the viscous diffusion. During this time, the velocity field across the

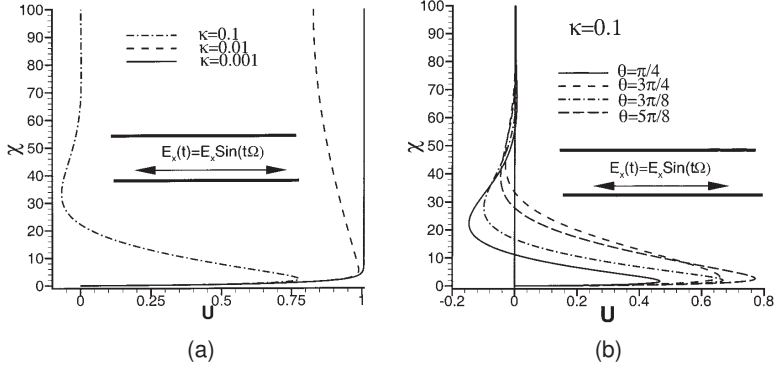


Figure 3.33: Velocity distribution of time-periodic electroosmotic flow (a) for various values of  $\kappa$  at time  $\theta = \pi/2$  and (b) for  $\kappa = 0.1$  at different times (adapted from [63]).

channel is time-dependent. Beyond this time scale, the velocity field becomes distinctly time independent, i.e. the flow reaches the steady state. The time  $\tau_{EOF}$  for the EOF flow to reach the steady state in a microchannel with diameter  $d$  filled with a liquid with density  $\rho$  is given by [62]

$$\tau_{EOF} = \frac{\rho d^2}{\eta} \quad (3.43)$$

From (3.43) it can be seen that for water based solutions in a microchannel with the diameter of  $20 \mu\text{m}$  the time needed for the establishment of the EOF will be in the sub millisecond range.

When a very high frequency AC is applied on a microchannel, the viscous diffusion is not fast enough to allow the bulk flow to respond to instantaneous changes in the applied electric field. Therefore, the flow will be only confined to a region near the channel wall while the bulk fluid remains essentially stationary. Dutta and Beskok developed an analytical model to predict the time periodic electroosmotic flow in a straight channel [63]. The result of the velocity distribution of time-periodic electroosmotic flow for various values of  $\kappa$  at time  $\theta = \pi/2$  is shown in Figure 3.33a.  $\kappa = (\Omega\lambda^2/\nu)^{1/2}$  is a nondimensional parameter that is a function of Debye length ( $\lambda$ ), the kinematic viscosity ( $\nu$ ), and the electric field excitation frequency ( $\Omega$ ).  $\kappa = 0.1, 0.01$ , and  $0.001$  correspond to the excitation frequencies of 1 MHz, 10 KHz, and 100 Hz, in the case of  $\lambda = 100 \text{ nm}$  and  $\nu = 1.0 \times 10^{-6} \text{ m}^2/\text{s}$ . The vertical-axis in the figure is the height ( $\chi = y/\lambda$ ) from the channel wall.  $\chi = 100$  corresponds to a channel half height  $h = 100\lambda = 10 \mu\text{m}$ . For the  $\Omega = 100 \text{ Hz}$  case, the viscous diffusion has enough time to respond and thus result in a quasi-steady velocity distribution that resembles the flat velocity obtained in



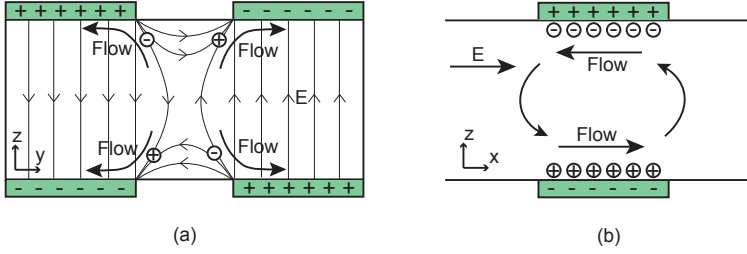


Figure 3.34: Schematics illustrating the induced charge electroosmotic flows (a) in the channel cross-section perpendicular to the flow and (b) in the channel cross-section parallel to the flow.

steady electroosmotic flows. When the frequency is increased to 10 KHz, the bulk flow velocity starts to deviate from the flat profile. For  $\Omega = 1$  MHz, the velocity becomes practically zero in the channel center at any time, as shown in Figure 3.33b.

Before entering the curves, the particles have already been focused to the channel center in both the horizontal and the vertical direction by the top-and-bottom electrodes. Therefore, the time-periodic flow near the channel wall will not affect the movement of the particles in the curves if the applied electric field frequency is in the MHz range. Even though the large particles will experience a time-periodic flow at outer tracks that are close to the sidewall, the time-periodic flow will give a zero time-averaged displacement to the particles in the curves.

### 3.5.5 Induced charge electroosmosis

The top-and-bottom focusing electrodes in the straight segments will induce time-periodic ionic charge above the electrode areas. Under the influence of the AC electric field (generated by the focusing electrodes) and the DC electric field (generated by the DC electrodes at the inlet and the outlet), the diffuse charge will move along the direction of the electric field and in turn result in the fluid flow through viscous interactions. In the channel cross-section perpendicular to the flow, there will be steady flow components subjecting to the AC electric field as shown in Figure 3.34a. While, in the channel cross-section parallel to the flow, there will be time-periodic flow components subjecting to the DC electric field as shown in Figure 3.34b. The fluid flows in this region will be the sum of the flow components in two different directions.

The fluid flow induced by an AC electric field on coplanar microelectrodes has already been demonstrated [13–15]. When the frequency is very low, the ions will have enough time to accumulate on the electrodes and screen out most of the electric field in the electrolyte. The steady flow components subjecting to the

AC electric field can be suppressed. However, the time-periodic flow components subjecting to the DC electric field will be significant. When the frequency is so high that its time period is shorter than the charging time  $\tau_c$  of the electrical double layer, all the induced charge electroosmotic flows will vanish due to the absence of the diffuse layer. The charging time  $\tau_c$  can be derived as the “RC time” of a liquid resistor in series with a double-layer capacitor. The liquid resistance (per unit area) can be calculated as

$$R_{liq} = \frac{L}{\sigma_{liq}} = \frac{\lambda_D^2 L}{\varepsilon_{liq} D} \quad (3.44)$$

where  $L$  is the electrode separation,  $\sigma_{liq}$  is the conductivity of the liquid,  $\varepsilon_{liq}$  is the permittivity of the liquid,  $\lambda_D$  is the Debye screening length and  $D$  is the ion diffusivity. The double layer capacitance (per unit area) can be estimated from the Debye-Huckel theory as

$$C_D = \frac{\varepsilon_{liq}}{\lambda_D} \quad (3.45)$$

Therefore, the charging time takes this form

$$\tau_c = R_{liq} C_D = \frac{\lambda_D L}{D} \quad (3.46)$$

When the electrode is covered by an insulating film, the capacitance of the insulating film will be much smaller than the double layer capacitance. In this case, the insulating film capacitor can be nearly considered as the capacitor in the RC network. Thus, the charging time will become

$$\tau_c = \frac{L \varepsilon_{is}}{\sigma_{liq} d_{is}} \quad (3.47)$$

where  $\varepsilon_{is}$  and  $d_{is}$  are the permittivity and thickness of the insulating film, respectively. So, the applied frequency should be higher than  $1/\tau_c$  in order to suppress the induced charge electroosmosis on the AC electrodes.

### 3.5.6 Heterogeneous $\zeta$ -potential

Connecting the isolated electrodes distributed along the channel to the same voltage supplier, as shown in Figure 3.30, makes them all have the same DC offset. The potential in the liquid decreases linearly along the channel since a DC voltage is applied over the entire channel to generate the EOF. The difference in the DC potentials on the electrodes with respect to the liquid potential in the channel will

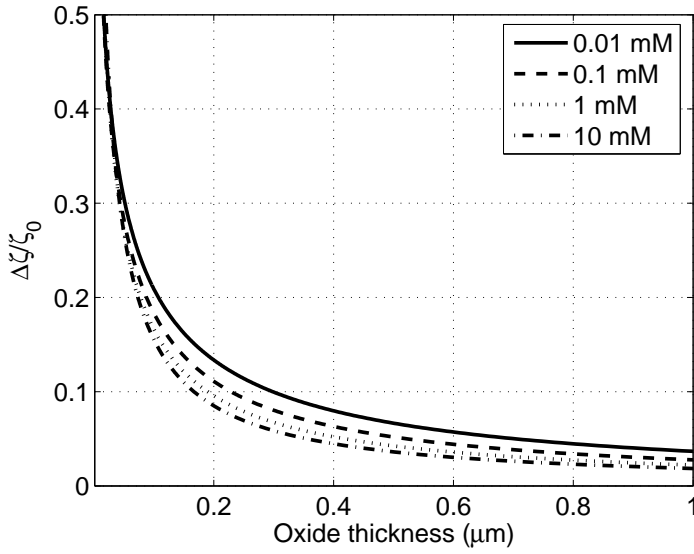


Figure 3.35:  $\zeta$ -potential change induced by isolated electrodes normalized to the natural  $\zeta$ -potential versus the thickness of the insulating film, at different ion concentrations.

result in heterogeneous  $\zeta$ -potentials, which will cause unwanted flow disturbance and thus will deteriorate the separation.

The  $\zeta$ -potential change (with respect to the nature  $\zeta$ -potential) induced by a 1 V voltage drop as a function of the film thickness (i.e. silicon oxide) was calculated and is shown in Figure 3.35. It can be seen from the figure that the influence of the electrode DC potential on the induced  $\zeta$ -potential change decreases as the thickness of the insulating film increases. Therefore, the flow disturbance caused by the heterogenous  $\zeta$ -potential can be minimized by increasing the thickness of the insulating film.

## 3.6 Hydrodynamic DEP separation in iterative curves

### 3.6.1 Flow profile comparison

The velocity profile of a hydrodynamic flow in the curve is parabolic with the peak velocity located slightly to the inner side of channel center. The flow velocity thus decreases monotonously from the channel center to the outer sidewall, which means the DEP separation in iterative curves could also be achieved with hydrodynamic flows. Both the hydrodynamic and the electrokinetic flow profiles in the same curve were simulated and are shown in Figure 3.36. The electrokinetic flow velocity decreases almost linearly and thereby has an almost constant velocity gradient across the channel. The velocity gradient of the hydrodynamic flow near the channel center is similar to that of the electrokinetic flow. And the gradient increases dramatically as the position comes closer to the outer sidewall. Hence, the separation in the presence of hydrodynamic flow is expected to have a higher efficiency while the separation in the presence of electrokinetic flow is expected to have a higher linearity.

### 3.6.2 Design principle

The principle schematic of the design is illustrated in Figure 3.37. The pressure difference on the separation channel governs a parabolic flow profile and drives the sample mixture forward along the channel. The AC voltages applied on the curves generate high non-uniform electric fields in the curves. For the negative DEP particles, the DEP force acts along the radius of the curves to the outside. The larger particles will be driven more to the outside of the curves. Since the flow velocity decreases monotonously from the channel center to the outer channel wall, the larger particles following the outer path will be left behind. For the curves are bended in the opposite directions, the separation will be canceled to a great extent. Therefore, the top-and-bottom focusing electrodes are used in the straight

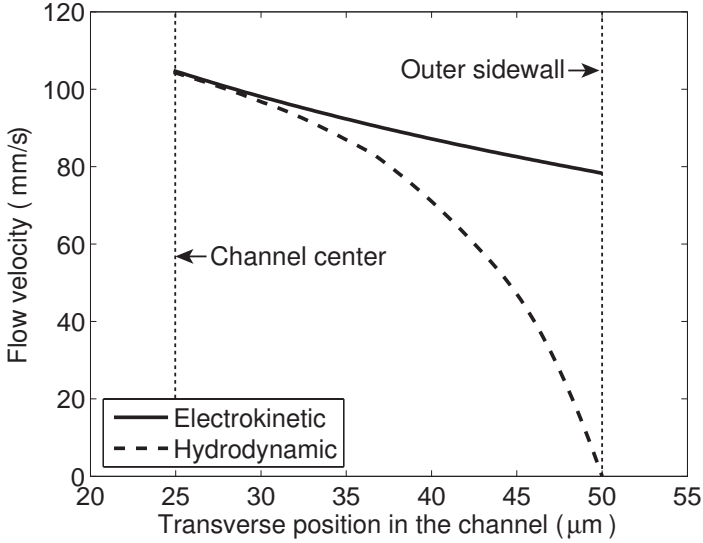


Figure 3.36: Comparison between the electrokinetic and the hydrodynamic flow profiles in a curve.

segments to bring all the particles to the channel center before entering the next curve. After a number of iterative curves, particles will get fully separated.

The hydrodynamic DEP separation has several advantages over the electrokinetic DEP separation. It could achieve a higher separation efficiency since the velocity gradient in the curves is larger. It eliminates the flow disturbance yielded by the heterogeneous  $\zeta$ -potential and the induced charge electroosmosis in the flow direction. The AC electrodes in the channel are not necessary to be insulated by the dielectric films any more, which reduces the process complexity and relieves the voltage required on the electrodes.

### 3.6.3 Simulation results

In Comsol multiphysics 3.4, an electrostatics module was used to calculate the electric field in the channel. A Stokes module was selected for the flow simulation. A 3D model for a microchannel containing 4 curves was built with the dimensions and the boundary conditions as listed in Table 3.4. Differing from the electrokinetic DEP separation, the fluid flow here is generated not by a DC voltage but by a pressure difference. The electrode edges and the inner side of the curves were expected to have the highest electric field gradients and therefore the meshes at those places should be defined relatively fine. After meshing, the velocity field

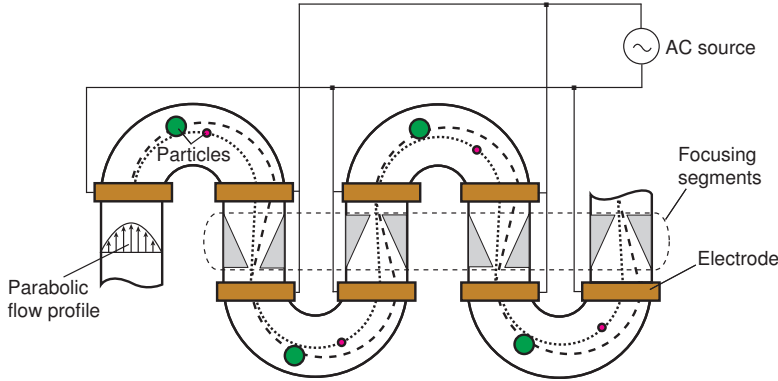


Figure 3.37: Principle schematic of the hydrodynamic DEP separation in iterative curves.

Table 3.4: Simulation parameters.

Simulation parameter	Value
Voltage on the curves ( $V_{rms}$ )	40 V
Voltage on the focusing electrodes ( $V_{rms}$ )	6 V
Poiseuille flow velocity ( $v_{max}$ )	100 $\mu\text{m/s}$
Channel width	50 $\mu\text{m}$
Channel depth	20 $\mu\text{m}$
Curve inner wall radius	50 $\mu\text{m}$
Simulation timeframe	19.6 s
Time step	50 ms

was calculated in the global coordinate system with finite element method. After the channel geometry and the field values were imported to the Matlab 7.0, the field-dependent force acting on the particle was calculated which defines the velocity of the particle and in turn the distance it travels in a short time step. Finally, the particle trajectory was retrieved by summing all short distances the particle traveled in a short time.

Firstly, the trajectories of two types of particles, i.e. 100 nm and 300 nm radius particles, were simulated and the result is shown in Figure 3.38. After 19.6 s, the 100 nm radius particle arrives at the end and the 300 nm radius particle is left behind. Compared with the simulated trajectories in the presence of electrokinetic flow as shown in Figure 3.26, the separation achieved here in the presence of hydrodynamic flow is relatively larger. The retention time for the particles with radii of 100-400 nm was then simulated and is listed in Table 3.3. The retention

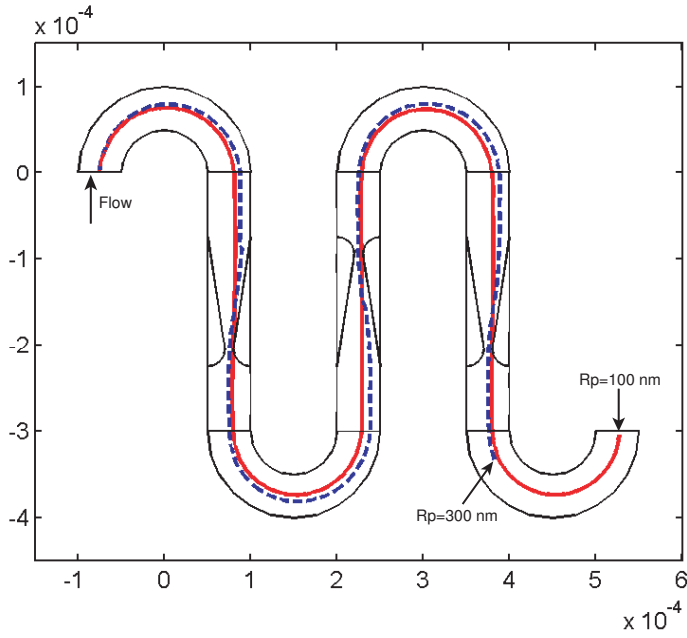


Figure 3.38: Top view of a fragment of the hydrodynamic DEP separation channel containing 4 curves and the simulated trajectories for two different types of particles (i.e. 100 nm and 300 nm radius particles).

Table 3.5: Simulated retention time of different size particles.

Particle radius (nm)	Retention time (s)
100	19.6
150	19.9
200	20.5
250	21.1
300	22
350	23.3
400	25

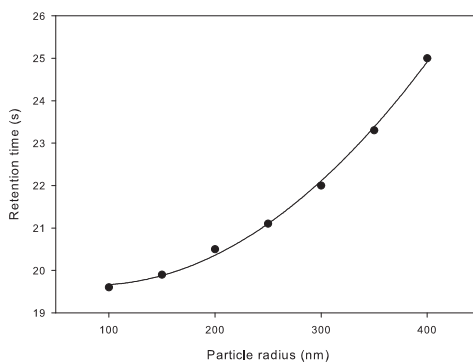


Figure 3.39: Simulated retention time as a function of particle size in the hydrodynamic DEP separation channel containing 4 curves.

time as a function of the particle size is plotted in Figure 3.27, from which it can be seen that the retention time has an almost second order dependence on the particle radius.



## Chapter 4

# Moving Field Capillary Electrophoresis

As introduced in Chapter 2, Capillary Electrophoresis (CE) is a very useful technique in various biochemical applications. However, high voltage levels are an issue for current microchip electrophoresis. In CE electric fields up to 500 V/cm are required for separation. Given that, (even on CE-microchips) the separation channel length is still several cm long, high voltages up to several kilovolts are required. The required strong power supplies limit the portability of the system and prevent complete integration with microelectronic read-out circuitry. Even though a compact battery-powered high-voltage power supply (weight 0.2 kg) has been developed [64], which is a major improvement over the conventional bench-top supply, there is still room for improvement. The recently introduced concept of moving field CE [65, 66] can relieve the high-voltage requirement to a great extent (Figure 4.1). In this method the channels contain multiple electrodes and the separation voltage is switched between these electrodes in such a way that it is always applied to that small part of the channel where the sample plug resides. Therefore, the separation field travels with the sample plug through the channel. Since the distance between the electrodes is small, adequate field strength can be maintained using low voltages (e.g. below 100 V).

### 4.1 Plug dispersion in moving field CE

Although the concept of moving field CE was proposed long time ago [65], there has been no experimental result published to prove this concept. That is because the flow profile distortion is still a serious problem remaining unaddressed. The electroosmotic flow profile between the active electrodes is flat in the ideal case.

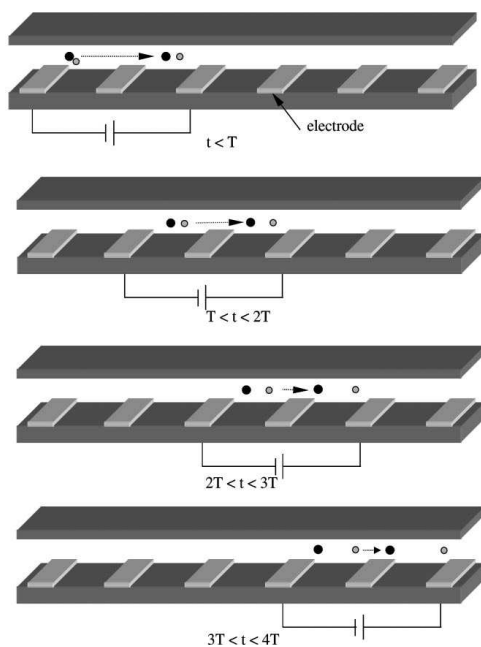


Figure 4.1: Schematic view showing the concept of moving field CE (adapted from [66]).

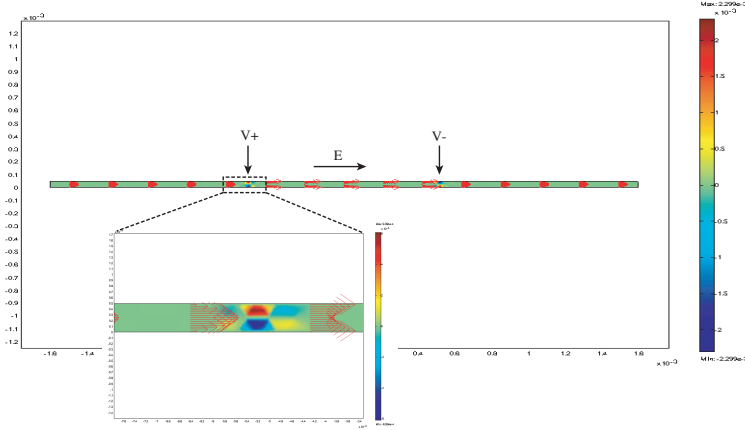


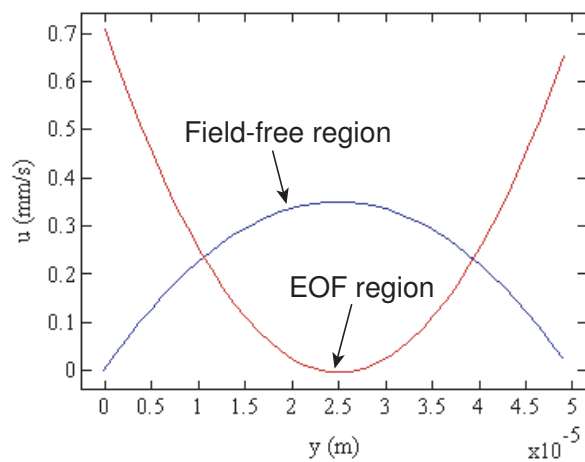
Figure 4.2: Simulation of plug dispersion when a voltage is applied on a fraction of the channel.

However, the flow profile of the electroosmotic flow will be largely distorted when the voltage is applied over a small segment of the channel. Pushing the liquid ahead and dragging the liquid behind will build up a pressure difference between two ends of the EOF region. This back pressure will result in an anti-parabolic flow profile. Outside this region, in the field free regions, the flow profile will tend to be a parabolic shape. No research has been reported on how far the flow profile transitions extend into the EOF region. This is rather important since a disturbed flow profile will introduce sample plug dispersion and peak broadening.

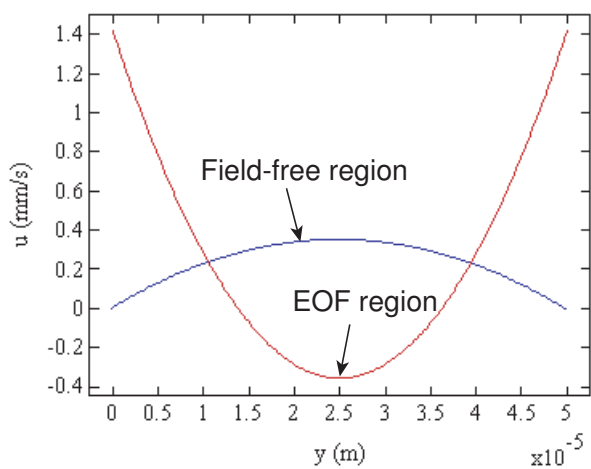
Extensive finite element simulations have been performed on flow profiles and related sample dispersion that can be expected in moving electric fields. The flow in the osmotic region is largely deformed by the pressure drop in the other sections much more than on forehand was expected, see Figures 4.2. And this will of course invoke large sample plug dispersion.

Figure 4.3a and Figure 4.3b exhibit the flow profiles in different regions of the channel when a given voltage is applied over 1/3 and 1/6 of the channel, respectively. The flows in the EOF region and the field-free region are closely related. The following conclusions can be drawn:

- The velocity in the field-free region solely depends on the separation voltage (not the fraction of the channel it is applied to).
- For a given voltage, the smaller fraction it is applied on, the larger profile distortion will be caused in the EOF region.



(a)



(b)

Figure 4.3: Simulated flow profiles in different regions of the channel when a voltage is applied over (a) 1/3 and (b) 1/6 of the channel.

Table 4.1: Equivalent elements of the fluid system and the electrical system.

Fluid System	Electrical System
Flow resistance	Electrical resistance
Pressure difference	Voltage
Volumetric flow rate	Current
Flow velocity	Current density
Electroosmosis	Current source

---

## 4.2 Electrical analogy of fluid system

The Hagen-Poiseuille equation is a well-known law that describes laminar flow through a channel with a circular cross-section. It is written in the form of [67]

$$\Delta P = \frac{8\eta L Q}{\pi r^4} \quad (4.1)$$

where  $\Delta P$  is the pressure drop,  $L$  is the length of the channel,  $\eta$  is the dynamic viscosity,  $Q$  is the volumetric flow rate, and  $r$  is the radius of the circular cross-section. From this equation, we could extract the flow resistance, which is independent of flow and pressure.

$$R_f = \frac{8\eta L}{\pi r^4} \quad (4.2)$$

From the Hagen-Poiseuille equation, we could see that the flow and resistance are reciprocally related, an increase in resistance decreases flow at any given pressure difference. Also, at any given flow along a channel, an increase in resistance increases the pressure difference. It is rather analogous to the electric model where the voltage, current and the electrical resistor have a similar relation. Poiseuille's law is also similar to Ohm's law for electrical circuits. The equivalent elements of the fluid system and the electrical system are extracted and listed in Table 4.1.

By means of the analog electrical model, the cause of the plug dispersion in the EOF region of the moving field CE system can be explained in an innovative way. Based on the equivalent elements, the equivalent circuit of the fluid channel with a voltage applied on one segment can be drawn as shown in Figure 4.4. For there is no pressure difference over the whole channel, two ends of the electrical circuit are both grounded and have equal potential. The EOF segment is acting as a non-ideal current source, which is composed of an ideal current source and a paralleled internal resistor. The rest part of the channel is analogous to a load resistor which is connected to the non-ideal current source. Apparently, there will be an electrical current flowing through the internal resistor from right to left, which corresponds to a back flow in the fluid system. The amplitude of the

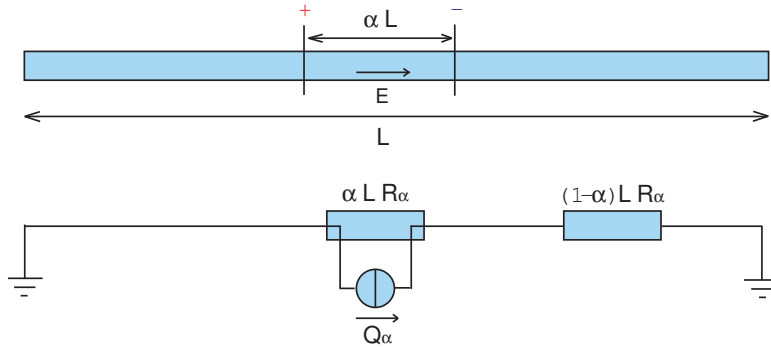


Figure 4.4: Electrical analog model for the fluid system in which a DC voltage is applied over a segment of the channel.

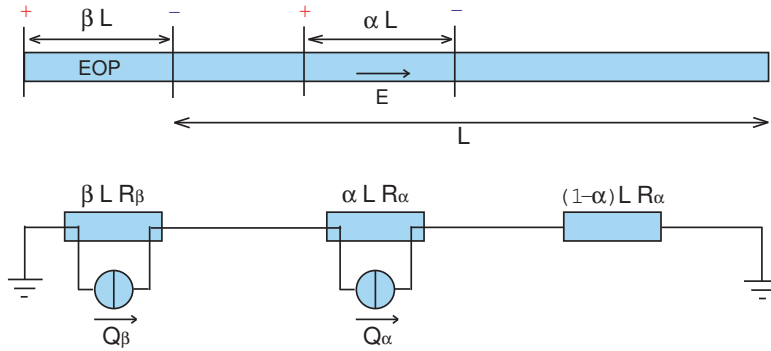


Figure 4.5: Electrical analog model for the plug dispersion compensation method.

back flow (i.e. the current through the internal resistor) depends on the ratio of the load resistance to the internal resistance. The back flow generates a reversed pressure drop on the EOF segment, which leads to a reversed parabolic flow profile. The reversed parabolic profile combined with the flat profile results in an anti-parabolic profile in the EOF segment.

### 4.3 Compensation by an electroosmotic pump

The method we propose to compensate the back flow is to generate, by coupling an electroosmotic pump (EOP), a forward flow and cancel the back flow in the EOF segment. When an EOP is connected to the separation channel, the electrical analog model for the fluid system can be drawn as illustrated in Figure 4.5. By

calculating the current in the equivalent circuit, we could easily retrieve the flow in each segment of the channel. Therefore, if assuming the length of the separation channel, EOF segment and EOP segment are  $L$ ,  $\alpha L$  ( $0 < \alpha < 1$ ) and  $\beta L$  ( $0 < \beta < 1$ ), respectively. The backward flow component in the EOF segment caused by the separation voltage alone can be derived and takes the form:

$$Q_{back,\alpha} = Q_\alpha \frac{\frac{1}{\alpha LR_\alpha}}{\frac{1}{\alpha LR_\alpha} + \frac{1}{\beta LR_\beta + (1-\alpha)LR_\alpha}} \quad (4.3)$$

where  $R_\alpha$  and  $R_\beta$  are the unit length flow resistance of the EOF segment and the EOP segment, respectively. And  $Q_\alpha$  is the electroosmotic flow in the EOF segment. Similarly, the forward flow component in the EOF segment generated by the EOP alone (i.e. the output flow of EOP) can also be calculated and takes the form

$$Q_{forward,\alpha} = Q_\beta \frac{\frac{1}{LR_\alpha}}{\frac{1}{LR_\alpha} + \frac{1}{\beta LR_\beta}} \quad (4.4)$$

where  $Q_\beta$  is the electroosmotic flow in the EOP segment. For a full plug distortion compensation, both forward and backward component should have the same amplitude, that is

$$Q_{back,\alpha} = Q_{forward,\alpha} \quad (4.5)$$

The volumetric electroosmotic flow which acts as the current source in the equivalent circuit can be calculated as the product of the electroosmotic velocity and the cross-section area of the channel. It can be described by the following equation

$$Q = v_{eof} A = -\frac{\varepsilon \zeta}{\eta} EA \quad (4.6)$$

where  $\varepsilon$  and  $\eta$  are the permittivity and viscosity of the aqueous solution, and  $\zeta$  is the zeta potential of the channel wall. Calculate  $Q_\alpha$  and  $Q_\beta$  with (4.6), then insert them to (4.3) and (4.4), then solve (4.5), the ratio of the EOP voltage to the separation voltage can be derived

$$\frac{V_\beta}{V_\alpha} = \frac{\zeta_\alpha}{\zeta_\beta} \frac{A_\alpha}{A_\beta} \left( \frac{\beta}{\alpha} + \frac{1-\alpha}{\alpha} \frac{R_\alpha}{R_\beta} \right) \quad (4.7)$$

In the above formula,  $V_\alpha$  is the separation voltage applied on the EOF segment, which should be high enough to create sufficient electric field strength for the

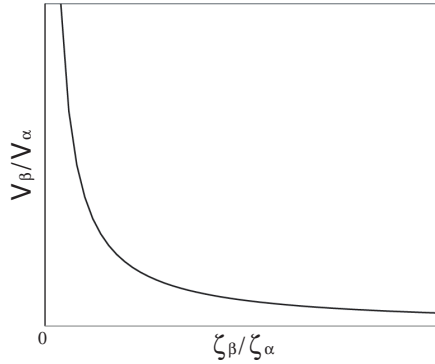


Figure 4.6: Required voltage ratio versus the  $\zeta$ -potential ratio.

electrophoretic separation. For instance, a 10 V will be required on a 1 mm long segment if a 100 V/cm electric field is desired for separation.  $V_\beta$  is the voltage required on the EOP segment for compensation. And this EOP voltage is preferably to be in the same scale as the separation voltage, i.e.  $V_\beta/V_\alpha$  is close to 1.

It can be seen from (4.7) that the voltage ratio is inversely proportional to the ratio of the  $\zeta$ -potential in EOP segment to the  $\zeta$ -potential in EOF segment, as depicted in Figure 4.6. By surface coating, the  $\zeta$ -potential in the EOP segment will be increased and thus the EOP voltage required for compensation can be relieved. However, it is rather difficult to do local surface coating in the microchannel. In a later section, a method to modify the channel  $\zeta$ -potential by embedded electrodes will be discussed.

When the channels are with homogeneous  $\zeta$ -potential, the voltage ratio becomes

$$\frac{V_\beta}{V_\alpha} = \frac{\beta}{\alpha} \frac{A_\alpha}{A_\beta} + \frac{1-\alpha}{\alpha} \frac{R_\alpha}{R_\beta} \frac{A_\alpha}{A_\beta} \quad (4.8)$$

The voltage ratio decreases with the decrease of the EOP length (Figure 4.7). That is because when  $\beta$  is decreased, a lower EOP voltage will be adequate to maintain the same EOP output flow in spite of a small decrease in the internal resistance. Moreover, a shorter  $\beta$  will cause less backward flow in the EOF segment. Therefore, decreasing the EOP length is a way to relieve the EOP voltage. However, decreasing the EOP length will increase the electric field in the EOP segment. And the extent of the voltage relieve is quite limited, as shown in Figure 4.7, even with an extremely short EOP and thus an extremely high electric field. When the EOP segment has the same cross-section as the separation channel. The voltage ratio becomes:



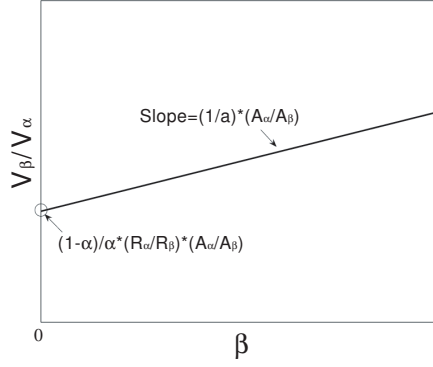


Figure 4.7: Required voltage ratio versus  $\beta$  length.

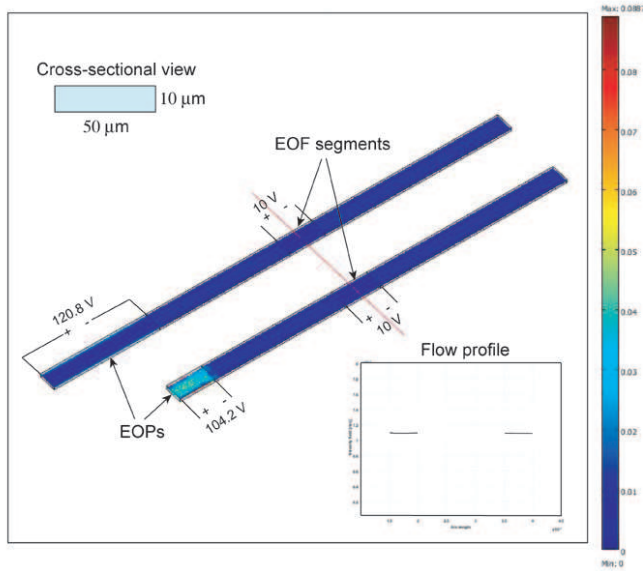


Figure 4.8: Simulation results showing how  $\beta$  length influences the required EOP voltage for plug dispersion compensation.

$$\frac{V_\beta}{V_\alpha} = \frac{\beta}{\alpha} + \frac{1 - \alpha}{\alpha} \quad (4.9)$$

If let  $\alpha = 0.1$ , and  $V_\alpha = 10$  V,  $V_\beta$  required is 100 V and 120 V respectively for  $\beta = \alpha$  and  $\beta = 3\alpha$ . The simulated results are in very good agreement with the calculated results, as can be seen in Figure 4.8. In these cases, the EOP voltages are more than 10 times of the separation voltage. Even if by decreasing  $\beta$  further, the required EOP voltage still has to be at least 9 times of the separation voltage no matter how short the EOP segment becomes.

Although the separation voltage can be reduced to a great extent in moving field CE, the several tens (or even hundreds) of times higher EOP voltage required for the compensation will totally wipe out the advantage of moving field CE. So, instead of decreasing  $\beta$ , more advanced solutions to relieve the EOP voltage will be investigated in the next section.

## 4.4 Relief of the pump voltage

### 4.4.1 By well-designed channel structures

Here we consider a situation in which the EOP segment consists of several sub-channels in parallel. Assuming that the cross-sectional area of each subchannel is  $A_\beta$  and the number of subchannel is  $n$ , the voltage ratio becomes

$$\frac{V_\beta}{V_\alpha} = \frac{\beta}{\alpha} \frac{A_\alpha}{nA_\beta} + \frac{1 - \alpha}{\alpha} \left( \frac{D_{h,\beta}}{D_{h,\alpha}} \right)^2 \quad (4.10)$$

where  $D_{h,\beta}$  and  $D_{h,\alpha}$  are the hydraulic diameter of the subchannels in EOP segment and the separation channel, respectively. From the above formula, we could conclude that both following requirements should be met if the compensation is desired to be fulfilled with a low voltage:

- A large total cross-section area of all the subchannels is desired with respect to that of the separation channel.
- A small hydraulic diameter of each subchannel is desired with respect to that of the separation channel.

A large total cross-section area of the subchannels corresponds to a large current source for a given EOP voltage. A small hydraulic diameter of each pump channel results in a large internal resistance. A large current source with a large internal resistance provides a maximum output which can compensate the back flow in the EOF segment more efficiently.

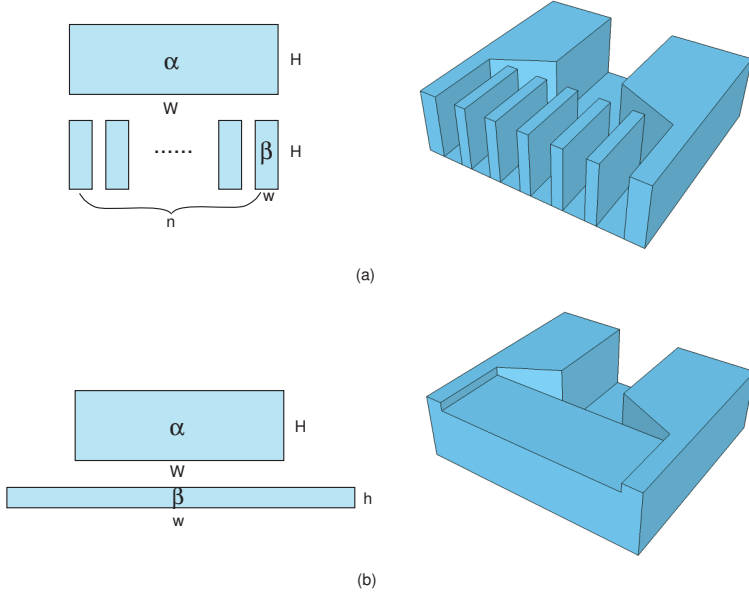


Figure 4.9: Proposed 2 EOP structures.

Two feasible EOP structures that meet both requirements are proposed. The first structure, as shown in Figure 4.9a, is to employ a number of high aspect ratio subchannels in parallel (i.e. a slender channel array) which have the same depth as the separation channel. In this case, the voltage ratio becomes

$$\frac{V_\beta}{V_\alpha} = \frac{\beta}{\alpha} \frac{W}{nw} + \frac{1-\alpha}{\alpha} \left(\frac{w}{H}\right)^2, w \ll H \ll W \quad (4.11)$$

where  $H$  is the depth of the channels,  $W$  and  $w$  are the width of the separation channel and each slender subchannel, respectively, and  $n$  is the number of the subchannels. By increasing the number of the subchannels, the first term on the right side of the equation could be reduced. And by decreasing the width of each subchannel, the second term could be reduced. In the way, the voltage ratio can be easily reduced to a value around 1. Given the channel dimensions shown in Figure 4.10 and the simulation parameters listed in Table 4.2, the simulated voltage ratio turns out to be 1.325, which is quite comparable with the calculated result 1.36. From the inlay, we could see the retrieved flat flow profile with only a 0.18 percent velocity variation.

The second proposed structure is to use a broad thin pump channel whose depth is much smaller than the depth of the separation channel as shown in Figure 4.9b. Thus, the voltage ratio becomes

Table 4.2: Parameters used in modeling and simulation.

Parameter	Symbol	Value
Separation channel length	L	1 mm
Separation channel width	W	50 $\mu\text{m}$
Separation channel depth	H	10 $\mu\text{m}$
EOF segment length	$\alpha L$	0.1 mm
EOP segment length	$\beta L$	0.1 mm
Separation voltage	V	10 V
$\zeta$ -potential	$\zeta_0$	-100 mV

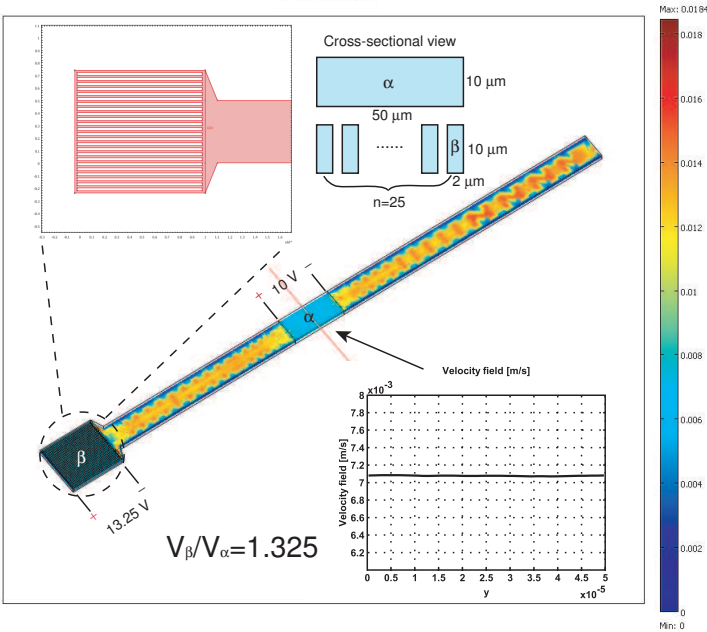


Figure 4.10: Simulated compensation results achieved by coupling a slender channel array.

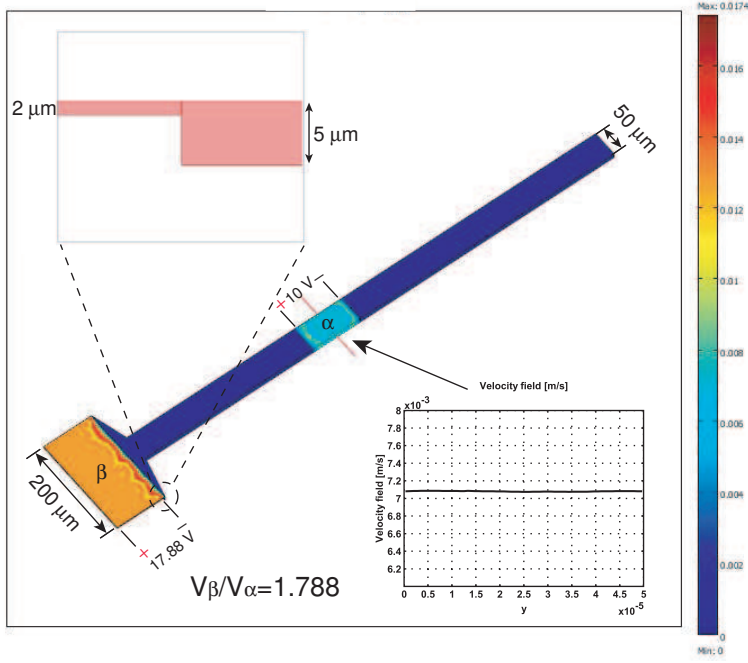


Figure 4.11: Simulated compensation results achieved by coupling a broad thin EOP.

$$\frac{V_\beta}{V_\alpha} = \frac{\beta WH}{\alpha wh} + \frac{1-\alpha}{\alpha} \left(\frac{h}{H}\right)^2, h \ll H \ll W \quad (4.12)$$

where  $h$  is the depth of the broad thin channel. Apparently, the feature of broadness makes the first term on the right side of the equation small and the feature of thinness makes the second term small. Given  $\alpha=\beta=0.1$ ,  $W=50 \mu\text{m}$ ,  $H=10 \mu\text{m}$ ,  $w=200 \mu\text{m}$  and  $h=2 \mu\text{m}$ , the simulated voltage ratio turns out to be 1.788 (Figure 4.11), which is also very comparable with the calculation result 1.61. The retrieved flat flow profile with a 0.17 percent velocity variation is shown in the inlay. The small variation between the simulation and calculation results is mainly due to the approximation of flow resistance in analytical calculation.

#### 4.4.2 By gate electrodes

In the first solution, the  $\zeta$ -potential is assumed to be uniform all over the channel surfaces. But as explained previously, the pump voltage could also be relieved by increasing the  $\zeta$ -potential of the EOP segment. Apart from surface coating,

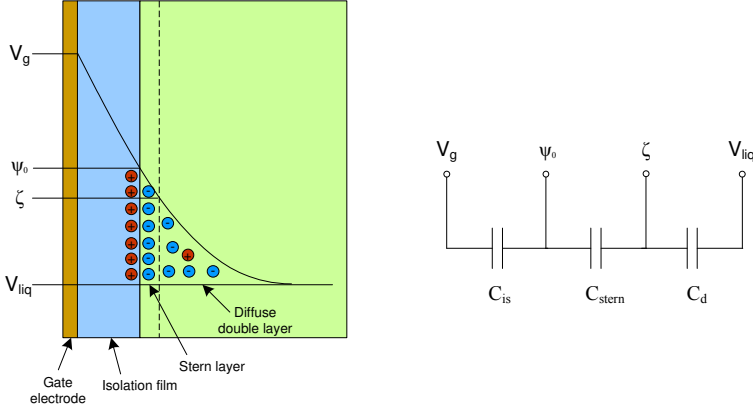


Figure 4.12: Overview of the potential decay and the equivalent circuit.

another way to modify the  $\zeta$ -potential of the channel walls is by using a gate electrode. In the proposed FlowFET [68] and Field Effect Flow Control (FEFC) devices [69], the electroosmotic flow was reported can be controlled by application of an external electric field perpendicular to the channel wall which is induced by a gate electrode. The perpendicular electric field changes the local  $\zeta$ -potential and thus the electrokinetic flow, which is proportional to the  $\zeta$ -potential, can be controlled. In this section, to what extent the  $\zeta$ -potential can be modified by the gate electrode will be investigated.

At moderate and low ionic strength, the capacitance of the Stern layer is generally much larger than that of the diffuse double layer. Therefore the voltage drop over the Stern layer is very small. If neglecting the Stern capacitor, the influence of the gate potential on the local  $\zeta$ -potential can be determined by the ratio between  $C_{is}$  and  $C_d$  as is illustrated in Figure 4.12.

$$\Delta\zeta = \frac{C_{is}}{C_d}(V_g - V_{liq}) \quad (4.13)$$

where  $V_g$  is the electric potential on the gate electrode and  $V_{liq}$  is the electric potential in the channel. The capacitance of the isolation film can be described as

$$C_{is} = \frac{\varepsilon_0 \varepsilon_r A}{d} \quad (4.14)$$

where  $A$  is the surface area of the gate electrode and  $d$  is the thickness of the film. The diffuse double layer capacitance is given by

$$C_d = \sqrt{\frac{2z^2q^2\varepsilon_0\varepsilon_r n_0}{\kappa T}} A \cosh\left(\frac{zq}{2\kappa T}\zeta_0\right) \quad (4.15)$$

In case of monovalent electrolyte at room temperature with a dielectric constant of 78.5. This equation can be simplified to [70]

$$C_d = 228.5 \times 10^{-6} A \sqrt{c} \cosh(19.46\zeta) \quad (4.16)$$

where  $\zeta = \zeta_0 + \Delta\zeta$ . And  $\zeta_0$  is the natural  $\zeta$ -potential which is electrolyte concentration dependent.  $\Delta\zeta$  is the  $\zeta$ -potential change induced by the gate electrode. The natural  $\zeta$ -potential,  $\zeta_0$ , can be calculated by equation

$$\zeta_0 = \frac{C_{stern}}{C_{stern} + C_d(\zeta_0)} \Psi_0 \quad (4.17)$$

where  $\Psi_0$ , the surface potential, is determined to be -0.25 V if considering the case of glass in contact with sodium acetate buffers of pH 7 [71]. Inserting (4.14) and (4.16) to (4.13) and solving (4.13), the  $\zeta$ -potential as a function of the gate potential can be obtained, which is plotted in Figure 4.13. When there is no voltage applied on the gate, the local  $\zeta$ -potential is equal to the negative natural  $\zeta$ -potential, which decreases with the increase of the buffer ion concentration. When the gate voltage is increased to a certain value, the external electric field completely balances the electric field generated by the build-in surface charges and therefore results in zero  $\zeta$ -potential. When the gate voltage is further increased, the  $\zeta$ -potential reverses its polarity and becomes even positive. The slope of the curves decreases rapidly with the increase of the gate voltage. That is because  $C_d$  increases rapidly with the increase of the  $\zeta$ -potential and thus ratio of  $C_{is}$  to  $C_d$  is decreased. It is also can be seen from the figure that the gate voltage has more influence on the  $\zeta$ -potential when the buffer concentration is lower.

Given  $\alpha = \beta$  and cross-section is the same, (4.7) can be simplified to

$$\frac{V_\beta}{V_\alpha} = \frac{\zeta_\alpha}{\zeta_\beta} \frac{1}{\alpha} = \frac{\zeta_0}{\zeta_0 + \Delta\zeta} \frac{1}{\alpha} \quad (4.18)$$

If let  $V_\alpha = V_\beta$ , the required  $\zeta$ -potential change induced by the gate electrode is equal to

$$\Delta\zeta = \frac{1 - \alpha}{\alpha} \zeta_0 \quad (4.19)$$

Given  $\alpha = 0.1$ , the  $\zeta$ -potential change induced by the gate electrode has to be 9 times of the natural  $\zeta$ -potential. Apparently, such high change cannot be achieved by the gate electrode with an acceptable voltage level, as can be seen in Figure

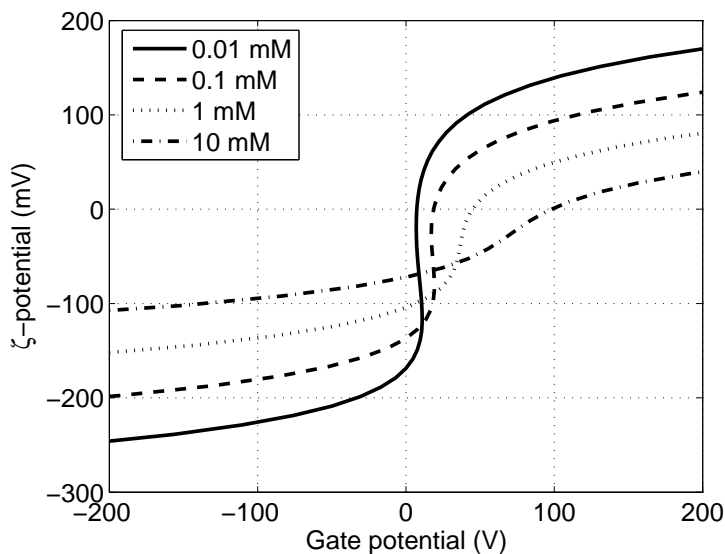


Figure 4.13:  $\zeta$ -potential as a function of the gate potential for different buffer concentrations.

4.13. By applying -50 V to the gate electrode, only about 30 % increase can be achieved in the magnitude of the  $\zeta$ -potential. Nevertheless, it might be a good idea if this method is used in combination with the EOP structures proposed in the previous section.

## 4.5 Prevention of flow loss

For the sample injection purpose, there will be side channels connecting to the main separation channel. During separation, the output flow of the EOP will leak into the side channels. Because of the flow loss, the forward flow in the EOF segment will not be sufficient any more to fully compensate the back flow. The arrows representing the flow velocity field in Figure 4.14 reveal that the flow velocity in the side channels is much higher than the flow velocity in the separation channel, as the side channels is normally shorter than the separation channel. As a result, the flow profile in the EOF segment turns anti-parabolic again, and the flow velocity becomes even negative at the center of the channel.

The equivalent circuit of the fluid system with flow loss is illustrated in Figure 4.15. Based on the circuit, the backward component generated by the separation voltage and the forward component generated by the EOP were derived and are



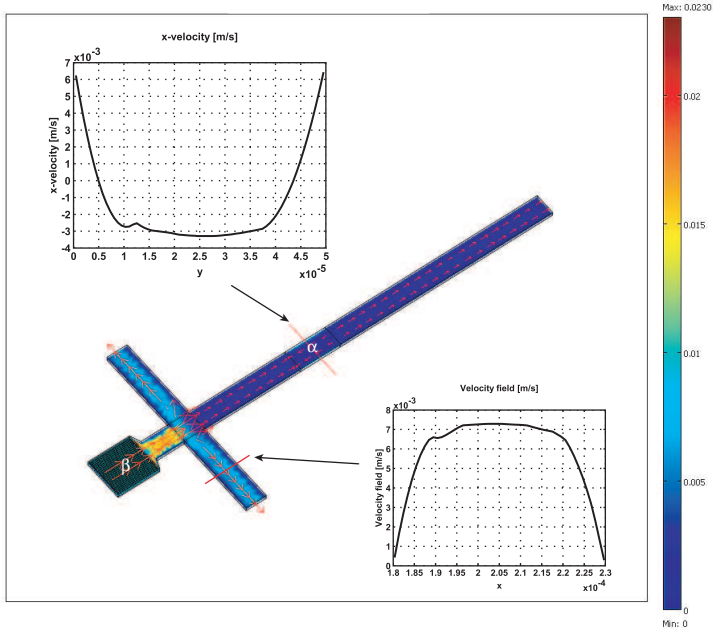


Figure 4.14: Simulation of flow loss via the side channels.

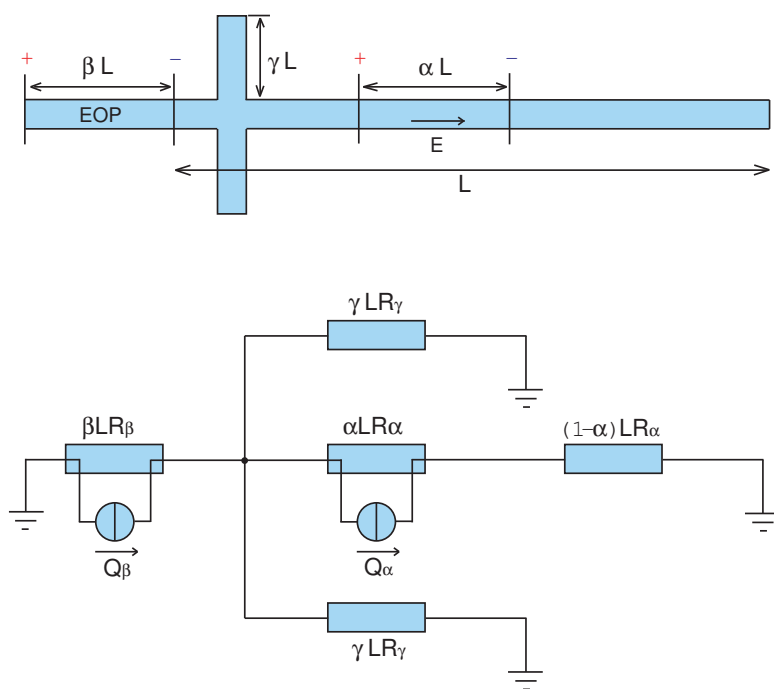


Figure 4.15: Equivalent circuit for the moving field CE with flow loss via the side channels.

exhibited in ((4.20)) and ((4.21)), respectively.

$$Q_{backward,\alpha} = Q_\alpha \frac{(1 - \alpha)LR_\alpha + \frac{\beta LR_\beta \frac{1}{2} \gamma LR_\gamma}{\beta LR_\beta + \frac{1}{2} \gamma LR_\gamma}}{LR_\alpha + \frac{\beta LR_\beta \frac{1}{2} \gamma LR_\gamma}{\beta LR_\beta + \frac{1}{2} \gamma LR_\gamma}} \quad (4.20)$$

$$Q_{forward,\alpha} = Q_\beta \frac{\frac{\beta LR_\beta \frac{1}{2} \gamma LR_\gamma}{\beta LR_\beta + \frac{1}{2} \gamma LR_\gamma}}{LR_\alpha + \frac{\beta LR_\beta \frac{1}{2} \gamma LR_\gamma}{\beta LR_\beta + \frac{1}{2} \gamma LR_\gamma}} \quad (4.21)$$

where  $\gamma L$  is the length of each side channel. The current generated by the current source  $Q_\beta$  will be split into three branches and two of them go to the ground through the resistors which are analogous to the side channels. The amount of the leakage current strongly depends on the resistance of these two resistors. Therefore, in order to minimize the flow loss, the flow resistance of the side channels has to be increased.

As explained previously, when a channel is divided into many high aspect ratio slender subchannels, the flow resistance of that channel will be greatly increased. This method could also be used here to increase the flow resistance of the side channels. And since the total cross-section area is not reduced much, the sample injection process will not be affected.

In order to evaluate the effectiveness of the slender channel arrays, the finite element method modeling was carried out. The width and the length of the slender subchannels in the side channels are  $2 \mu m$  and  $2 mm$ , respectively, and the rest of the simulation parameters are the same as shown in Figure 4.10 and Table 4.2. The simulated results depicted in Figure 4.17 shows that the flow profile in the separation segment becomes much less anti-parabolic with the slender channel arrays at the voltage ratio of 1.325. The flow velocity at the center of the channel becomes positive. By a very small increase of the voltage ratio to 1.496, the flat flow profile is retrieved with only 0.09 percent velocity variation.

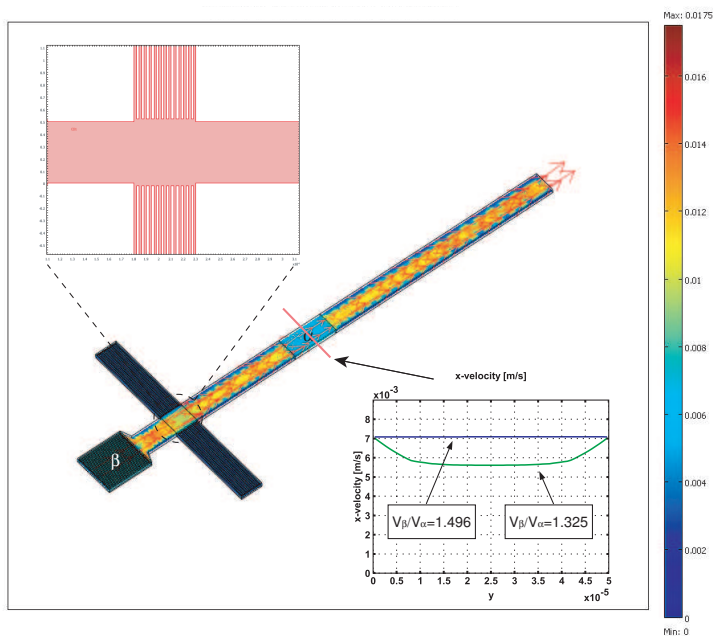


Figure 4.16: Simulated results showing, by employing slender channel arrays in the side channels, a small increase in the voltage ratio will be sufficient to balance the flow loss.

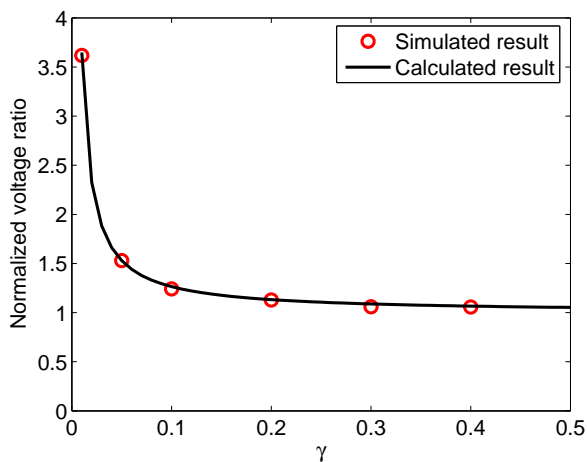


Figure 4.17: Simulated and calculated results depicting how much the voltage ratio has to be increased with respect to the none-side-channel case when  $\gamma$  is decreased.

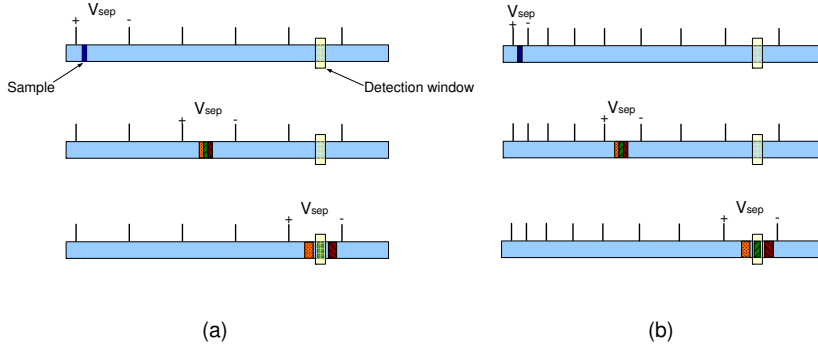


Figure 4.18: Comparison between (a) constant electric fields and (b) dynamic electric fields.

## 4.6 Constant electric fields versus dynamic electric fields

There are two methods to arrange the electrodes in the separation channel. The first method is to have them uniformly distributed in the channel with a fixed span, as shown in Figure 4.18a. In this method, the analytes experience constant electric fields during the entire period as they do in traditional CE, and thus the separation will increase linearly over time. The second method is to have the smallest electrode spans in the front and gradually increase the spans between the electrodes, as shown in Figure 4.18b. The narrow sample plug at the beginning of separation allows small electrode spans for yielding very strong electric fields. Sequentially, the electrode spans are increased based on the mobility difference of the analytes. In this method, the particles are exposed to dynamic electric fields. In contrast with the constant electric fields, the dynamic electric fields could achieve a faster separation since the time-averaged field value is much higher.

## 4.7 Single-side electrodes versus double-banked electrodes

Two different electrode configurations, single-side electrodes and double-banked electrodes, were compared with respect to the quality of the separation [72]. The electric potential distribution is nonuniform at the two ends of the separation segment (Figure 4.19a) in the case of single-side electrodes. The nature of the field distribution will result in a velocity gradient since it is proportional to the

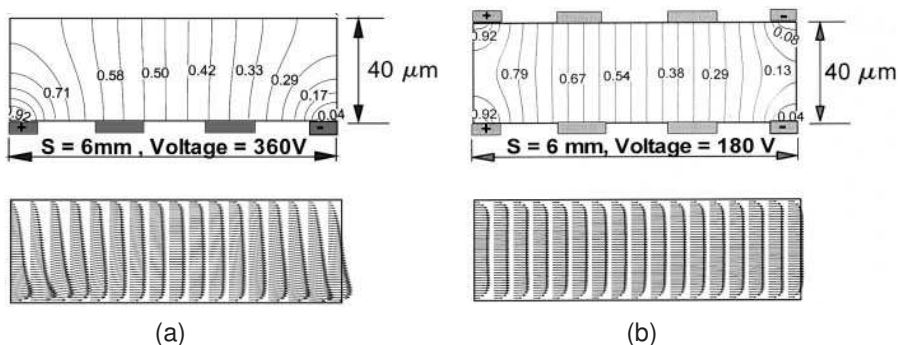


Figure 4.19: Electric potential distribution and flow velocity field in (a) a single-side electrode configuration and in (b) a double-banked electrode configuration (adapted from [72]).

tangential electric field near the channel wall. The shape of the sample plug will be increasingly distorted as it flows through a number of separation segments. However, if the sample plug is always kept far away from the active electrodes, this plug distortion might be avoided. The simulated results in Figure 4.19b show that the double-banked electrodes create a much more symmetric electric potential distribution and thus will result in flat velocity profiles along the whole separation segments. Therefore, the double-banked electrodes will have much less plug distortion and will achieve higher separation quality.

The flow profile in the field region is flat while the flow profile in the field-free region is parabolic. Around the active electrodes, there is a transition area where the flow profile changes from flat to parabolic. Additionally, turbulence might also occur around the electrodes during switching on and off the voltage. Therefore, it is essential to keep the samples far from the active electrodes. The solution is that, instead of applied to the neighbor electrodes, the separation voltage is applied to the electrodes with a gap of one or several electrodes, as shown in Figure 4.1. The voltage is switched in such a way that the sample plug resides always in the EOF regions.

## 4.8 Flow distortion above floating electrodes

It was reported in [73] that the surface charge will be induced when the titanium thin film is brought into contact with the electrolyte. In turn a diffuse layer with counter ions will be formed over a floating electrode, which will move under the influence of a DC field as the mechanism of EOF in the silica channel. From literatures it can be found that the  $\zeta$ -potential of titanium film in electrolyte with counter ion concentration of  $0.001\text{ M}$  is around  $-8\text{ mV}$  at  $\text{pH } 7$ . The  $\zeta$ -potential of

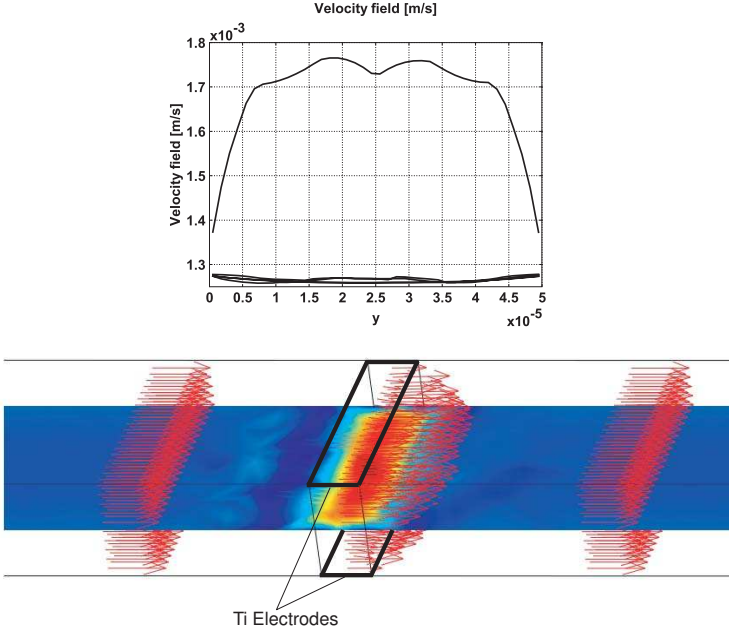


Figure 4.20: Flow distortion above the floating electrodes.

the silica used as the channel material reported in [74] is around -90 mV at pH 7 in electrolyte with the same counter ion concentration of 0.001 M ( $pC = -\log C = 3$ ). The  $\zeta$ -potential of the titanium electrodes is much lower than that of the silica channel wall.

On the other hand, the floating metal electrode short-circuits the voltage drop in the channel, which will render a zero lateral electric field above the electrode surface. Low  $\zeta$ -potential and zero lateral electric field result in almost zero slip velocity above the floating electrodes and thus flow distortion will occur. The numerical modelling was carried out in Comsol Multiphysics. In the model two opposing floating electrodes are placed in the middle of an EOF channel, as shown in Figure 4.20. The simulated flow profiles at different positions of the channel are plotted in the same figure, showing that the largest flow distortion is located above the floating electrodes.

## 4.9 Gas venting

Electrolysis will occur and therefore gases will be formed when a DC voltage is applied on the electrodes immersed in an electrolyte. The formation of the

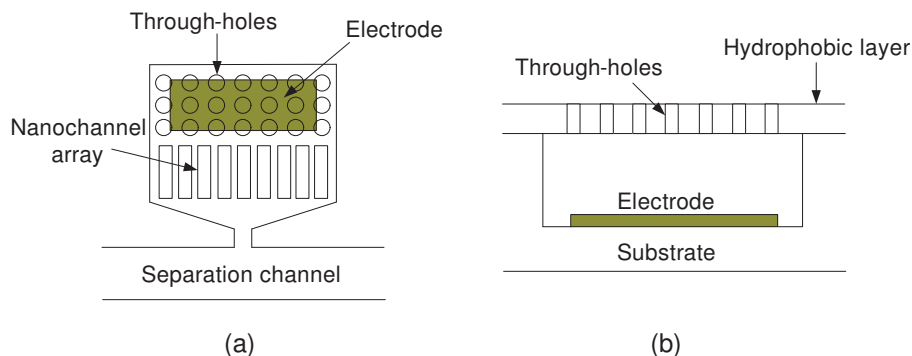


Figure 4.21: (a) Top view and (b) cross-sectional view schematics of the electrode chamber used for gas venting.

gases is because of the chemical reactions taking place at the electrodes. For microchip CE, the chance that the gas bubbles get into the separation channel can be greatly reduced by placing the electrodes close to the reservoirs or by using off-chip electrodes. But, for the moving field CE, electrolysis might cause serious problems since the electrodes are distributed ubiquitously inside the separation channel. Therefore, we would like to propose a chamber structure that connects to the separation channel and houses the electrodes, as shown in Figure 4.21. The electrode is placed at the bottom of the chamber, and the roof of the chamber is made from hydrophobic materials containing a lot of through-holes (or from other gas-permeable but liquid-impermeable materials), which enables gas venting and keeps liquid inside. A nanochannel array is employed to prevent the gas bubbles from entering the separation channel, while it doesn't block the electrical connections of the electrodes.

## 4.10 Moving field CE system

The schematics of the moving field CE system is depicted in Figure 4.22. The high flow-resistance channel arrays are created by subdividing the sample injection channel into multiple parallel channels, which are employed to minimize a flow loss via the sample injection channel during separation. A control unit is present comprising output terminals that are connected to each electrode in the micro-channels and reservoirs. The control unit controls the sample injection by applying suitable voltage to the electrodes in the sample reservoirs. The sample will be driven through and form a sample plug in the separation channel by electroosmosis. Then, the control unit generates voltages at its output terminals so as to control the moving field separation process, meanwhile the voltage on the electroosmotic pump will be arranged to fully compensate the plug dispersion in the



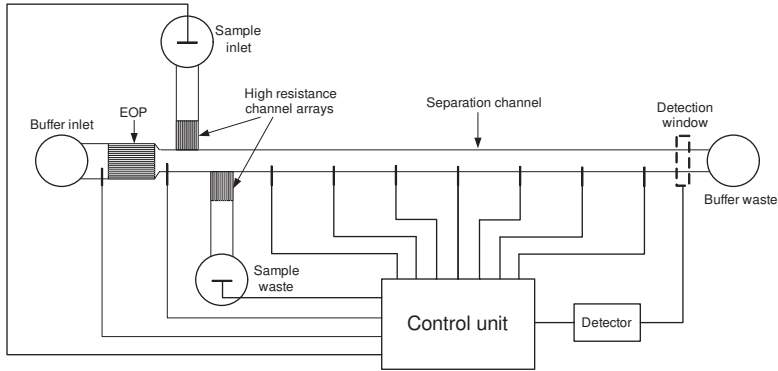


Figure 4.22: Schematics of the moving field CE system.

separation segment. The samples in the side channels will be driven slowly away from the separation channel so that the separation will not be disturbed by the remaining sample. A detector is employed to detect the sample in the detection window at the end of the separation channel. The detector outputs a signal which is the input for the control unit. Before each operation, a measurement can be done to find out the EOF properties of the separation channel. The measurement results will be fed back to control unit in order to fine tune the control of the voltages over the electrodes of the separation channel.



## Chapter 5

# Biomass Concentration Detection

### 5.1 Introduction

In the fermentation process, the carbohydrates are converted by the yeast into alcohol, carbon dioxide and numerous byproducts. Yeasts are unicellular eukaryotic microorganisms that can be found ubiquitously in the environment. Traditionally, there are two types of beer yeast, ale yeast (*Saccharomyces cerevisiae*, as shown in Figure 5.1) and lager yeast (*Saccharomyces uvarum*). The yeast catalyze the desired reactions but are also self-catalyzing, generally referred to as microbial growth. Therefore, the yeast population is an important process indicator.

Measurement of yeast cell concentration is essential for monitoring and control-

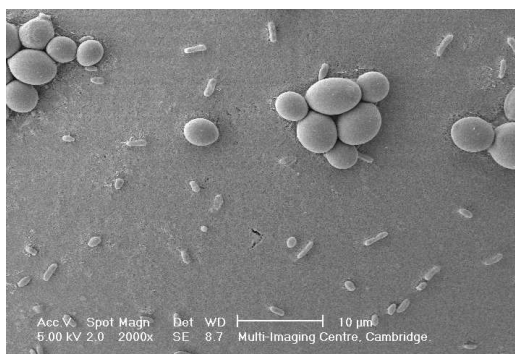


Figure 5.1: *Saccharomyces cerevisiae* yeast cells.

ling the fermentation progress. The traditional method dry weight measurement, which involves sampling, drying and weighting, is accurate but quite labor intensive and time consuming. Inline measurement of the biomass concentration is possible nowadays by optical and electrochemical means. However, miniaturization leads to a decline in their sensitivity and interference from byproducts and air bubbles.

In the previous work [75], an impedance sensor for monitoring yeast cell concentration was proposed. The conductivity change of the cell suspension below and above the characteristic frequency was measured, which depends linearly on the biomass concentration. The impedance of the cell suspension was measured by two planar electrodes, a third electrode was employed to compensate for the changes in the electric properties of the medium. Nevertheless, its ability to detect cells at extremely low concentrations remains limited. Here, in contrast, we present an alternative and complimentary solution to fulfill the biomass concentration detection, we demonstrate an electrokinetic technology for rapidly increasing the concentration of the cells while measuring the concentration. This method can also be used to detect pathogens at extremely low concentration.

## 5.2 Design principle

The proposed design is an open-top planar structure which is composed of one pair of trapping electrodes and a four electrode conductivity detector. The trapping electrode pair is utilized to trap and collect the live cells from the flowing suspension by positive dielectrophoresis. The dead cells with leaky membranes will escape from the trapping since they have already lost the permittivity contrast to the medium. The purpose of trapping is to condense the live cells and keep them at a proper position for the conductivity detection. In order to prevent unwanted electrochemistry, the metal electrodes of the detector are protected by an insulating film. The 4-electrode configuration has already been proved to allow sensitive and accurate sensing in a wide frequency range, which is not the case with a 2-electrode configuration [76]. The device will be packed and mounted into the fermentation chamber. When mounted into the fermentation chamber, the electrode part of the chip will be exposed to the liquid suspension during operation. A sieve-like filter surrounding the chip is necessary to keep the uninterested large particles or the debris away from the trapping electrodes. The yeast cells will be continuously brought close to the trapping region by the stirred flow in the chamber. After each measurement, the live cells could be released by switching off the voltage on the trapping electrodes.

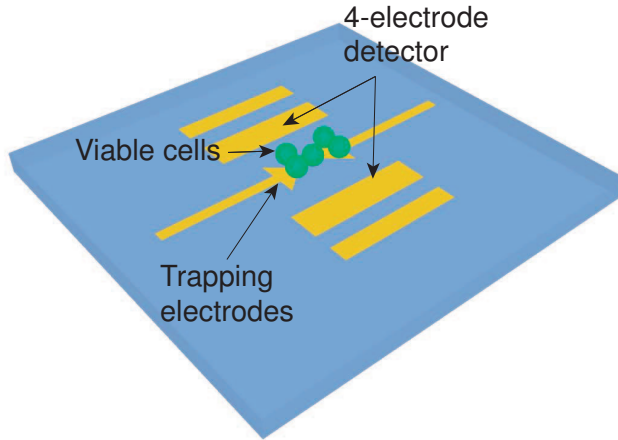


Figure 5.2: Schematic view of the design.

## 5.3 Viable yeast cell trapping

### 5.3.1 Model of the yeast cell

Yeasts are walled, single-cell organisms that usually assume a roughly spherical shape. The yeast cell can be roughly divided into three regions: the wall, the cell membrane, and the cell interior. In yeasts, the cell wall provides mechanical protection to the fragile membrane. The membrane, which consists of a selectively permeable bilayer of lipid proteins molecules, is thin ( $\sim 10^{-2} \mu\text{m}$ ) and quite fragile. It serves a vital function as a two way conduit for (i) life-sustaining nutrients and regulatory substances required by the cell's metabolism and (ii) waste materials excreted from the cell. The cell interior is extraordinarily complex, containing the nucleus and vacuoles as well as numerous other structures, all suspended in an aqueous ionic fluid called the cytoplasm. In biology the yeast cell's complete structure is widely studied, but attention here is only focused on its dielectric properties. Thus, a dielectric model for the cell, taken from [57], is explained below.

The cell wall is usually modeled as a homogeneous spherical concentric shell of finite thickness with bulk permittivity  $\varepsilon_w$  and ohmic conductivity  $\sigma_w$ . The membrane of the cell typically can withstand a DC voltage up to  $\sim 10$  mV without disruption. This breakdown voltage correspond to an effective dielectric strength of  $\sim 10^6$  V/m. The membrane behaves like a very low loss capacitor, blocking low-frequency electric field and electric current from the interior of the cell. Thus,

membranes are typically characterized by effective capacitance  $c_m$  and conductance  $g_m$ , both per unit surface area. Despite the complexity of the cell interior, simplified models can be used in many circumstances. In particular, we use here a homogenous model for the cytoplasm with dielectric permittivity  $\varepsilon_c$  and ohmic conductivity  $\sigma_c$ .

Thus, from the original structure of the yeast cell depicted in Figure 5.3a, a multilayered dielectric model can be derived, as shown in Figure 5.3b. When observed from the outside, the cell can be viewed as a homogeneous sphere with an equivalent permittivity  $\varepsilon'_2$  and an equivalent conductivity  $\sigma'_2$ , as shown in Figure 5.3c. The values of  $\varepsilon'_2$  and  $\sigma'_2$  are both frequency ( $\omega$ ) dependent.  $\varepsilon'_2(\omega) = \text{Re}(\underline{\varepsilon}'_2)$  and  $\sigma'_2(\omega) = -\omega \cdot \text{Im}(\underline{\varepsilon}'_2)$ , where  $\underline{\varepsilon}'_2$  is the complex effective permittivity in the homogeneous sphere model and can be retrieved by the methodology described in [57].

### 5.3.2 Induced dipole strength calculation

As mentioned in a previous chapter, the Clausius-Mossotti factor is dependent on the complex permittivity contrast between the medium and the particle, which is normally symbolized with  $K$  and takes the form

$$K = \frac{\varepsilon_p^* - \varepsilon_m^*}{\varepsilon_p^* + 2\varepsilon_m^*} \quad (5.1)$$

where  $\varepsilon_p^*$  and  $\varepsilon_m^*$  are the complex permittivity of the particle and electrolyte. The direction and the magnitude of the averaged DEP force are determined by the induced dipole strength  $\text{Re}(K)$  in any given electric field distribution.

The induced dipole strength for yeast cells can be calculated as a function of frequency by the homogeneous sphere model. Parameter values for the yeast model are specified in accordance with literature values [57] in Table 5.1. The curves in Figure 5.4 indicate that the induced dipole strength of the yeast cells is strongly dependent on the conductivity of the electrolyte. Increasing electrolyte conductivity decreases  $\text{Re}(K)$ , even reversing its sign at low frequencies from positive to negative. At very high frequencies that is above 100 MHz,  $\text{Re}(K)$  is negative for all electrolyte concentrations.

For the examination of cell radius in Figure 5.5, we set the conductivity of the electrolyte concentration to 0.1 S/m, which is close to the conductivity of the wort during the beer fermentation process. At very low and high frequency, The frequency dependence of  $\text{Re}(K)$  for yeast is not sensitive to the size of the cell. At frequencies between 100 KHz and 10 MHz,  $\text{Re}(K)$  increases as the cell radius increases. At around 10 MHz, the yeast cells will be pDEP with the maximum induced dipole strength.

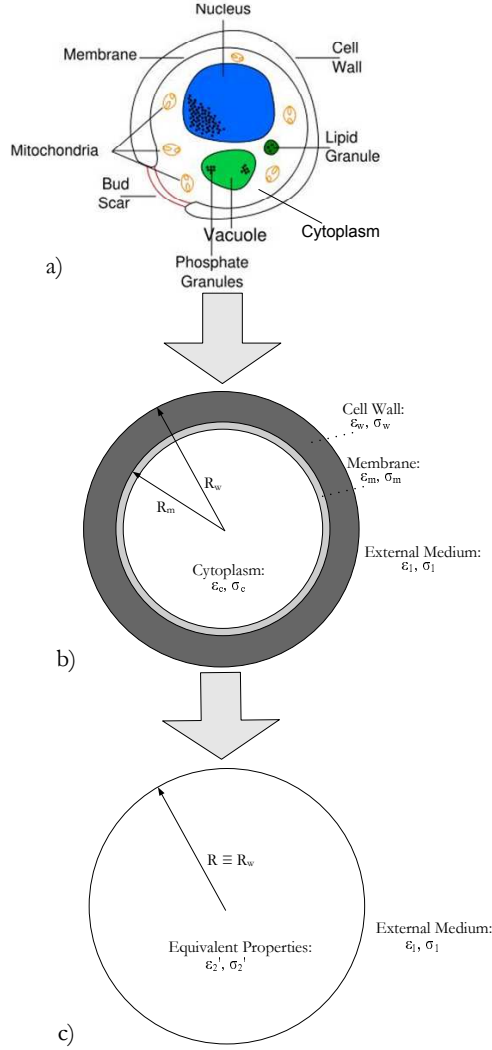
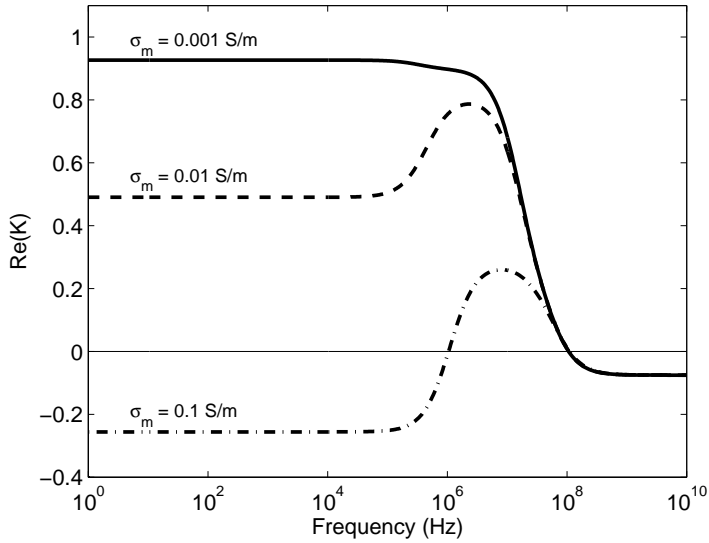


Figure 5.3: Derivation of the equivalent electrical model of a yeast cell. (a) Sketch of a real yeast cell (b) Electrical model of the cell (c) Simplified electrical model of the cell.

Table 5.1: Parameters for the yeast model.

Parameter	Symbol	Value
Cell radius	$R$	$2.5 \mu m$
Cell wall conductivity	$\sigma_w$	$0.1 \text{ S/m}$
Cell wall permittivity	$\varepsilon_w$	$65 \varepsilon_0$
Membrane capacitance	$c_m$	$1 \mu F/cm^2$
Cytoplasm conductivity	$\sigma_c$	$0.5 \text{ S/m}$
Cytoplasm permittivity	$\varepsilon_c$	$60 \varepsilon_0$
Electrolyte conductivity	$\sigma_1$	$0.001\text{-}0.1 \text{ S/m}$
Electrolyte permittivity	$\varepsilon_1$	$78 \varepsilon_0$


 Figure 5.4:  $\text{Re}(K)$  for yeast cell in the medium of different conductivities calculated as a function of frequency.



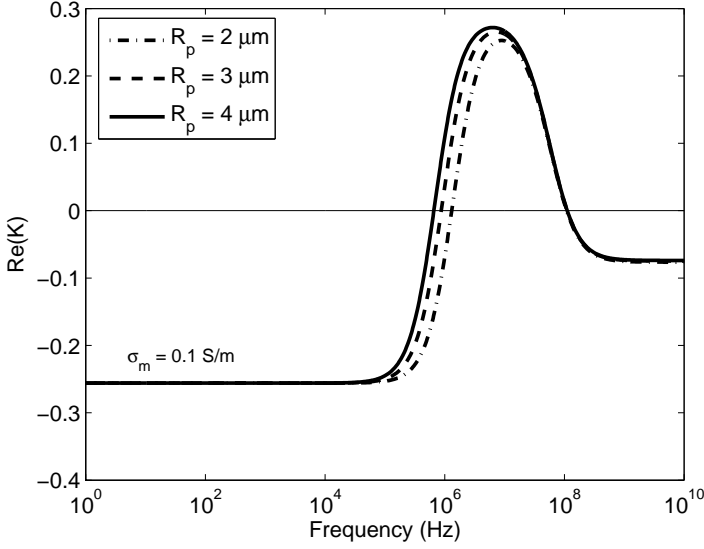


Figure 5.5:  $\text{Re}(K)$  for different size yeast cells calculated as a function of frequency.

### 5.3.3 Dielectrophoretic trapping

The Brownian movement of the particles is irregular and over time the distribution of the random displacement of the particles follows a Gaussian profile with a mean displacement (in one dimension) given by [58]

$$|\bar{x}| = \sqrt{2Dt} \quad (5.2)$$

where  $D$  is the diffusion coefficient. For a spherical particle of radius  $R_p$ , this is given by

$$D = \frac{k_B T}{6\pi\eta R_p} \quad (5.3)$$

where  $k_B$  is the Boltzmann constant. Application of a uniform force will perturb the probability distribution so that the center of the Gaussian profile will move in the direction of the force field. Defining the center of the Gaussian to be  $\bar{x}$ , in the presence of a deterministic force (i.e. composite force of the DEP force and the viscous force), and after a short time ( $\Delta t$ ) there will be a displacement from  $\bar{x}$  to  $\bar{x} + \Delta\bar{x}$ , where

$$\Delta \bar{x} = (\frac{\bar{F}_{DEP}}{6\pi\eta R_p} + V_{liq})\Delta t \quad (5.4)$$

where  $V_{liq}$  is the flow velocity in the vicinity of the particle. The particle has uncertainty in its position given by the Gaussian profile. If the deterministic force produces a displacement which is greater than the uncertainty in the position, namely  $\Delta \bar{x} > 2\sqrt{2Dt}$  corresponding to two standard deviations from the mean position, the particle will have an observable deterministic displacement. Therefore, the threshold DEP force needed to overcome the fluid drag force and the Brownian motion is calculated as

$$F_{DEP,th} = 6\pi\eta R_p V_{liq} + 2k_B T \sqrt{\frac{2}{D\Delta t}} \quad (5.5)$$

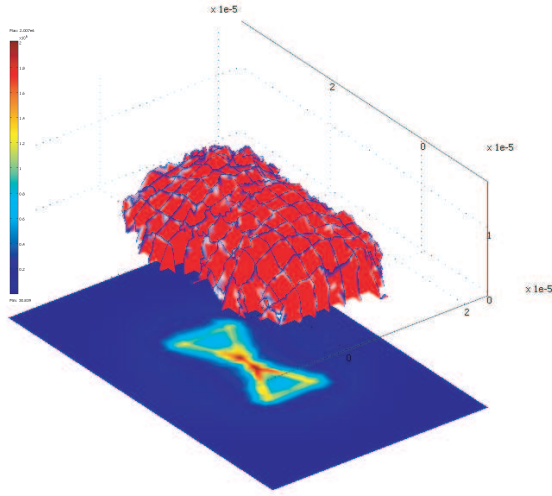
This equation holds for 95 % of all particles, i.e. 2 standard deviation, due to the stochastic nature of their movement. For 2  $\mu\text{m}$  radius yeast cells, the first term (i.e. the viscous force) is about 19 pN, given the flow rate is 500  $\mu\text{m/s}$ . And the second term (i.e. the diffusion force) is 0.0107 pN, which is quite small and negligible if compared to the viscous force. From the spatial distribution of the electric field gradient and a threshold DEP force of 19 pN, the space in which the cells are trapped can be derived. This space is found to resemble a semi-ellipsoid with a volume of about 400  $\mu\text{m}^3$ , as shown in Figure 5.6a. When the flow velocity is decreased to 100  $\mu\text{m/s}$ , this space is found to be enlarged due to the reduced fluid drag, as shown in Figure 5.6b.

In [77], it was demonstrated that the strong electric fields up to  $2 \times 10^6$  V/m did not harm the yeast cells, the cells are observed dividing during many hour exposed to that high electric field.

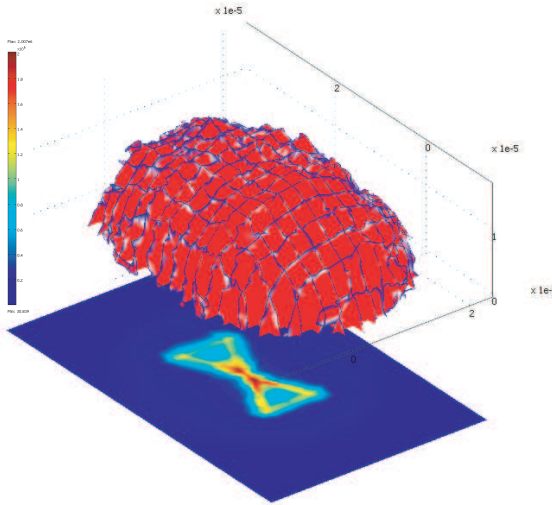
The dielectrophoretic trapping only works on the viable cells. Dead cells with leaky membranes cannot be polarized, therefore they will not be trapped and will not affect the measurement of the biomass concentration.

## 5.4 Contactless 4 electrode detection

In F. Laugere's work [76], a contactless 4 electrode detector was proposed for microfluidic CE application. In order to prevent the electrochemical reaction between the metal electrodes and the electrolyte, the electrodes were protected by a 30 nm SiC film. In contrast with the 2 electrode configuration, the measured conductivity of the 4 electrode configuration does not depend on the insulating film capacitance and thus it could achieve sensitive detection with various carrier-electrolyte conductivity without requiring adjustment of the measurement frequency.



(a)



(b)

Figure 5.6: Simulated results showing how the trapping space is influenced when the flow velocity is decreased from (a)  $500 \mu\text{m/s}$  to (b)  $100 \mu\text{m/s}$ .

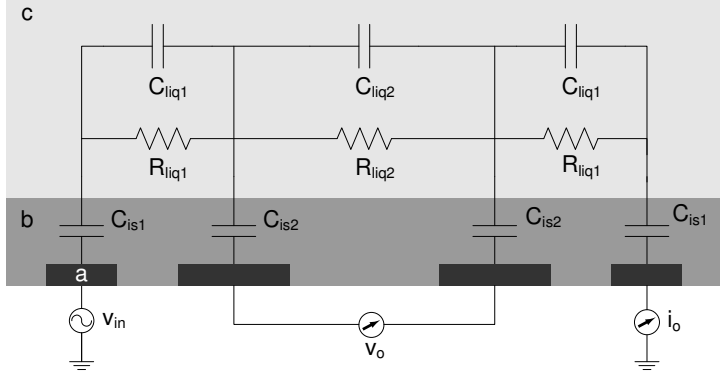


Figure 5.7: Electrical model of the contactless 4-electrode conductivity detector and measurement scheme. (a) metal electrodes, (b) isolation film, and (c) suspension.

### 5.4.1 Electrical model of the detector

The electrical model of the contactless 4-electrode detection cell and the measurement scheme are shown in Figure 5.7.  $C_{is}$ ,  $C_{liq}$  and  $R_{liq}$  are respectively, the capacitance of the insulating film, the capacitance of the liquid and the resistance of the liquid.  $R_{liq2}$  is the resistance that we would like to measure. The input voltage  $v_{in}$  is applied on the two outer electrodes. The voltage difference between the two inner electrodes is measured with a high-input impedance differential amplifier and thus, there is no current through the capacitors  $C_{is2}$ . Therefore, the measured voltage drop is the voltage drop over the resistance  $R_{liq2}$ . The current  $i_o$  flowing through the outer electrodes is measured, which is also the current flowing through the resistor  $R_{liq2}$ . The value of the resistor  $R_{liq2}$  can be retrieved from the ratio  $v_o/i_o$ .

### 5.4.2 Readout circuits

#### Direct current readout

Connecting a current source to the outer electrodes is a way to steer the current. However, it is not applicable to our case since the detector has a rather high input impedance  $Z_{in}$  and most of the current would flow to the parasitic capacitance  $C_{p1}$  (Figure 5.8).

$$Z_{in} = \frac{2}{j\omega C_{is1}} + 2R_{liq1} + R_{liq2} \quad (5.6)$$

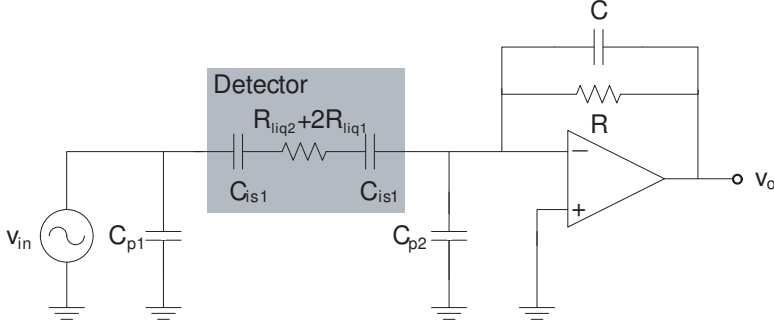


Figure 5.8: Schematics of the direct current readout circuit using a transimpedance amplifier.

The cable that connects the current source to the detector has a distributed capacitor between the conducting wire and the grounded shield. The capacitance is dependent on the length of the cable: a 1 m long cable has a distributed capacitance of about 100 pF. This value is larger than  $C_{is1}/2$  and therefore it introduces a systematic error in the current steering.

A solution is to connect a voltage source of fixed amplitude to one of the outer electrodes and measure the resulting current at the other outer electrode with a transimpedance amplifier, as shown in Figure 5.8. The voltage applied on the outer electrode is not affected by the capacitance of the cable. The current resulting from the applied voltage is measured with a transimpedance amplifier which has a low input impedance. The output voltage of the transimpedance amplifier  $V_o$  is proportional to the current flowing through the detector. The high output impedance of the detector together with the input capacitance of the operational amplifier  $C_{p2}$  might be a source of instabilities for the transimpedance amplifier. Oscillations are prevented by putting a capacitor  $C$  in parallel with the feedback resistor  $R$ .

### Differential voltage measurement

The differential voltage between the two inner electrodes can be measured by a differential amplifier. There are two critical issues for the differential amplifier. First, it must have a very high input impedance so that it does not load the detector. Second, the common-mode rejection ratio (CMRR) should be high enough to reject the high common-mode voltage. The details of designing such a high impedance and high CMRR differential amplifier are discussed in [76]. In that work, a specific bootstrapping technique was introduced to meet the high impedance requirement and to prevent the severe degradation of the common-mode rejection ratio due to component mismatch.

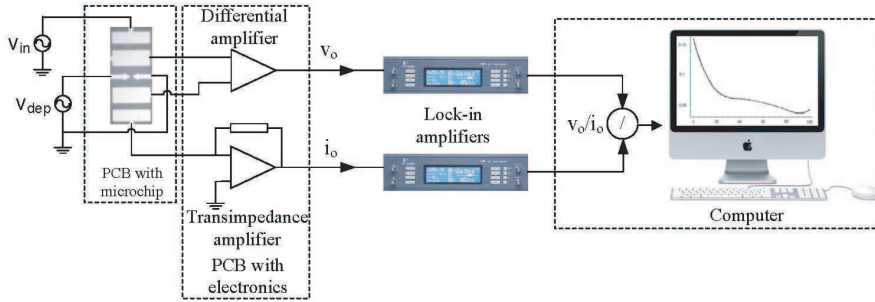


Figure 5.9: Measurement setup for the biomass concentration detection.

### 5.4.3 Measurement setup

Figure 5.9 shows the measurement setup for the biomass concentration detection. A 10 MHz AC voltage is applied over the trapping electrodes and a 1 KHz AC voltage is imposed on one of the outer electrode. The readout electronics on the printed circuit board consists of a differential amplifier and a transimpedance amplifier. The two inner electrodes are connected to the high input impedance differential voltage amplifier. One of the outer electrodes is connected to the transimpedance amplifier. The output of the differential amplifier and that of the transimpedance amplifier are connected to lock-in amplifiers to measure the signal amplitudes. The measured signals are sent to a PC through a data acquisition card, and the conductivity of the aqueous suspension can be retrieved from the real-time division of  $i_o/v_o$  by using the software Labview.

# Chapter 6

## Device Fabrication

### 6.1 Standard processes

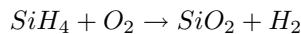
First of all, the standard processes used in the device fabrication will be briefly introduced. These processes were performed in DIMES (Delft Institute of Microelectronics and Submicrontechnology) cleanroom class 100 and MEMS lab.

#### 6.1.1 Layer deposition

##### Plasma enhanced chemical vapor deposition (PECVD)

Chemical vapor deposition (CVD) is a chemical process used to produce thin film in microfabrication. The source gases decompose and react with the substrate surface to form the deposition. The process can be enhanced either by a subatmospheric pressure and a high temperature (LPCVD) or by a plasma (PECVD). Various materials can be deposited by CVD process such as silicon, silicon oxide, silicon carbide, silicon nitride, metals, etc.

To deposit the oxide layer, we choose PECVD process although thermal growth gives better oxide quality. That is because PECVD allows deposition at lower temperature (300-400 °C) and thus can be conducted after metallization. The common source gas used for PECVD oxide deposition is silane ( $SiH_4$ ). And the reaction is described as below:



##### Sputtering metallization

Sputtering is another process used to deposit a thin film on substrates. A gaseous plasma is first created by applying a very high voltage across a low-pressure gas.

The ever-present electrons are accelerated by the DC electric field and collide with neutral gas atoms in their path. The collision will drive the outer shell electrons off the gas atoms and make them become positively charged ions. These ions strike a target composed of the desired coating material under the influence of the DC electric field, and cause the atoms from the target to be ejected and come into contact with the substrate facing to the target. Sputtering was usually used by us to deposit metals like aluminum, titanium, and etc.

### 6.1.2 Plasma etching

In a plasma etching process, the surface of the film to be etched is subjected to both physical and chemical attacks from the plasma environment. The physical attack is by far the largest and is conducted by the ions. The chemical attack is commonly done by free radicals, which also depends on the flux of free electrons. Plasma etching has several significant advantages when compared with wet etching. Plasma etching is more repeatable than wet etching. Most important for small features, plasma etching allows directional etching which minimize under-etching and etch bias. Plasma environment may also have much fewer particles than aqueous medium. Finally, a plasma etching process produces less chemical waste than wet etching. Therefore, it was chosen by us for etching oxide and titanium layers.

Deep reactive ion etching (DRIE) is a highly anisotropic etching process which is widely used to create high aspect ratio holes or trenches. There are two types of deep reactive ion etching (DRIE) processes: the cryogenic process and the Bosch process. In the cryogenic process, the chemical reaction that produces isotropic etching is slowed down by the extremely low temperature which limits the application of the cryogenic process. In the Bosch process, however, the isotropic etching is prevented by alternating repeatedly the etching and the passivation steps. Therefore, the Bosch process makes it possible to do wafer dry etching nearly at room temperature. It was used by us to form the access holes in silicon wafers.

### 6.1.3 Photolithography

Photolithography is a very important process and was conducted repeatedly throughout the whole fabrication procedure. The purpose of the photolithography process is to transfer the pattern on the mask to the photoresist on the substrate. The process is mainly consisting of four steps: surface pretreatment, resist coating, exposure and development.

#### Surface pretreatment

After cleaning the wafer, a layer of liquid or gaseous adhesion promoter, such as HMDS, is created on the wafer surface to promote adhesion of the photoresist to



the wafer. In case of applying SU-8 to the glass wafer, it is better to treat the wafer with low power oxygen plasma beforehand.

### **Resist coating**

The photoresist is normally coated to the wafer by spin coating. The resist viscosity and the spinning speed are two key parameters that determine the resulting thickness of the resist. Other techniques, such as spray coating and electro-deposition [78], can also be used to coat the resist. After resist coating, soft bake is necessary to evaporate the solvent from the photoresist completely.

### **Exposure**

Patterns on the mask can be transferred to the resist by a wafer stepper or by a contact aligner. The wafer stepper is a projection printing system which is widely used for high-volume manufacturing today. What we used the most for our application is the contact aligner which could perform contact printing and proximity printing. Compared with contact printing, proximity printing offers lower resolution of the printed patterns due to diffraction effects. Nevertheless, proximity printing is sometimes used when the resist layer to be exposed is vulnerable or sticky.

### **Development**

The patterns transferred to the photoresist are revealed during the development process. In this process selective removal of the photoresist takes place in a resist dependent solution. A PEB (post-exposure bake) is performed before development to help reduce standing wave phenomena caused by the destructive and constructive interference patterns of the incident light. And a hard bake is performed after development to solidify the remaining photoresist.

## **6.2 Materials used**

### **6.2.1 Glass wafer**

Fused quartz and fused silica are types of glass containing primarily silica, which is  $SiO_2$  in an amorphous (non-crystalline) form. They are allowed for processing in the cleanroom for they do not contain metals. However, they are very fragile. Borosilicate glass, another type of glass, which contains Boron is characterized by its resistance to heat, chemicals and specific coefficients of thermal expansion. The exact composition of each of these glasses differentiates them from one another and determines their best application. Schott AF 45 and Corning Eagle 2000 are two types of Borosilicate glass that we used.

Schott AF 45 with the thickness of  $400\ \mu m$  is a modified borosilicate glass with a high content of BaO and  $Al_2O_3$ . The main characteristics of this glass type are:

alkali free in synthesis, low coefficient of thermal expansion, high chemical resistance, excellent thermal resistance, high luminous transmittance and an excellent surface quality.

Corning Eagle 2000 with the thickness  $700\ \mu\text{m}$  is an alkaline earth aluminoborosilicate type of glass. It is a high quality and flat type of glass that was specifically developed for LCD production. Eagle2000 has a very-low glass density, which makes it a lightweight glass, a high chemical durability, advanced thermal properties and near zero alkali content.

### 6.2.2 Titanium

Ti has been reported to be very bio-compatible and chemical inert. Compared to Pt, Ti has a lower polarization resistance for the same surface area if the electrode is in contact with the electrolyte. The initial interfacial capacitance of the Ti may be high, however, a thin passive oxide film forming spontaneously on Ti results in a decreased capacitance with time. When coated with TiN or platinized, the Ti electrode will exhibit a much higher interfacial capacitance and much lower polarization resistance due to the considerable increase in the surface area.

### 6.2.3 Silicon dioxide

Silicon dioxide ( $\text{SiO}_2$ ) is chosen as the insulating material for the titanium electrodes because of the following reasons.  $\text{SiO}_2$  can be easily formed by PECVD process with a controllable deposition rate.  $\text{SiO}_2$  can be etched with high selectivity to titanium and resist mask using plasma etching process.  $\text{SiO}_2$  has very good and stable electrical properties, with a dielectric constant of 4 and a dielectric strength of  $1000\ \text{KV/mm}$ .

### 6.2.4 Dry film resist

Dry film resists (DFR) were originally developed for printed circuit board (PCB) fabrication. Although application for micro-electromechanical systems (MEMS) fabrication is not very common, DFRs have been reported useful for fabricating electroplating moulds [79], sealing of fluidic channels [80] and acting as a mask for powder blasting of microchannels [81]. DFRs have many advantages over the liquid resists, such as easy multilayer formation, excellent adhesion to any substrate, uniform resist distribution, no necessity of liquid handling, low cost and short processing time. In this section, two types of DFRs will be introduced, they are TMMF S2000 and Ordyl SY300.

#### TMMF S2000 series

Table 6.1: Physical properties of the TMMF resist.

Tg	230 °C
Coefficient of thermal expansion	65 ppm/°C
Elongation at break	4.4 %
Breaking strength	60.3 MPa
Young modulus	2.1 GPa
Water absorption	1.8 %
Dielectric constant	3.8
Transparency	400-600 nm

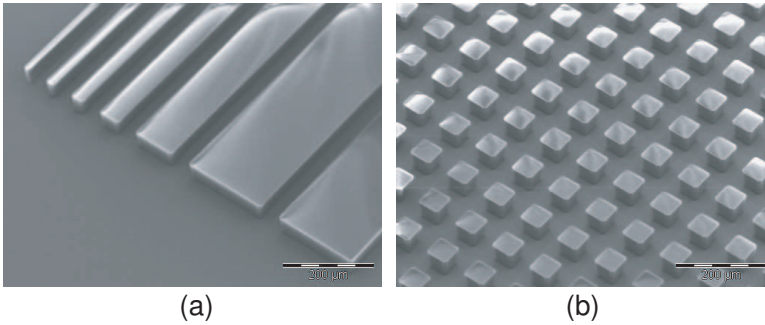


Figure 6.1: SEM photographs of resist structures on a silicon substrate. (a) Strips with feature size range from 10  $\mu\text{m}$  to 200  $\mu\text{m}$  separated by 50  $\mu\text{m}$  gaps. (b) 50  $\mu\text{m}$  square pillars.

TMMF is a type of permanent dry resist composed of 5% antimony compound and 95% novolak type epoxy resin. It is a negative-tone photopolymer designed to be applied with hot roll lamination. The officially revealed physical properties of TMMF are listed in Table 6.1. TMMF S2030 offers the thickness of 30  $\mu\text{m}$  after processing. By multi lamination, a hundreds micron thick layer can be obtained. TMMF has strong adhesion to different materials like glass, silicon, polymers, etc. Excellent resistance to chemicals also allows its use in various biochemical applications.

A number of resolution test experiments were carried out to find out the achievable aspect ratio of the TMMF resist. The minimum features that were demonstrated reproducibly for freestanding structures are 10  $\mu\text{m}$  for a resist thickness of 30  $\mu\text{m}$  exhibiting an aspect ratio of 3. The minimum gap dimensions for the same thickness are 5  $\mu\text{m}$  exhibiting an aspect ratio of 6. The scanning electron microscopy (SEM) photographs shown in Figure 6.1 exhibit some structures formed by the TMMF resist.

The SEM photograph in Figure 6.2 is showing the cross-sectional view of the

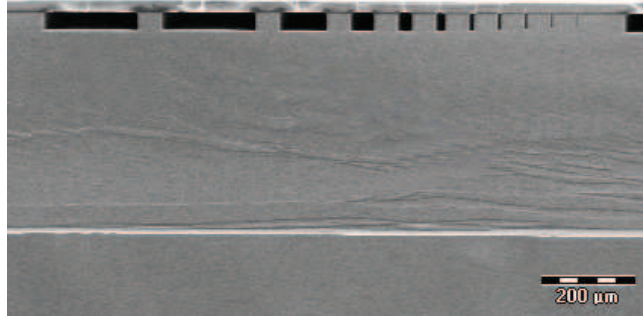


Figure 6.2: SEM photographs of channel cross sections showing the rigidity of TMMF resist.

channels formed by the lamination of the TMMF S2030 resist on parallel trenches whose width range from  $5\text{ }\mu\text{m}$  to  $200\text{ }\mu\text{m}$ , from which we could see the rigidity and the flatness of the resist.

#### Ordyl SY300 series

Ordyl is a solvent type permanent dry film mainly consisting of acrylic ester, acrylic polymer and cross-linking Agent. Like TMMF, it is a negative-tone photopolymer which can be applied by hot roll lamination. It was reported in the work [82] that the maximum aspect ratio of the freestanding structure is 2.7 and that of the gap dimension is 1.3. It was also reported in the same work that this type of dry resist could be used for double bonding process.

### 6.2.5 SU-8

SU-8 is an epoxy-based negative photoresist patented by IBM in 1989 (US 1989). The main component of it is the EPON SU-8, a highly functionalized molecule with 8 epoxy groups. The polymerization is done by a cationic photopolymerization mechanism. Due to the following excellent physical properties, SU-8 has been widely used as a structural material for microfluidic applications in the last decade [83–86].

- High aspect ratio (up to 20)
- Excellent chemical resistance
- Good adhesion to various materials
- Good biocompatibility

- Good thermal stability (no reflow below 220 °C)

## 6.3 Rapid prototyping of the moving field CE device

In the past few years, there is an explosive growth in the development of microfluidic devices for various biochemical applications. The majority of microfluidic prototypes nowadays are fabricated in Polydimethylsiloxane (PDMS) molding [87–89], since it has the advantages of low cost and fast fabrication of complicated structures. Because of its elastic property, however, PDMS cannot be used for fabricating the moving field CE device which contains the high-aspect-ratio slender channels. The microfluidic channels can also be fabricated by sandwiching a patterned photoresist layer in between two substrates [90]. But the required adhesive will readily fill in the slender channels during the bonding process. Glass wet etching is also a commonly used fabrication technique [91], but it is not possible to achieve high aspect ratio structures with this technique. Deep reactive ion etching of glass or silicon can be a promising approach for it permits the fabrication of high-aspect-ratio structures [92, 93]. The sealing of the channel can be done by the thermal bonding [94] or anodic bonding [95]. Nevertheless, we would like to propose a fabrication technique here which is much more suitable for the rapid prototyping of the moving field CE device, owing to its low setting up cost, low processing complexity and short processing time. In this technique, TMMF dry film resist (TOK, Japan) was mainly used. In the progress of channel and access hole formation, only a simple lamination method and a standard photolithography process were conducted. And there was no bonding process required. The fabricated chip was mounted to the holder for a hydraulic test. No cracks were observed in the resist for average pressures up to 1.5 Bar. The 3D schematic view of the device structure is shown in Figure 6.3. The device consists of three layers: a processed glass substrate and two layers of dry film resist. The first resist layer is used to define the channel structure and the second acts as the lid of the channel.

### 6.3.1 Process flow

An overview of the entire process flow is shown in Figure 6.4. The titanium electrodes are firstly formed on the glass substrate (a). The dry film resist is laminated (b) and patterned to form the sidewall of the channel (c). The second resist layer is laminated to seal the channel (c). Finally, the access holes are formed by photolithography process (d). The detailed process flow of dry film resist will be explained as below.

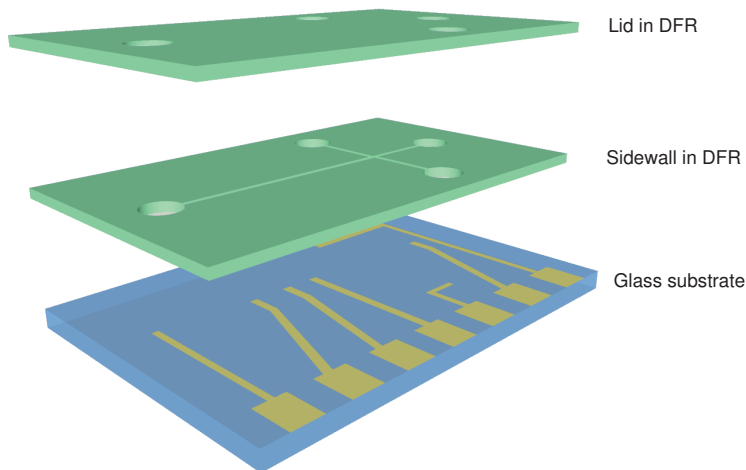


Figure 6.3: 3D view showing the structure of the moving field CE device.

The negative dry film resists, TMMF S2030 ( $30\text{ }\mu\text{m}$  thick, TOK, Japan) was used. The resist layer is protected by two polyester (PET) layers, one on each side. To obtain the maximum process reliability, the substrate should be clean and dry prior to applying the DFR. The glass substrate is firstly baked at  $200^\circ\text{C}$  for 10 minutes on a hotplate to dehydrate the surface. An oxygen plasma treatment is preferred to improve the adhesion. Then, one of the PET layers is peeled off and the resist is laminated onto the substrate manually with a rubber roller at  $85^\circ\text{C}$ , and the laminating pressure and speed is around  $0.5\text{ MPa}$  and  $1\text{ m/min}$ . The other polyester (PET) layer is peeled off after the substrate is cooled down. 5 minutes pre-bake at  $90^\circ\text{C}$  is performed to evaporate the solvent in the resist completely. An anti-reflective foil is laminated onto the backside of the glass to avoid the light scattering from the metal chuck during the exposure. The resist is flush exposed to  $300\text{ mJ/cm}^2$  I-Line with a mask aligner (Karl Suss MA6). The soft contact mode is used with a chromium mask for the exposure. The substrate is subjected to a post exposure bake (PEB) at  $90^\circ\text{C}$  for 5 minutes. The resist is developed for 6 minutes in PGMEA (Propylene Glycol Methyl Ether Acetate) after PEB. The second resist layer of TMMF S2030 is applied to seal the channel and form the access holes to the channels. A lower temperature  $40^\circ\text{C}$  is preferred here to avoid roof collapse. After the lamination step, the protective PET should remain on top. The exposure and PEB is done in the same way as described above. The PET is peeled off right before the development step. The final step is curing at  $200^\circ\text{C}$  for 1 h in a nitrogen oven.

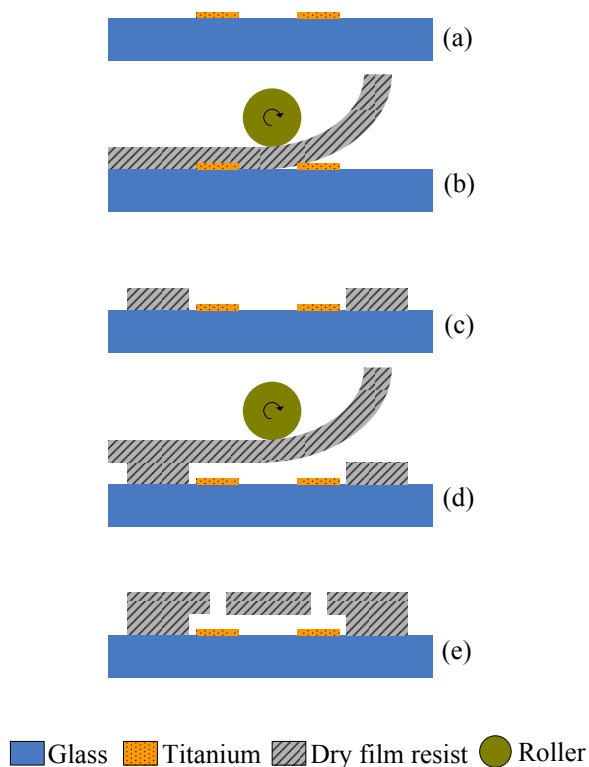


Figure 6.4: Overview of the process flow for rapid prototyping of the moving field CE device.

### 6.3.2 Critical processing steps

#### Oxygen plasma removal of the resist

The oxygen plasma removal of the photoresist after etching the titanium layer on the glass wafer is a critical step. During the operation, the substrate will be heated to a very high temperature. Due to the mismatch in the thermal expansion coefficient, delamination of the metal layer will occur. Therefore, a non-standard recipe with lower energy and longer time was used with extra cooling steps in between.

#### Dry film resist lamination

The dry resist lamination is also a critical step because the air bubbles are prone to be trapped under the resist layer if it is not processed in a proper way. First, the substrate should be heated up to a particular temperature before lamination (i.e. 85°C for the first layer lamination and 40°C for the second layer lamination). Second, a large roller is preferably to be used, since it increases the contact areas with the resist during lamination. Last, the resist must be leaned against the roller during lamination and the pressure and the speed of lamination have to be well controlled according to the data mentioned above. It will be the best if the substrates can be put through a hot-roll laminator after the manual application of the resist.

### 6.3.3 Fabrication results

The fabricated device has a dimension of 1.5 cm  $\times$  3 cm, as shown in Figure 6.5. The main separation channel is 50  $\mu\text{m}$  wide and 18 mm long whose cross-section is shown in Figure 6.6. The length of the pump channel is 1/10 of the main channel. The width of the subchannels in the pump region, as depicted in the inlay of Figure 6.5, is 5  $\mu\text{m}$ . The electrodes are distributed uniformly in the channel, and the span of every two adjacent electrodes is 1.8 mm. These electrodes are connected to the electrode contacts on one side of the microchip.

### 6.3.4 Hydraulic pressure test

The hydraulic pressure test was performed in order to verify the mechanical strength of the TMMF dry film resists. The fabricated chip was mounted to a customized holder. The outlet on the chip was sealed by an adhesive foil while the inlet was connected to the holder via an o-ring. A pressure meter was connected in series with the syringe and the holder, as shown in Figure 6.7. Liquid was pumped into the microfluidic channel continuously by pushing the syringe, meantime, the value on the pressure meter was read. As a result, no cracks occurred to the 30  $\mu\text{m}$  top resist layer for an average pressure up to 1.5 Bar.



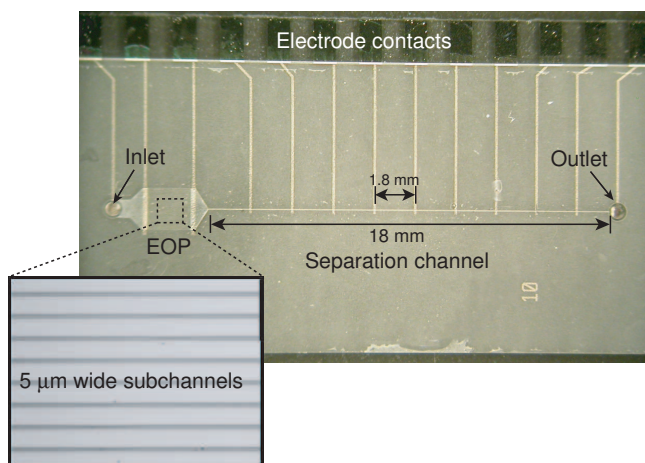


Figure 6.5: Photograph of the fabricated moving field CE device.

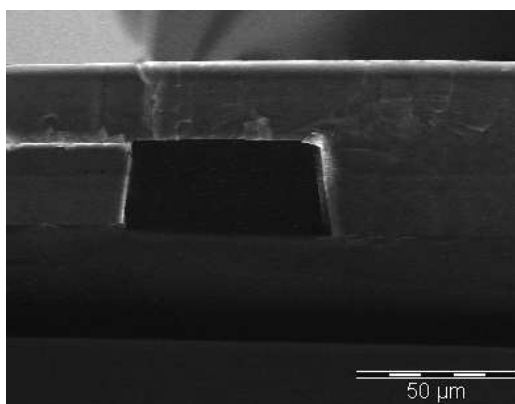


Figure 6.6: SEM photograph of the channel cross section ( $50\ \mu\text{m} \times 30\ \mu\text{m}$  channel sealed by a  $30\ \mu\text{m}$  TMMF resist film).

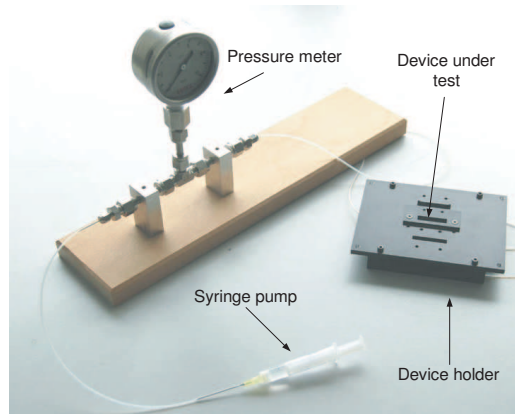


Figure 6.7: Photograph of the hydraulic test setup.

## 6.4 Fabrication of the DEP device

To have top-and-bottom electrodes in the channel, the DEP device was fabricated by the bonding of two processed substrates with an SU-8 layer sandwiched in between, as shown in Figure 6.8.

### 6.4.1 Process flow

On silicon wafer

- (a) 2  $\mu\text{m}$  PECVD oxide deposition
- (b) Sputtering and plasma etching of 200 nm Ti electrodes
- (c) 200 nm PECVD oxide deposition to cover the electrodes
- (d) Plasma etching of the oxide to expose the electrode contacts and the DC electrodes in the channels
- (e) Deposition of 6  $\mu\text{m}$  oxide on the backside and window etching
- (f) Deep reactive ion etching of the access holes

On glass wafer

- (g) Sputtering and plasma etching of 200 nm Ti electrodes
- (h) 200 nm PECVD oxide deposition to cover the electrodes
- (i) Plasma etching of the oxide
- (j) Applying of 20  $\mu\text{m}$  SU-8 to define the channel structures

Wafer bonding

- (k) Adhesive bonding with SU-8 glue

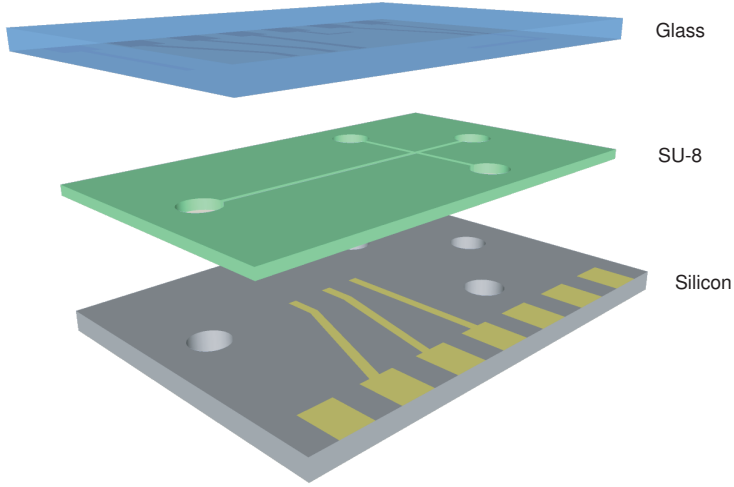


Figure 6.8: 3D schematic structure of the DEP device.

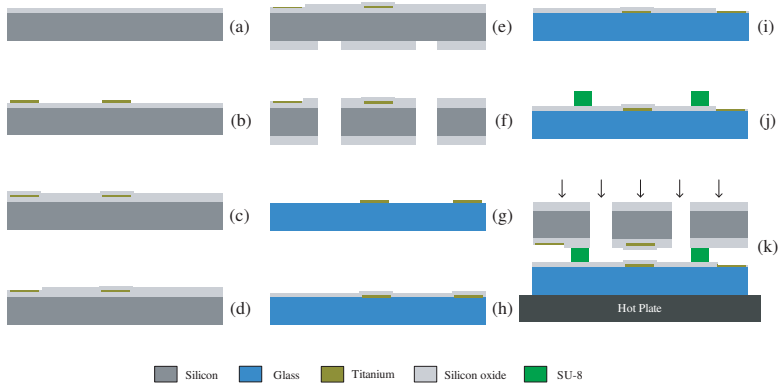


Figure 6.9: Process flowchart for fabricating the DEP devices with isolated electrodes on both top and bottom side of the channels.

Table 6.2: Process parameters for the 2-step etching process.

Step	Gas	Pressure	RF power	Time
Etching	$\text{CF}_4:\text{SF}_6:\text{O}_2=70:10:10$	0.05 mBar	60 W	5 s
Overetching/Landing	$\text{CF}_4:\text{SF}_6:\text{O}_2=70:10:10$	0.05 mBar	50 W	1 s

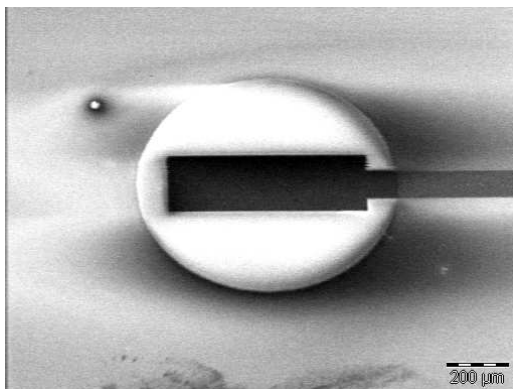


Figure 6.10: Exposed DC electrode with an oxide window etched by the 2-step etching process.

## 6.4.2 Critical processing steps

### Metal sputtering

Normally, deposition of metal layers on glass substrates is preferably to be conducted at room temperature in order to reduce the surface stress. It seems, however, not applicable to our case, since it was found that the titanium sputtered at room temperature was delaminated seriously during the following PECVD process performed at  $400^\circ\text{C}$ . When the sputtering temperature was changed to  $350^\circ\text{C}$ , the delamination did not occur any more.

### Oxide etching

The titanium electrodes can easily be destroyed by the plasma etcher after the above oxide is etched away. Therefore, a 2-step etching method was used. In the 1st step, a sufficient RF power was applied to achieve an etch rate of  $39\text{ }\mu\text{m}/\text{min}$ . In the 2nd step, i.e. the over-etching phase, soft-landing was performed by reducing 20% RF energy. The parameters for the entire etching process are depicted in Table 6.2. Conductivity measurement was conducted to check the remaining oxide on the exposed DC electrodes (Figure 6.10). The measurement result shows that the oxide on the DC electrodes are completely etched away.

### SU-8 processing

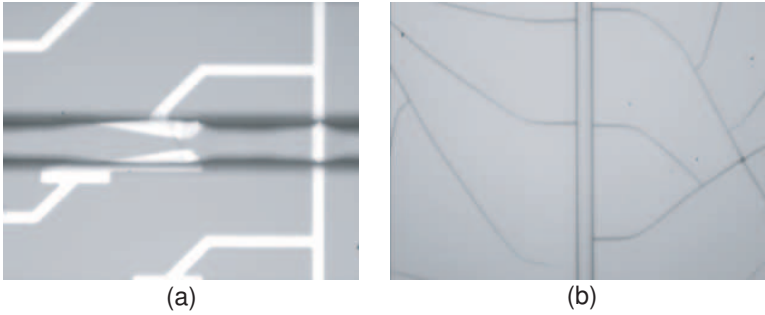


Figure 6.11: (a) SU-8 residues caused by light reflection. (b) Cracks in the SU-8 structures caused by thermal shocks.

For the exposure of SU-8 on glass substrates, an anti-reflective foil must be placed under the substrates to prevent unwanted exposure effects due to the light reflection from the metal chuck. If the anti-reflective foil is not used, there will be plenty of SU-8 residues at the bottom edge of the channel after development, as shown in Figure 6.11a. The regions above the electrodes are almost residue free, because the electrodes were blocking the reflected light during exposure. Another important issue which must be paid attention to when processing SU-8 is preventing thermal shocks, since SU-8 is very sensitive to an abrupt temperature change. A thermal shock introduces considerable internal stress into the SU-8 and in turn breaks the structures, as shown in Figure 6.11b. Therefore, a low temperature ramping speed ( $1\text{-}2^{\circ}\text{C}/\text{min}$ ) should be applied for both ramping up and down in the step of post exposure bake. And the wafer should not be removed off from the hotplate until it is completely cooled down to room temperature.

### Wafer bonding

Wafer-to-wafer bonding is one of the most critical steps in the process flow. First of all, the channel sidewall has to be defined narrow in order to reduce the amount of the glue that can be squeezed into the channel during bonding. The detailed procedure of the wafer bonding is described as below.

#### Wafer pre-treatment

The SU8 glue will not have good adhesion to the PECVD oxide if the surface is not treated carefully. Therefore the silicon wafer should be cleaned with nitric acid followed by 30 minute oxygen plasma treatment at 500 watt.

#### Glue dipping

A  $9\text{ }\mu\text{m}$  SU-8 layer was spun on a dummy wafer. The glass substrate with channel structures was stamped to the dummy wafer on a hotplate at the temperature of  $90^{\circ}\text{C}$ . The glass wafer was pressed against the dummy wafer carefully. The detachment between wafers was performed at  $120^{\circ}\text{C}$  using a blade. Heating the

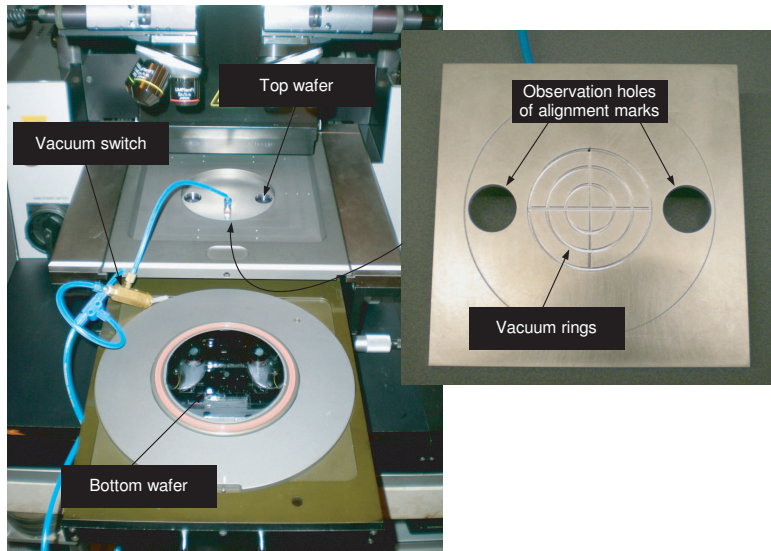


Figure 6.12: Alignment setups for wafer to wafer bonding.

SU-8 to this temperature for a while will decrease the viscosity and will help to separate the wafers.

#### Wafer to wafer alignment

An aluminum dummy mask was customized for the contact aligner to hold the top glass wafer during alignment (Figure 6.12). The 2 cm diameter holes on two sides are made for observation of the alignment marks. The bottom silicon wafer was held on the wafer chuck of the contact aligner. To prevent the vacuum leakage through the access holes, a blue foil was laminated to the backside of the silicon wafer.

#### Pre-bonding

To prevent the wafer shift, the wafers are taken off from the contact aligner together with the wafer chuck. The chuck was put onto the hotplate and heated up to 120°C for 5 minutes. In this step, the glue will melt and forms a pre-bonding between the wafers. Then, the chuck was moved to the heat sink and cooled down to room temperature.

#### Bonding with pressure and heat

The wafers were transferred to a cold hotplate. A weight of 20 kg was applied to the wafers with a thermal isolation layer placed in between. The hotplate was switched on and the temperature was kept at 150°C for 30 minutes. The wafers were not removed until the hotplate was switched off and cooled down to room temperature.

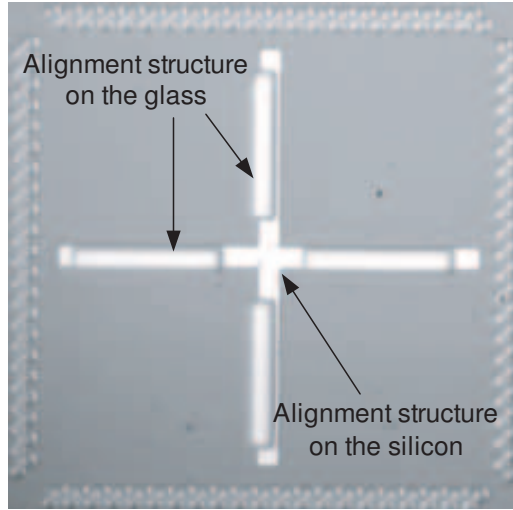


Figure 6.13: Microscopic image of the alignment structures.

#### Crosslinking the SU-8 glue

Flood exposure was performed to cross-link the SU-8 and the post exposure bake was done for the stress removal. The bonded wafers are exhibited in Figure 6.14.

#### Wafer dicing

To mount the device onto the double clamping holder with conductive rubber connecting to it, the electrode contacts on the glass and the silicon have to be opened. Therefore the dicing lines in the glass and the silicon are not in the same vertical plane but have a horizontal distance corresponding to the contact width as illustrated in 6.15. Moreover, the dicing saw has to be stopped before reaching the counter plate when it is dicing one of the plates. Otherwise, the metal wires on the counter plate will be cut off, destroying the electrical connection. Taking into account the thickness of the blue foil stuck to the backside of the wafers, which is  $80\text{ }\mu\text{m}$ , the saw blade has to stop at  $700\text{ }\mu\text{m}$  above the wafer stage when dicing the glass. However, the saw blade has to stop at  $600\text{ }\mu\text{m}$  above the wafer stage when dicing the silicon, since the AF45 glass wafer we used is around  $100\text{ }\mu\text{m}$  thinner than the silicon wafer.

### 6.4.3 Fabrication results

The fabricated DEP device with the dimension of  $1.5\text{ cm} \times 3\text{ cm}$  is shown in Figure 6.16. The zoom-in picture shows a part of the separation channel which has a width of  $50\text{ }\mu\text{m}$  and a depth of  $20\text{ }\mu\text{m}$ , and it also shows the electrodes on two sides of the curves and the trapezoid-shaped top-and-bottom electrodes

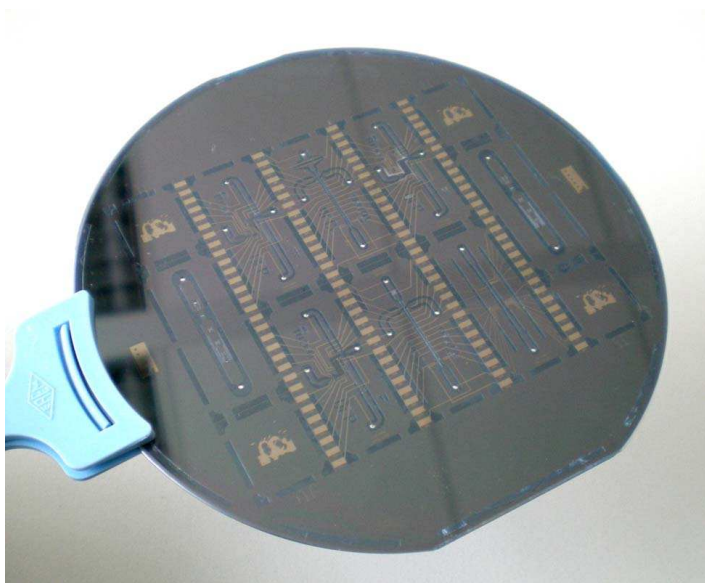


Figure 6.14: Photograph of the bonded wafers.

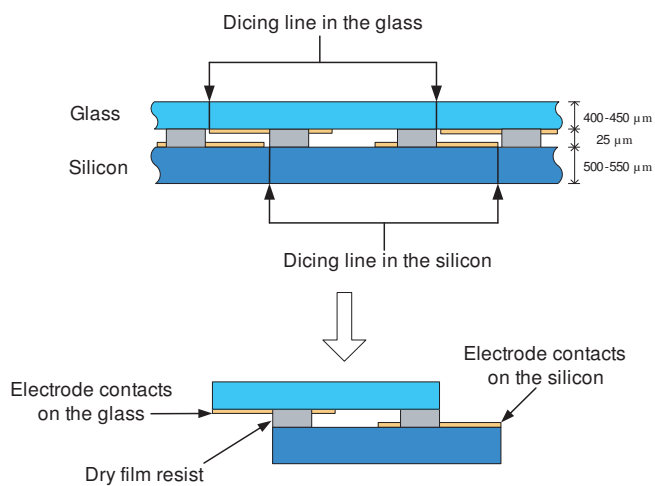


Figure 6.15: Schematic view showing how the bonded wafers are diced.



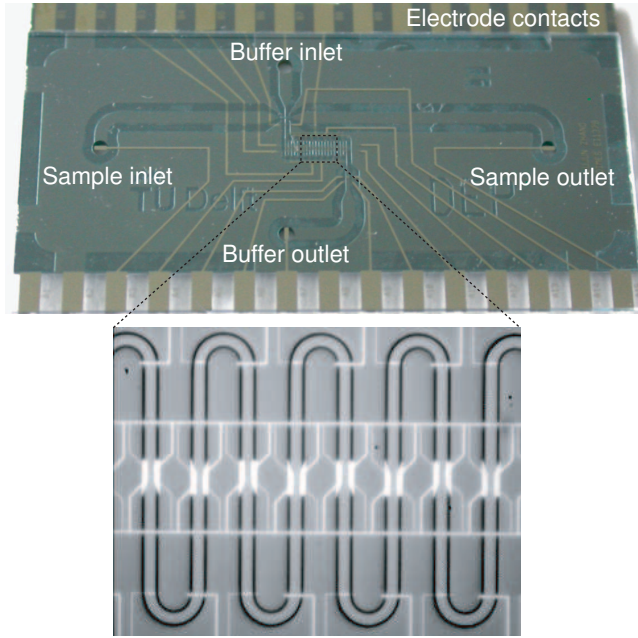


Figure 6.16: Photograph of the fabricated DEP device.

in the straight segments. The channels formed by SU-8 are found to have nearly vertical sidewalls. Owing to the above-mentioned alignment method, the top and bottom electrodes are aligned with an accuracy of  $5\ \mu\text{m}$ . The tight bonding was verified by feeding the Rhodamine B solution into the channels using a syringe pump.



# Chapter 7

## Experimental Results

### 7.1 Device holder

The front and rear views of the holder are shown in Figure 7.1. The microfluidic chip is clamped in the center recess by the fixing plate, with the access holes facing down to the liquid interface on the bottom plate. The o-rings are placed in between to achieve tight sealing. The fluid connection is realized by connecting the plastic tubes to the back side of the holder. And the electrical connection is realized by a double clamping system, the schematic sectional view of which is shown in Figure 7.2. The microfluidic chip is connected to the PCBs via rubber connectors in which the conductive and non-conductive strips are alternatively stacked. The double clamping system makes it possible to connect both the top and the bottom layer of the microfluidic chip. Meanwhile, it also gives user the freedom to connect either the top or the bottom layer of the chip.

### 7.2 Experiments on the DEP device

#### 7.2.1 Measurement setups

The fluorescent polystyrene (PS) beads used in the experiments are carboxylated-modified FluoSpheres from Molecular Probes (USA). The beads' excitation and emission wavelengths are 580 nm and 630 nm, respectively.

The holder containing the microfluidic chip was mounted onto the table of an inverted microscope (IX71, Olympus) equipped with a low noise self-cooling CCD camera (ColorView II, Olympus). The images or the videos were acquired by an imaging software (analySIS docu, Olympus) for further data process and analysis. To see the fluorescent image, an excitation filter ( $\lambda=570\text{-}590\text{ nm}$ ) can be used in

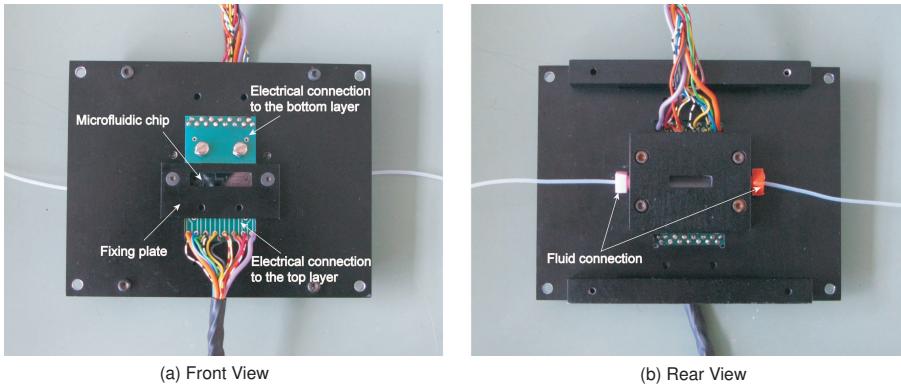


Figure 7.1: (a) Front view and (b) rear view of the device holder.

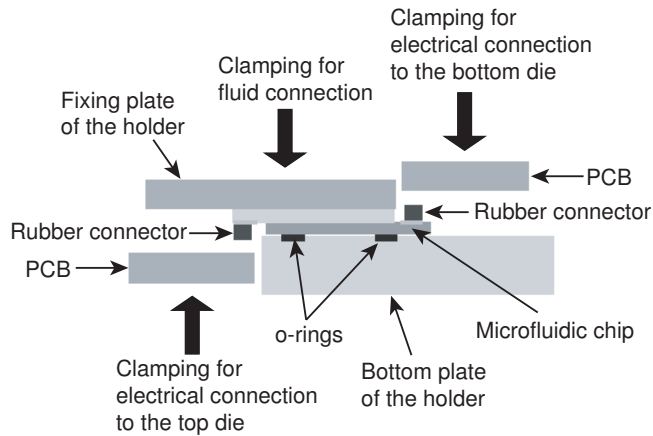


Figure 7.2: Schematics of the double clamping system.

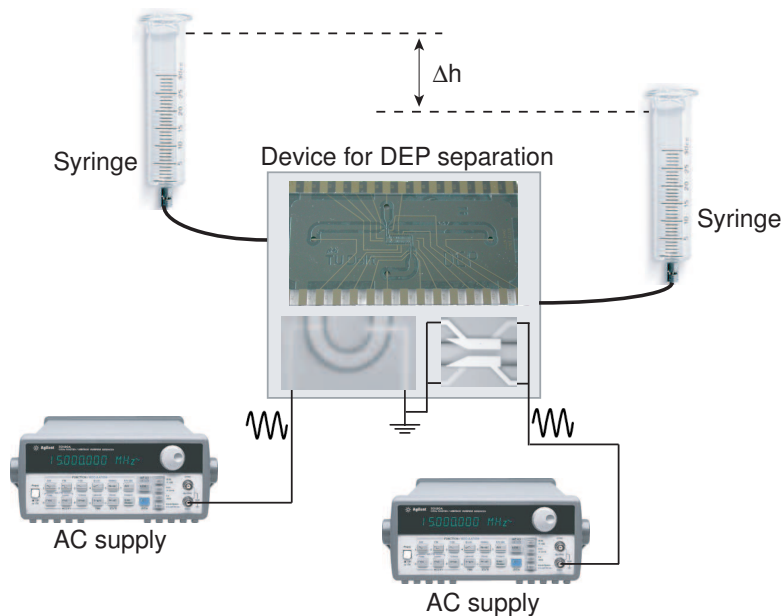


Figure 7.3: Schematics showing the fluid and the electrical connections on the device for the DEP separation.

combination with an emission filter ( $\lambda=600-660$  nm), both from Olympus. The schematics showing the fluid and the electrical connections on the DEP device is depicted in Figure 7.3. To apply the electric fields, AC supplies (HP33120A arbitrary waveform generator) were connected to the chip via the electrical interface on the holder. In order to check the applied voltage, an oscilloscope (HP54601B) was used. The continuous flow was generated by the pressure difference between the inlet and the outlet. The flow velocity was controlled by tuning the height difference of the liquid surface levels in the reservoirs. A summary of the equipments used in the experiments is listed in Table 7.1.

After several experiments, many PS particles adhered to the wall surface will be left in the channel. Toluene was found capable of dissolving the PS particle. Therefore, flushing the channel with toluene for 2-3 times will effectively get rid of all the residual PS particles. After cleaned with Demi-water, the device could be re-used for many times of experiments, and no deterioration in performance was observed.

Table 7.1: Used equipments and materials.

Equipment/Material	Type
Syringe	BD Plastipak, 50 mL
Particles	Carboxylated PS particle, Invitrogen
AC supply	HP33120A arbitrary waveform generator
Oscilloscope	HP54601B
Microscope	IX71 inverted microscope, Olympus
Camera	ColorView II, Olympus
Imaging software	analySIS docu, Olympus

### 7.2.2 Dielectrophoretic focusing

To evaluate the focusing effect of the top-and-bottom focusing electrodes, 2  $\mu\text{m}$  PS particles were utilized which experience negative DEP and would be focused to the channel center. Each picture in Figure 7.4 shows a time-lapse sequence of images exhibiting the trajectories of several different particles. These pictures were formed from the superposition of 150 successive video images. When the voltage is off, the particles are distributed randomly in the channel, as shown in the figure. The particles start being focused when the applied voltage is increased. When the applied peak-to-peak voltage is increased to 10 V, all the particles are repelled to the center of the channel. At 15 V, the particles are focused to an even tighter band. Focusing occurred in the vertical direction was demonstrated by setting the focusing plane of the objective to the middle height of the channel. The particles observed out of focus before passing the electrodes come into focus after passing the electrodes.

The voltages required to focus 2  $\mu\text{m}$  PS particles at different flow velocities were measured and are shown in Figure 7.5. Two groups of measured data are for two types of electrodes, i.e. the electrodes in direct contact with electrolytes and the electrodes insulated by 200 nm oxide, respectively. The voltages required on the insulated electrodes are relatively higher since there is a voltage drop on the oxide layer. The simulated data for particle focusing, which plotted in the same figure, are very comparable with the measured data for both types of electrodes.

### 7.2.3 Dielectrophoretic repelling in the curve

The DEP repelling effect in the curve was also demonstrated, over which a 10 V peak-to-peak voltage was applied. The trajectories of a 4  $\mu\text{m}$  PS particle at different velocities were obtained by superimposing successive video images, as shown in Figure 7.6. Before entering the curve, the particle has already been brought to the channel center by the focusing electrodes. At a high flow velocity, the particle follows the streamline of the flow and does not have any deflection

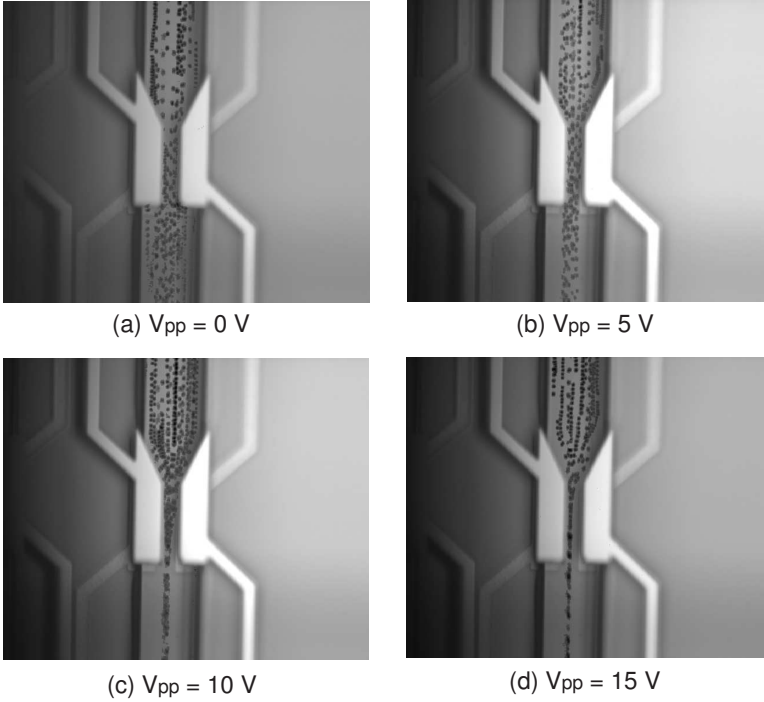


Figure 7.4: Pictures showing how increasing the applied voltage will influence the particle focusing.

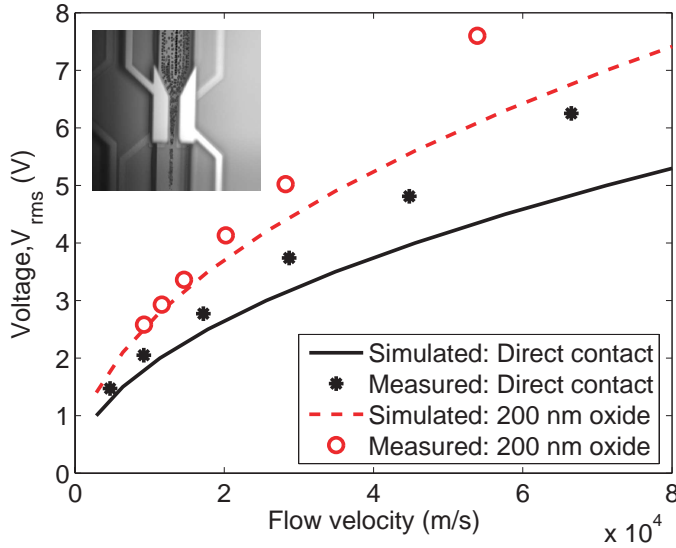


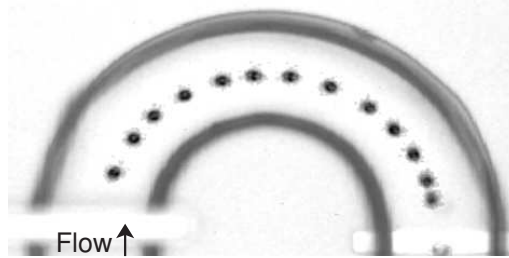
Figure 7.5: Measured and simulated voltages for the focusing of  $2\ \mu\text{m}$  particles at different flow velocities.

in the lateral direction. When the flow velocity is decreased, the DEP repelling effect becomes significant. The particle is driven to the outer tracks and finally end up at the outer sidewall of the curve. It can be seen that the distance of the particle in two successive images became shorter when it came closer to the outer sidewall. This indicates the flow velocity gradient inside the channel.

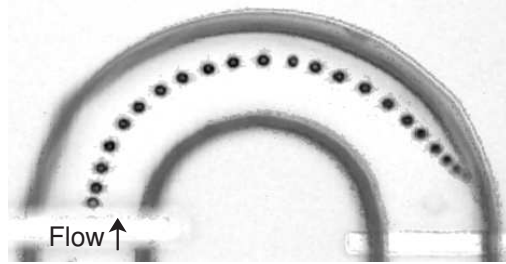
#### 7.2.4 Measured separation

The separation of  $2\ \mu\text{m}$  and  $4\ \mu\text{m}$  PS particles was measured in terms of retention time. The liquid buffer was driven forward along the channel at a velocity of  $200\ \mu\text{m/s}$  (center velocity) by syringe reservoirs. A voltage of  $3.5\ \text{V}$  (RMS,  $2\ \text{MHz}$ ) was applied to the focusing electrodes to concentrate both  $2\ \mu\text{m}$  and  $4\ \mu\text{m}$  particles to the channel center. When a voltage of  $7.1\ \text{V}$  (RMS,  $2\ \text{MHz}$ ) was applied over the curves, the retention time in a fragment of the separation channel containing 4 curves was measured. 25 measurements were taken for each type of particles and the result is plotted in the form of histogram as shown in Figure 7.7, from which we could clearly see the separation. The time deviation in the same type of particles is mainly due to the variation of particle size, which has a coefficient of about 5%. The mean retention time of each type of particle was calculated and shown in Table 7.2. The  $4\ \mu\text{m}$  particles turn out to take an average 10%

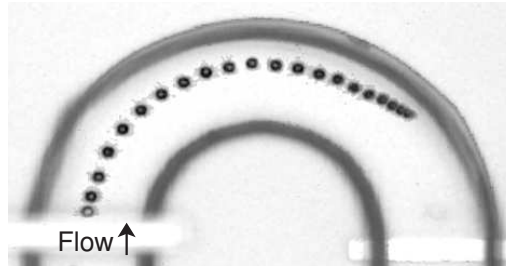




(a) High flow velocity



(b) Medium flow velocity



(c) Low flow velocity

Figure 7.6: Pictures showing the DEP repelling effect in the curve and how the flow velocity change influences the particle movement in the curve.

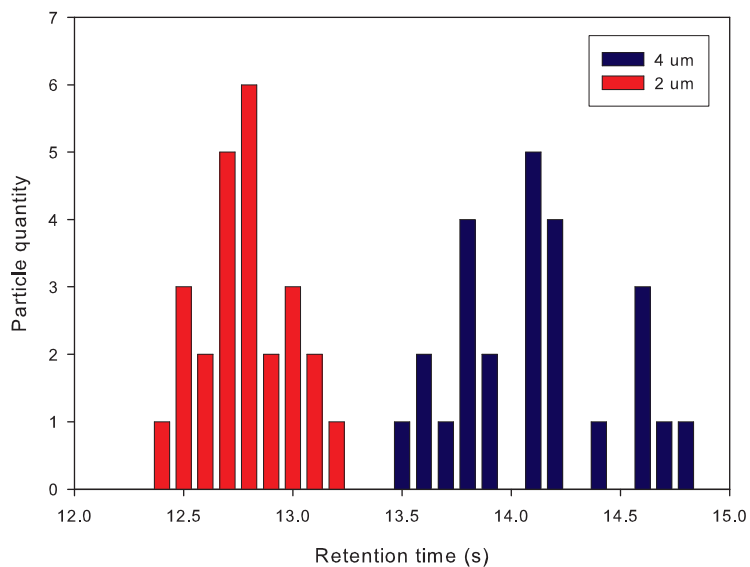


Figure 7.7: Histogram for the retention time of two different size particles.

Table 7.2: Measured mean retention time of two different size particles.

Particle diameter	Mean retention time
2 $\mu\text{m}$	12.8 s
4 $\mu\text{m}$	14.1 s

longer retention time than the 2  $\mu\text{m}$  particles, which proves the concept. The retention time of these two types of particles was simulated in the same ways as introduced in Chapter 3. The simulated retention time of the 4  $\mu\text{m}$  particles is 7.2% longer than that of the 2  $\mu\text{m}$  particles. Compared with the simulated result, the measured separation is a bit larger, which is due to the other dimensional separation in the vertical direction caused by the planar electrodes at the access of the curves.

## 7.3 Experiments on the moving field CE device

### 7.3.1 Measurement setups

To track the electroosmotic flow, neutral particles must be used. The previously used carboxylated polystyrene particles, which are produced slightly negatively charged to avoid agglomeration, is not appropriate for this experiment. Therefore, 366 nm (in diameter) Rhodamine B MF particles (microParticles GmbH, Germany), which have zero charge at buffer pH value around 6.7, were chosen. The buffer used was Demi-water, additional  $H^+$  makes its pH a bit lower than 7.

The holder containing the microfluidic chip was mounted onto the table of an inverted microscope (IX71, Olympus) equipped with a low noise self-cooling CCD camera (ColorView II, Olympus). The images or the videos were acquired by an imaging software (analySIS docu, Olympus) for further data process and analysis. The schematics showing the fluid and the electrical connections on the DEP device is depicted in Figure 7.3. To apply the DC electric fields, two DC voltage supplies (E303-3 Delta Elektronika) were connected to the chip via the electrical interface on the holder. One voltage ( $V_\alpha$ ) was applied over a segment of the separation channel, and the other voltage ( $V_\beta$ ) was applied over the EOP segment. When feeding the channel with liquid, small bubbles are prone to be generated around the slender channel array, as shown in Figure 7.9. Therefore, the flow direction was arranged in such a way that the EOP segment locates at the downstream of the separation channel. This can prevent the small bubbles from entering the separation channel. In order to eliminate the pressure difference on the micro-channel during operation, the syringes with large diameters were used, and the liquid surfaces in the syringe reservoirs were placed to the same height.

### 7.3.2 Measured flow distortion compensation

When  $V_\alpha$  was switched on, an electroosmotic flow was immediately built up in the field region. The particles in the channel started traveling in opposite directions due to the back pressure effect. When the pump voltage  $V_\beta$  was switched on and increased to a certain level, the particles at the channel center turned around and started moving in the same direction and at the same speed as the particles near the channel walls. This pump voltage was measured with respect to different  $V_\alpha$ , and the result is shown in Figure 7.10. The slope of the fitting-trend line for the measured data exhibits a voltage ratio of 1.38, which is higher than the calculated ratio derived by using the equivalent circuit model, as shown in Figure 7.10. The mismatch can be due to the following two reasons: The calculated flow resistance of the channels is an approximated value of the real fabricated channels; The bubbles generated in the EOP region interrupted the operation of some slender channels.

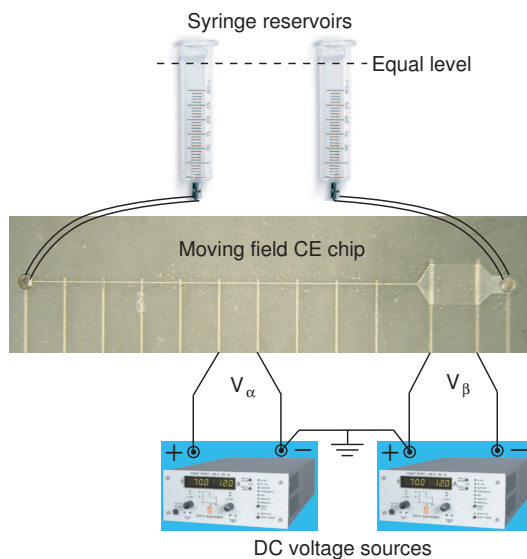


Figure 7.8: Schematics showing the fluid and the electrical connections on the moving field CE device.

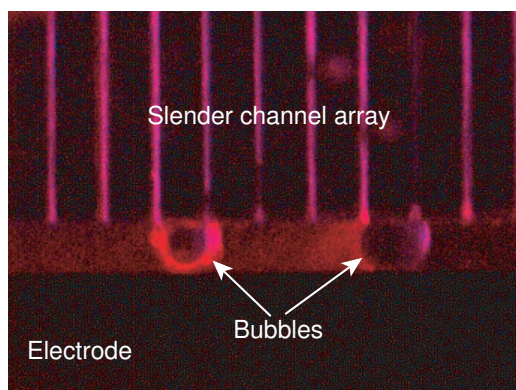


Figure 7.9: Bubbles generated in the EOP segment.

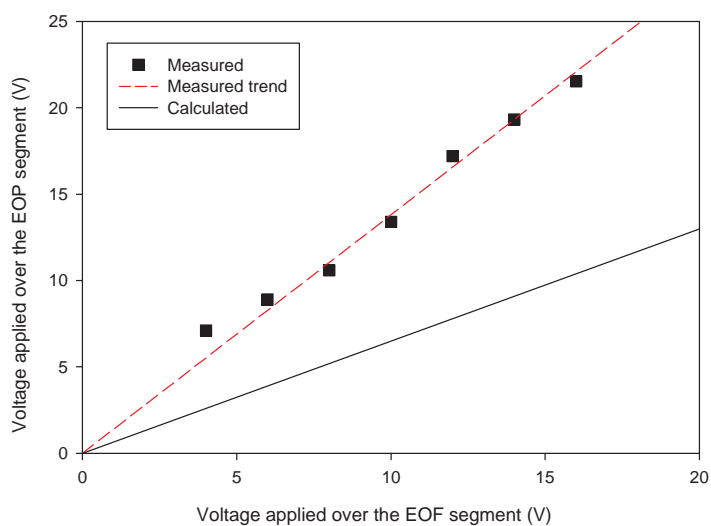


Figure 7.10: A comparison between the measured and the calculated voltage ratios for flow distortion compensation.



## Chapter 8

# Conclusions and Future Work

### 8.1 Conclusions

In this thesis, two separation methods were proposed and investigated with the aim of substituting the conventional microfluidic CE method which is currently used only in laboratory situation for off-line measurement largely due to the high separation voltage required. In the first DEP method, the curved parts of a serpentine channel are effectively used for dielectrophoretic separation, based on the fact that the electric field gradient in the curves generates simultaneously a flow velocity gradient and a dielectrophoretic force field orthogonal to the direction of flow. The second method moving field CE is basically an evolution version of the traditional CE, in which the required separation voltage is significantly reduced by bringing the electrodes into the channel so as to decrease the span between the electrodes. And the separation voltage is switched between these small span electrodes in such a way that it is always applied to the part of the channel where the sample plug resides.

In the DEP device, the curves are the essential parts where the dielectrophoretic separation takes place. Compared with a DC electric field, a DC-biased AC electric field allows much smaller particle separation in a curve, since applying an AC voltage with a DC offset over a curve decouples the dielectrophoresis from the electroosmosis. By controlling the ratio of AC to DC amplitudes, the separation of samples with various size distributions can be achieved. The separation sensitivity was found to have a second order dependence on the ratio of AC to DC amplitudes and a linear dependence on the particle size. In the presence of Brownian motion, the AC plus the DC amplitudes should be larger than the threshold voltage to

achieve a deterministic separation. Since the curves are bended in the opposite directions, the separation will be canceled to a great extent in the next curve. Therefore, focusing must be performed in between two successive curves. In terms of focusing, the top-and-bottom electrode structure performs superior to the planar array for negative DEP because stronger electric field gradients are generated and particles are forced away from walls where nonuniform flow and nonspecific particle adhesion can occur. A high frequency AC is preferred in order to minimize the AC perturbation on the flow in the curves and the induced charge electroosmosis in the vicinity of the AC electrodes. Since the hydrodynamic flow profile in a curve also decreases monotonously from the channel center to the outer sidewall, we could use the same device for both hydrodynamic DEP separation and electrokinetic DEP separation. With a higher flow gradient, the hydrodynamic DEP is expected to produce a larger separation than the electrokinetic DEP. The fabricated DEP device consists of three layers: two processed substrates bonded together with an SU-8 layer sandwiched in between. In order to demonstrate the DEP effect with moderate voltage levels, 2 and 4  $\mu\text{m}$  polystyrene beads were used in the experiments. The DEP movement of a 4  $\mu\text{m}$  PS particle was experimentally observed in a curve, over which a 10 V peak-to-peak voltage was applied. The particles are driven to the outer tracks and finally reaches the outer sidewall of the curve at a low flow velocity. The distance of the particle in two successive images becomes shorter when it comes closer to the outer sidewall, which indicates the flow velocity gradient inside the channel. The focusing effect of the trapezoidal top-and-bottom electrodes were demonstrated by utilizing 2  $\mu\text{m}$  PS particles. At a peak-to-peak voltage of 10 V, all the particles are focused to the channel center. Focusing occurred in the vertical direction was demonstrated by setting the focusing plane of the objective to the middle height of the channel. The particles observed out of focus before passing the electrodes become in focus after passing the electrodes. The retention time of 2 and 4  $\mu\text{m}$  PS particles in a channel fragment containing 4 curves was measured in the case of hydrodynamic DEP. The 4  $\mu\text{m}$  particles turn out to take an average 10% longer retention time than the 2  $\mu\text{m}$  particles, which proves the concept.

It was revealed that applying a DC voltage over a fraction of the channel will evoke flow profile distortion in moving field CE operation, and will in turn cause plug dispersion. For a given voltage, the smaller fraction it is applied on, the larger distortion will be caused in the EOF region. By extracting and analyzing the equivalent circuits of the fluid system, the flow profile distortion was found can be considered as a consequence of the backward flow. The method we proposed is to generate, by using an electroosmotic pump (EOP), a forward flow and cancel the backward flow in the EOF segment. Two pump structures were proposed, with which the driving voltage of the pump could be reduced to the same level as the voltage required for separation. The first structure is an array of slender channels, and the second structure is a broad thin channel. In order to minimize the flow loss, the channel arrays are suggested also to be used in the sample injection



channels to increase the flow resistance. It was proved by simulation that in the presence of slender-channel arrays a small increase in the pump driving voltage will be enough to compensate the flow loss via the side channels. The moving field CE prototype device was fabricated by laminating two layers of dry film resist onto a processed glass substrate. The channel structure is defined in the first dry film resist layer and the second acts as the lid of the channel. To first verify the compensation technique neglecting flow loss, experiments were carried out with the devices that does not consist of sample injection channels. The flow distortion compensation can be observed when the EOP driving voltage is increased to a certain level. The required EOP driving voltages with respect to different separation voltages were measured and exhibit a linear relationship as expected.

To detect cells at extremely low concentration, we additionally proposed a biomass concentration detection method in which an electrokinetic technology is used for rapidly increasing the concentration of the cells while measuring the concentration. Due to the dielectric contrast between the viable cell and the surrounding medium, the cells could be trapped and collected by the positive dielectrophoresis. Based on the simplified model, the frequency dependence of the induced dipole strength of the yeast cell was studied by computer methods. The threshold DEP force needs to dominate the Brownian motion for successfully trapping the cells was investigated. This threshold force defines a trapping space which depends on the applied voltage and the flow velocity of the fluid. To achieve accurate and sensitive detection, the 4-electrode conductivity detector was suggested to be used. The change speed of the measured conductivity corresponds to the concentration of the yeast cells in the aqueous suspension.

## 8.2 Future work

### 8.2.1 DEP separation in iterative curves

For the DEP device, it has been demonstrated by calculation and simulation that nanoparticles can be separated with enough high voltages. The temperature change due to Joule heating caused by those voltages remains to be investigated experimentally, since the temperature raise will have nontrivial effect on the fluid flow and the biological samples.

The characterization of this device has been performed by using polystyrene particles so far. It was recommend to further investigate the possibility of this device by using biological samples (e.g. proteins and peptides). When the separation of these biological samples is demonstrated, this device can be developed for a wide range of applications.

### 8.2.2 Moving field CE

For the moving field CE device, the degree of profile flatness of the compensated electroosmotic flow remains to be investigated. Two approaches are recommended to be used for this investigation: Evaluating the flow profile in the EOF region by using PIV technique would give a precise image of the flatness; By injecting a fluorescent sample plug and analyzing the fluorescent image of sample zone dispersion in the EOF region, the flatness of the flow profile could be retrieved as well.

There is still room for improvement in the fabrication process. The next generation devices are suggested to be constructed by direct bonding of glass and silicon substrates, which will have better durability and stability than the prototypes constructed by the dry film resist. A better channel uniformity could also be achieved by deposition of an oxide layer on both substrates.

In future projects, the electronics for the control unit need to be designed, which can realize automatic control of the sample injection, the movement of the electric field, and the plug dispersion compensation process. The control unit should also be able to communicate with the detector at the end of the channel, so as to measure the electroosmotic flow and adjust the field moving speed based on real-time situation.

### 8.2.3 Biomass concentration detection

The glass microchip containing electrodes for cell trapping and conductivity detection has been fabricated. The readout circuits, the measurement setup and the Labview code have also been verified by using ideal resistors to mimic the environment of a liquid suspension. In the next step, yeast cells are suggested to be used first to evaluate the trapping effect and then to prove the concept of the detection. By varying the voltage levels applied on the trapping electrodes, we could try to capture and measure different types of cells in the liquid suspension. Besides, the bulky lock-in amplifier used in the hardware setup might be miniaturized later to allow an complete integration into a micro-module.

### 8.2.4 System integration

In order to form an real-time in-line analytical system, a number of other aspects should be investigated apart from the ones mentioned above. Sampling is an important issue not addressed yet. It is very difficult to avoid contamination of the system that samples are taken from. Furthermore, the sample should be representative of the process being sampled from. The sample volumes to be injected will be in the nanoliter range, which implies that the analytical device must be as close as possible to the sampling source to reduce dead volumes.

Sample pre-treatment is another crucial part of this development, which may involve filtration, dialysis, separation based on molecular size or based on other relevant features of the analytes to be quantified. The detector is very important for the entire system. A sensitive and stable contactless conductivity detector has been developed by F. Laugere [76]. However, the integration of this detector into the proposed separation microchips remains to be investigated with respect to the microfabrication process. The device periphery of a separation microchip consists of a sampling unit, an external power supply, external detector electronics as well as a data transmitter. To achieve an independent system, the power could be supplied either by a battery or with an on-board power generator. Two points are essential for the miniaturization of all the components involved: wireless communication and low power consumption.



# Bibliography

- [1] N. Cleland and S. O. Enfors. Monitoring glucose consumption in an escherichia coli cultivation with an enzyme electrode. *Anal. Chim. Acta.*, 163: 281–285, 1984.
- [2] C. Menzel, T. Lerch, K. Schneider, R. Weidemann, C. Tollnick, G. Kretzmer, T. Scheper, and K. Schugerl. Application of biosensors with an electrolyte isolator semiconductor capacitor (eis-cap) transducer for process monitoring. *Process Biochem.*, 33:175–180, 1998.
- [3] P. Norlin, O. Ohmann, B. Ekstrom, and L. Forssen. A chemical micro analysis system for the measurement of pressure, flow rate, temperature, conductivity, uv-adsorption and fluorescence. *Sensors and Actuators B*, 49:34–39, 1998.
- [4] S. Sivakesava, J. Irudayaraj, and D. Ali. Simultaneous determination of multiple components in lactic acid fermentation using ft-mir, nir, and ft-raman spectroscopic techniques. *Process Biochem.*, 37:371–378, 2001.
- [5] I. Notingher, J. Selvakumaran, and L. L. Hench. New detection system for toxic agents based on continuous spectroscopic monitoring of living cells. *Biosens. Bioelectron.*, 20:780–789, 2004.
- [6] K. Schugerl. Progress in monitoring, modeling and control of bioprocesses during the last 20 years. *J. Biotechnol.*, 20:149–173, 2001.
- [7] A. Plum05 and A. Rehorek. Strategies for continuous on-line high performance liquid chromatography coupled with diode array detection and electrospray tandem mass spectrometry for process monitoring of sulphonated azo dyes and their intermediates in anaerobic-aerobic bioreactors. *J. Chromatogr. A*, 1084:119–133, 2005.
- [8] K. M. Williams, P. Fox, and T. Marshall. A comparison of protein assays for the determination of the protein-concentration of beer. *J. Inst. Brew.*, 101: 365–369, 1995.

- [9] A. Curioni, G. Pressi, and L. Furegon. Major proteins of beer and their precursors in barley - electrophoretic and immunological studies. *J. Agric. Food Chem.*, 43:2620–2626, 1995.
- [10] P. Bednar, Z. Aturki, Z. Stransky, and S. Fanali. Chiral analysis of uv nonabsorbing compounds by capillary electrophoresis using macrocyclic antibiotics: 1. separation of aspartic and glutamic acid enantiomers. *Electrophoresis*, 22: 2129–2135, 2001.
- [11] S. Gorinstein, M. Zemser, O. Paredes-Lopes Ch. Scheler J. Salnikow O. Martin-Belloso F. Vargas-Albores, J. L. Ochoa, and S. Trakhtenberg. Proteins and amino acids in beers, their contents and relationships with other analytical data. *Food Chem.*, 67:71–78, 1999.
- [12] D. Li. *Electrokinetics in Microfluidics*. Academic Press.
- [13] A. Ramos, H. Morgan, N. G. Green, and A. Castellanos. Ac electric-field-induced fluid flow microelectrodes. *Journal of colloid and interface science*, 217:420–422, 1999.
- [14] N. G. Green, A. Ramos, H. Morgan A. Gonzalez, and A. Castellanos. Fluid flow induced by nonuniform ac electric fields in electrolytes on microelectrodes. i. experimental measurements. *Phys. Rev. E*, 61:4011–4018, 2000.
- [15] A. Gonzalez, A. Ramos, N. G. Green, H. Morgan, and A. Castellanos. Fluid flow induced by nonuniform ac electric fields in electrolytes on microelectrodes. ii. a linear double-layer analysis. *Phys. Rev. E*, 61:4019–4028, 2000.
- [16] F. Nadal, F. Argoul, P. Kestener, B. Pouligny, C. Ybert, and A. Ajdari. Electrically induced flows in the vicinity of a dielectric stripe on a conducting plane. *Eur. Phys. J. E*, 9:387–399, 2002.
- [17] N. G. Green, A. Ramos, A. Gonzalez, H. Morgan, and A. Castellanos. Fluid flow induced by nonuniform ac electric fields in electrolytes on microelectrodes. iii. observation of streamlines and numerical simulation. *Phys. Rev. E*, 66:026305, 2002.
- [18] D. J. Harrison, A. Manz, Z. Fan, H. Ludi, and H. M. Widmer. Capillary electrophoresis and sample injection systems integrated on a planar glass chip. *Anal. Chem.*, 64:1926–1932, 1992.
- [19] A. Manz, D. J. Harrison, E. M. J. Verpoorte, J. C. Fettingner, A. Paulus, H. Ludi, and H. M. Widmer. Planar chips technology for miniaturization and integration of separation techniques into monitoring systems : Capillary electrophoresis on a chip. *Journal of Chromatography*, 593:253–258, 1992.
- [20] G. M. Greenway, S. J. Haswell, and P. H. Petsul. Characterisation of a micro-total analytical system for the determination of nitrite with spectrophotometric detection. *Analytica Chimica Acta*, 387:1–10, 1999.

- 
- [21] N. Malcik, J. P. Ferrance, J. P. Landers, and P. Caglar. The performance of a microchip-based fiber optic detection technique for the determination of  $\text{Ca}^{2+}$  ions in urine. *Sensors and Actuators B*, 107:24–31, 2005.
- [22] E. X. Vrouwe, R. Luttge, W. Olthuis, and A. van den Berg. Microchip analysis of lithium in blood using moving boundary electrophoresis and zone electrophoresis. *Electrophoresis*, 26:3032–3042, 2005.
- [23] E. X. Vrouwe, R. Luttge, W. Olthuis, and A. van den Berg. Rapid inorganic ion analysis using quantitative microchip capillary electrophoresis. *Journal of Chromatography A*, 1102:287–293, 2006.
- [24] S. Sirichai and A. J. de Mello. A capillary electrophoresis microchip for the analysis of photographic developer solutions using indirect fluorescence detection. *Analyst*, 125:133–137, 2000.
- [25] M. Zuborova, M. Masar, D. Kaniansky, M. Johnck, and B. Stanislawski. Determination of oxalate in urine by zone electrophoresis on a chip with conductivity detection. *Electrophoresis*, 23:774–781, 2002.
- [26] J. Kameoka, H. G. Craighead, H. W. Zhang, and J. Henion. A polymeric microfluidic chip for ce/ms determination of small molecules. *Analytical Chemistry*, 73:1935–1941, 2001.
- [27] S. Gotz, T. Revermann, and U. Karst. Quantitative on-chip determination of taurine in energy and sports drinks. *Lab Chip*, 7:93–97, 2007.
- [28] C. D. Garcia, G. Engling, P. Herckes, J. L. Collett, and C. S. Henry. Determination of levoglucosan from smoke samples using microchip capillary electrophoresis with pulsed amperometric detection. *Environ. Sci. Technol.*, 39:93–97, 2005.
- [29] Y. Y. Wu and J. M. Lin. Determination of phenol in landfill leachate by using microchip capillary electrophoresis with end-channel amperometric detection. *Journal of Separation Science*, 29:137–143, 2006.
- [30] Y. Q. Guan, T. Wu, M. Lin, and J. N. Ye. Determination of pharmacologically active ingredients in sweet potato (*ipomoea batatas* L.) by capillary electrophoresis with electrochemical detection. *Journal of Agricultural and Food Chemistry*, 54:24–28, 2006.
- [31] H. Morgan, M. P. Hughes, and N. G. Green. Separation of submicron bioparticles by dielectrophoresis. *Biophysical Journal*, 77:516–525, 1999.
- [32] G. H. Markx, P. A. Dyda, and R. Pethig. Dielectrophoretic separation of bacteria using a conductivity gradient. *J. Biotech.*, 51:175–180, 1996.
-

- [33] Y. Huang, R. Holzel, R. Pethig, and X. Wang. Differences in the ac electrodynamics of viable and nonviable yeast cells determined through combined dielectrophoresis and electrorotation studies. *Phys. Med. Biol.*, 37:1499–1517, 1992.
- [34] J. G. Kralj, M. T. W. Lis, M. A. Schmidt, and K. F. Jensen. Continuous dielectrophoretic size-based particle sorting. *Anal. Chem.*, 78:5019–5025, 2006.
- [35] S. Choi and J. K. Park. Microfluidic system for dielectrophoretic separation based on a trapezoidal electrode array. *Lab Chip*, 5:1161–1167, 2005.
- [36] I. Doh and Y. H. Cho. A continuous cell separation chip using hydrodynamic dielectrophoresis (dep) process. *Sensors and Actuators A*, 121:1161–1167, 2005.
- [37] Y. L. Li, C. Dalton, H. J. Crabtree, G. Nilsson, and K. Kaler. Continuous dielectrophoretic cell separation microfluidic device. *Lab chip*, 7:239–248, 2007.
- [38] C. F. Chou, J. O. Tegenfeldt, O. Bakajin, S. S. Chan, and E. C. Cox. Electrodeless dielectrophoresis of single- and double-stranded dna. *Biophy. J.*, 83:2170–2179, 2002.
- [39] C. F. Chou and F. Zenhausern. Electrodeless dielectrophoresis for micro total analysis system. *IEEE Eng. in medicine and biology magazine*, pages 62–67, 2003.
- [40] E. B. Cummings and A. K. Singh. Dielectrophoresis in microchips containing arrays of insulating posts: Theoretical and experimental results. *Anal. Chem.*, pages 4724–4731, 2003.
- [41] B. H. Lapizco-Encinas, B. A. Simmons, E. B. Cummings, and Y. Fintschenko. Insulator-based dielectrophoresis for the selective concentration and separation of live bacteria in water. *Electrophoresis*, pages 1695–1704, 2004.
- [42] K. H. Kang, Y. Kang, X. Xuan, and D. Li. Continuous separation of microparticles by size with direct current-dielectrophoresis. *Electrophoresis*, 27: 694–702, 2006.
- [43] Y. Kang, D. Li, S. A. Kalams, and J. E. Eid. Dc-dielectrophoretic separation of biological cells by size. *Biomed Microdevices*, 10:243–249, 2008.
- [44] I. Barbulovic-Nad, X. Xuan, J. S. H. Lee, and D. Li. Dc-dielectrophoretic separation of microparticles using an oil droplet obstacle. *Lab chip*, pages 274–379, 2006.
- [45] S. Miltenyi, W. Muller, W. Weichel, and A. Radbruch. High gradient magnetic cell separation with macs. *Cytometry*, 11:231–238, 1990.



- [46] G. Blankenstein and U. D. Larsen. Modular concept of a laboratory on a chip for chemical and biochemical analysis. *Biosensors and Bioelectronics*, 13:427–438, 1998.
- [47] C. H. Ahn, M. G. Allen, W. Trimmer, Y. Jun, and S. Erramilli. A fully integrated micromachined magnetic particle separator. *Journal of Microelectromechanical System*, 5:151–158, 1996.
- [48] A. C. Siegel, S. S. Shevkoplyas, D. B. Weibel, D. A. Bruzewicz, A. W. Martinez, and G. M. Whitesides. Cofabrication of electromagnets and microfluidic systems in poly(dimethylsiloxane). *Angew. Chem., Int. Ed.*, 45:6877–6882, 2006.
- [49] N. Pamme and A. Manz. On-chip free-flow magnetophoresis: Continuous flow separation of magnetic particles and agglomerates. *Anal. Chem.*, 76:7250–7256, 2004.
- [50] N. Pamme and C. Wilhelm. Continuous sorting of magnetic cells via on-chip free-flow magnetophoresis. *Lab on a Chip*, 6:974–980, 2006.
- [51] J. J. Hawkes and W. T. Coakley. Force field particle filter, combing ultrasound standing waves and laminar flow. *Sensors and Actuators B*, 75:213–222, 2001.
- [52] F. Petersson, A. Nilsson, C. Holm, H. Jonsson, and T. Laurell. Continuous separation of lipid particles from erythrocytes by means of laminar flow and acoustic standing wave forces. *Lab Chip*, 5:20–22, 2005.
- [53] F. Petersson, L. Aberg, A. M. Sward-Nilsson, and T. Laurell. Free flow acoustophoresis: Microfluidic-based mode of particle and cell separation. *Anal. Chem.*, 79:5117–5123, 2007.
- [54] L. Paterson, E. Papagiakoumou, G. Milne, V. Garces-Chavez, S. A. Tatarikova, W. Sibbett, F. J. Gunn-Moore, P. E. Bryant, A. C. Riches, and K. Dholakia. Light-induced cell separation in a tailored optical landscape. *Applied Physics Letter*, 87:123901, 2005.
- [55] M. P. MacDonald, G. C. Spalding, and K. Dholakia. Microfluidic sorting in an optical lattice. *Nature*, 426:421–424, 2003.
- [56] G. Milne, D. Rhodes, M. MacDonald, and K. Dholakia. Fractionation of polydisperse colloid with acousto-optically generated potential energy landscapes. *Optics Letters*, 32:1144–1146, 2007.
- [57] T. B. Jones. *Electromechanics of Particles*. Cambridge Univ. Press, New York, 1995.

- [58] A. Einstein. on the movement of small particles suspended in stationary liquids required by the molecular-kinetic theory of heat. *Annalen der Physik*, 17:549–560, 1905.
- [59] J. H. Nieuwenhuis and M. J. Vellekoop. Simulation study of dielectrophoretic particle sorters. *Sensors and Actuators B*, 103:331–338, 2004.
- [60] S. Fiedler, S. G. Shirley, T. Schnelle, and G. Fuhr. Dielectrophoretic sorting of particles and cells in a microsystem. *Anal. Chem.*, 70:1909–1915, 1998.
- [61] T. Muller, G. Gradl, S. Howitz, S. Shirley, T. Schnelle, and G. Fuhr. A 3-d microelectrode system for handling and caging single cells and particles. *Biosens. Bioelectron.*, 14:247–256, 1999.
- [62] E. V. Dose and G. Guiochon. Timescales of transient processes in capillary electrophoresis. *Journal of Chromatography A*, 652:263–275, 1993.
- [63] P. Dutta and A. Beskok. Analytical solution of time periodic electroosmotic flows: analogies to stokes’ second problem. *Anal. Chem.*, 73:5097–5102, 2001.
- [64] R. S. Pai, T. J. Roussel, M. M. Crain, D. J. Jackson, J. A. Conklin, R. P. Baldwin, R. S. Keynton, J. F. Naber, and K. M. Walsh. Integrated electrochemical detection for lab on a chip analytical microsystems. *Proceedings of the Fourteenth Biennial University/Government/Industry Microelectronics Symposium*, pages 167–170, 2001.
- [65] Y. C. Lin. Design of low voltage-driven capillary eletrophoresis chips using moving electrical fields. *Sensors and Actuators B*, 80:33–40, 2001.
- [66] Y. Lin and W. Wu. Arrayed-electrode design for moving electric field driven capillary electrophoresis chips. *Sensors and Actuators B*, pages 54–62, 2001.
- [67] S. P. Suter and R. Skalak. Design of low voltage-driven capillary eletrophoresis chips using moving electrical fields. *Annu. Rev. Fluid Mech.*, 25:1–19, 1993.
- [68] R. B. M. Schasfoort, S. Schlautmann, J. Hendrikse, and A. van de Berg. Field-effect flow control for microfabricated fluidic networks. *Science*, 286:942–945, 1999.
- [69] N. J. Sniadecki, C. S. Lee, P. Sivanesan, and D. L. DeVoe. Induced pressure pumping in polymer microchannels via field-effect flow control. *Anal. Chem.*, 76:1942–1947, 2004.
- [70] R. J. Hunter. *Zeta potential in colloid science*. Academic Press.
- [71] E. van der Wouden. *Field Effect Flow Control of Electro-osmotic Flow in Microfluidic Networks*. Wohrmann Print Service, Zutphen, 2006.

- 
- [72] L. Fu and R. Yang. Low-voltage driven control in electrophoresis microchips by traveling electric field. *Electrophoresis*, 24:1253–1260, 2003.
- [73] K. Cai, M. Frant, J. Bossert, G. Hildebrand, K. Liefeth, and K. D. Jandt. Surface functionalized titanium thin films: Zeta-potential, protein adsorption and cell proliferation. *Colloids and Surfaces B: Biointerfaces*, 50:1–8, 2006.
- [74] B. J. Kirby and E. F. Hasselbrink. Zeta potential of microfluidic substrates: 1. theory, experimental techniques, and effects on separations. *Electrophoresis*, 25:187–202, 2004.
- [75] E. E. Krommenhoek, J. G. E. Gardeniers, A. van de Berg J. G. Bomer, X. Li, M. Ottens, L. A. M. van der Wielen, G. W. K. van Dedem, M. van Leeuwen, W. M. van Gulik, and J. J. Heijnen. Monitoring of yeast cell concentration using a micromachined impedance sensor. *Sensors and Actuators B*, 115: 187–202, 2006.
- [76] F. Laugere. *Conductivity detection for application in capillary electrophoresis microchips*. Optima Grafische Communicatie, Rotterdam, 2003.
- [77] T. P. Hunt and R. M. Westervelt. Dielectrophoresis tweezers for single cell manipulation. *Biomed Microdevices*, 8:227–230, 2006.
- [78] N. P. Pham, E. Boellaard, J. N. Burghartz, and P. M. Sarro. Photoresist coating methods for the integration of novel 3-d rf microstructures. *Journal of microelectromechanical systems*, 13:491–499, 2007.
- [79] E. Kukhareuka, M. M. Farooqui, L. Grigore, M. Kraft, and N. Hollinshead. Electroplating moulds using dry film thick negative photoresist. *Journal of Micromechanics and Microengineering*, 13:S67–S74, 2003.
- [80] I. Chartier, J. Sudor, Y. Fouillet, N. Sarrut, C. Bory, and A. Gruss. Fabrication of an hybrid plastic-silicon microfluidic device for high-throughput genotyping. *Proc. SPIE-Int. Soc. Opt. Eng.*, 4982:208–219, 2003.
- [81] S. Schlautmann, H. Wensink, R. Schasfoort, M. Elwenspoek, and A. van den Berg. Powder-blasting technology as an alternative tool for microfabrication of capillary electrophoresis chips with integrated conductivity sensors. *Journal of Micromechanics and Microengineering*, 11:386–389, 2001.
- [82] P. Vulto, N. Glade, L. Altomare, J. Bablet, L. Del Tin, G. Medoro, I. Chartier, and N. Maresi. Microfluidic channel fabrication in dry film resist for production and prototyping of hybrid chips. *Lab on chip*, 5:158–162, 2005.
- [83] J. Carlier, S. Arscott, V. Thomy, J. C. Fourier, F. Caron, J. C. Camart, C. Druon, and P. Tabourier. Integrated microfluidics based on multi-layered su-8 for mass spectrometry analysis. *J. Micromech. Microeng.*, 14:619–624, 2004.

- [84] Y. J. Song, C. S. S. R. Kumar, and J. Hormes. Fabrication of an su-8 based microfluidic reactor on a peek substrate sealed by a 'flexible semi-solid transfer' (fst) process. *J. Micromech. Microeng.*, 14:932–940, 2004.
- [85] F. E. H. Tay, J. A. van Kan, F. Watt, and W. O. Choong. A novel micro-machining method for the fabrication of thick-film su-8 embedded micro-channels. *J. Micromech. Microeng.*, 11:27–32, 2001.
- [86] M. A. Roberts, J. S. Rossier, P. Bercier, and H. Girault. Uv laser machined polymer substrates for the development of microdiagnostic systems. *Anal. Chem.*, 69:2035–2042, 1997.
- [87] D. C. Duffy, J. C. McDonald, O. J. A. Schueller, and G. M. Whitesides. Rapid prototyping of microfluidic system in poly(dimethylsiloxane). *Anal. Chem.*, 70:4974–4984, 1998.
- [88] J. C. McDonald, D. C. Duffy, J. R. Anderson, D. T. Chiu, H. Wu, O. J. A. Schueller, and G. M. Whitesides. Fabrication of microfluidic systems in poly(dimethylsiloxane). *Electrophoresis*, 21:27–40, 2000.
- [89] S. K. Sia and G. M. Whitesides. Microfluidic devices fabricated in poly(dimethylsiloxane) for biological studies. *Electrophoresis*, 24:3563–3576, 2003.
- [90] J. O'Brien, P. J. Hughes, M. Brunet, B. O'Neill, and J. Alderman. Advanced photoresist technology for microsystems. *J. Micromech. Microeng.*, 11:353–358, 2001.
- [91] A. Daridon, V. Fascio, J. Lichtenberg, R. Wutrich, H. Langen, E. Verpoorte, and N. F. de Rooij. Multi-layer microfluidic glass chips for microanalytical applications. *Fresenius J. Anal. Chem.*, 371:261–269, 2001.
- [92] X. Li, T. Abe, and M. Esashi. Deep reactive ion etching of pyrex glass using sf<sub>6</sub> plasma. *Sensors and Actuators A*, 87:139–145, 2001.
- [93] M. Madou. *Fundamentals of Microfabrication*. 1st ed. Boca Raton, FL: CRC Press.
- [94] S. C. Jacobson, A. W. Moore, and J. M. Ramsey. Fused quartz substrates for microchip electrophoresis. *Anal. Chem.*, 67:2059–2063, 1995.
- [95] R. M. Guijt, E. Baltussen, G. van der Steen, J. Frank, H. A. H. Billiet, T. Schalkhammer, F. Laugere, M. J. Vellekoop, A. Berthold, P. M. Sarro, and G. W. K. van Dedem. Capillary electrophoresis with on-chip four-electrode capacitively coupled conductivity detection for application in bioanalysis. *Electrophoresis*, 22:2537–2541, 2001.

# Summary

There was an explosive growth in the bioprocess industry market during the last decade. The tight control of these processes is often very critical in order to optimize the process efficiency or even achieve the right product. Capillary Electrophoresis (CE) system is a good option for process monitoring and controlling, since it has already been proved to be a powerful analytical tool used in laboratory situations. However the extremely high separation voltage required by CE operation is preventing the system miniaturization and integration, and thus hindering its way to in-line application. Therefore, in this work, two low-voltage separation methods are proposed and investigated with the aim of substituting the conventional microfluidic CE. In the first DEP method, the curved parts of a serpentine channel are effectively used for dielectrophoretic separation. The second method “Moving Field CE” is basically an evolution version of the traditional CE, in which the required separation voltage is significantly reduced by decreasing the span of the electrodes in the channel.

For the DEP method, the curves are the essential parts where the dielectrophoretic separation takes place. A DC-biased AC electric field allows small particle separation in a curve as the dielectrophoresis is decoupled from the electroosmosis. The separation sensitivity was found to have a second order dependence on the ratio of AC to DC amplitudes and a linear dependence on the particle size. The separation resolution is limited by the Brownian motion and is voltage dependent. Since the curves are bended in the opposite directions, the separation will be wiped out in the next curve. Therefore, focusing must be conducted to bring all the particles to the same entering point for the next curve. In terms of focusing, the top-and-bottom electrode structure performs superior to the planar array for negative DEP because stronger electric field gradients are generated and particles are forced away from walls where nonuniform flow and nonspecific particle adhesion can occur. Because the hydrodynamic flow profile in a curve also decreases monotonously from the channel center to the outer sidewall, the same device can be used for both hydrodynamic and electrokinetic DEP separation. The hydrodynamic DEP, bearing a higher flow gradient, is expected to produce a larger separation than the electrokinetic DEP. The DEP device was fabricated by bonding of two processed substrates with an SU-8 layer sandwiched in bet-

ween. The retention time of 2  $\mu\text{m}$  and 4  $\mu\text{m}$  PS particles in a channel segment containing 4 curves was measured in the case of hydrodynamic DEP. The 4  $\mu\text{m}$  particles turn out to take an average 10% longer retention time than the 2  $\mu\text{m}$  particles, which proves the concept.

It was revealed that applying a DC voltage over a fraction of the channel will evoke flow distortion in moving field CE operation, and will in turn cause plug dispersion and peak broadening. For a given voltage, the smaller fraction it is applied on, the larger flow distortion will be caused in the EOF region. By extracting and analyzing the equivalent circuits of the fluid system, the flow distortion was found to be the consequence of a backward flow. The method we proposed is to generate, by coupling an electroosmotic pump (EOP), a forward flow and compensate the backward flow in the EOF segment. Specific pump structures were designed to relieve the driving voltage to the same level as the separation voltage. They are an array of slender channels and a broad thin channel. In order to minimize the flow loss, the channel arrays are proposed to be used in the injection channels as well to increase the flow resistance. The moving field CE prototype device was fabricated by laminating two layers of dry film resist on a processed glass substrate. The first layer is used to define the channel structure and the second acts as the lid of the channel. The flow distortion compensation was observed when the EOP driving voltage was increased to a certain level. The required EOP driving voltages with respect to different separation voltages were measured, which exhibit a linear relationship as expected.

To detect cells at extremely low concentrations, we additionally proposed a biomass concentration detection method in which an electrokinetic technology is used for rapidly increasing the concentration of the cells while measuring the concentration. Due to the dielectric contrast between the viable cell and the surrounding medium, the cells could be trapped and accumulated by positive dielectrophoresis. Based on the simplified homogeneous sphere model, the frequency dependence of the induced dipole strength of the yeast cell was studied by computer methods. The threshold DEP forces required to dominate over the Brownian motion for cell trapping were investigated. To achieve accurate and sensitive detection, a contactless 4-electrode conductivity detector was suggested to be used. Readout circuits and measurement setups were verified by using ideal resistors to mimic the environment of a liquid suspension. This method is recommended to be further investigated by using viable yeast cells in future research.

# Samenvatting

In de laatste 10 jaar is de bio-procesindustrie-markt explosief gegroeid. Een zeer nauwkeurige regeling van de daar gebruikte processen is veelal vereist om een goede proces optimalisatie te behalen en soms zelfs om het juiste product te verkrijgen. Capillaire Electroforese (CE) is een goede optie voor het in-line meten van de proceskwaliteit. In laboratorium situaties heeft het zich al bewezen als een krachtige analyse methode. De voor CE benodigde hoge scheidingsspanningen belemmeren de miniaturisatie en integratie en dus de toepassing voor in-line analyse. In dit werk worden twee laagspanningsscheidingsmethoden besproken die de conventionele micro-vloeistof CE kunnen vervangen. In de eerste diëlektrofores (DEP) methode, worden de gebogen secties van een serpentine vormig kanaal effectief gebruikt voor diëlektroforetische scheiding. De tweede methode, “Moving Field CE”, is in feite een doorontwikkeling van traditionele CE, waarbij de benodigde scheidingsspanning aanzienlijk is teruggebracht door de afstand tussen en het bereik van de actieve elektrodes te verkleinen.

In de DEP methode vormen de bochten de essentiële delen van het kanaal waar de diëlektroforetische scheiding plaats vindt. Een wisselend elektrisch veld voorzien van een kleine gelijkspanningscomponent maakt de scheiding van kleine deeltjes mogelijk omdat zo de diëlektroforese ontkoppeld wordt van de elektro-osmose. De scheidingsresolutie heeft een tweede-orde afhankelijkheid van de ratio tussen AC en DC amplitudes en varieert lineair met de deeltjes grootte. De resolutie wordt begrensd door de Brownse beweging en is afhankelijk van de scheidingsspanning. Omdat de bochten steeds in tegenovergestelde richting buigen, zou normaal gesproken de scheiding behaald in één bocht, in de volgende bocht weer teniet gedaan worden. Daarom worden door focusering alle deeltjes weer netjes naar hetzelfde entreepunt voor de volgende bocht geleid. De top-en-bodem elektrodeconfiguratie levert, voor negatieve DEP, een superieure focuseringskwaliteit t.o.v. de planaire configuratie omdat deze sterkere elektrisch veld gradiënten levert en de deeltjes weggedreven worden van de kanaalwanden waar niet uniforme stromingscondities en eventuele aanhechting van de deeltjes het proces kunnen verstoren. Omdat de hydrodynamische stroomsnelheid monotoon afneemt tussen de binnenwand en de buitenwand van de bocht kan hetzelfde apparaat zowel voor hydrodynamische als elektrokinetische DEP scheiding gebruikt worden. Naar

verwachting zal hydrodynamische DEP, die een grotere stromingsgradiënt vertoont, een betere scheiding opleveren dan elektrokinetische DEP. De DEP chip werd gefabriceerd door twee voorbereekte substraten d.m.v. een tussenliggende SU-8 laag, samen te voegen. Voor de hydrodynamische DEP situatie werden de doorlooptijden van de 2  $\mu\text{m}$  en 4  $\mu\text{m}$  polystyreen (PS) deeltjes over een kanaalsegment met 4 bochten gemeten. De 4  $\mu\text{m}$  PS deeltjes blijken gemiddeld een 10% langere doorlooptijd te hebben dan de 2  $\mu\text{m}$  deeltjes., waarmee dit concept beezen is.

In moving-field CE blijkt het aanleggen van een gelijkspanning over slechts een deel van het kanaal verstoring van het stromingsprofiel te veroorzaken, waardoor plugdispersie en detectiepiek-verbreding optreedt. Hoe kleiner de fractie van het kanaal waarover de spanning wordt aangelegd, hoe groter de verstoring. De verstoring blijkt het gevolg van tegendruk veroorzaakt door de stromingsweerstand van de spanningvrije delen van het kanaal, waardoor een additionele terugwaartse stroming ontstaat. Om dit effect te compenseren wordt voorgesteld om een elektro-osmotische pomp (EOP) toe te voegen die een extra stroming introduceert waarmee de terugwaartse stroming gecompenseerd kan worden waardoor weer een vlak stromingsprofiel verkregen wordt. Specifieke pompstructuren werden ontworpen zodat met een kleine pompspanning voldoende voorwaartse druk gegenereerd kan worden. Eén bestaat uit een array van smalle parallelle kanalen, de ander uit een breed dun kanaal. Om stromingsverlies via de injectiekanalen te minimaliseren kunnen deze structuren ook in deze kanalen opgenomen worden waarmee de weerstand van deze kanalen toeneemt. Het prototype van het moving-field CE apparaat werd gerealiseerd door twee lagen droge film fotolak te lamineren op een voorbereekt glassubstraat. De eerste laag wordt gebruikt om de kanalen te definiëren, de tweede laag dient om het kanaal aan de bovenkant af te sluiten. Compensatie van de verstoring van het stromingsprofiel werd aangetoond door de pompspanning langzaam op te voeren tot het juiste niveau. De benodigde pompspanningen werden gemeten bij verschillende scheidingsspanningen, waaruit een lineair verband tussen beide bleek, zoals verwacht.

Om extreem lage celconcentraties te meten wordt een biomassa concentratie detectie methode voorgesteld waarbij gebruik gemaakt wordt van een elektrokinetische technologie om snel celconcentraties lokaal te verhogen tijdens het meten. Door het diëlektrische contrast van levende cellen t.o.v. het omringende medium, kunnen cellen gevangen en verzameld worden d.m.v. positieve diëlektroforese. Gebaseerd op het simpele homogene bolmodel werd de frequentie-afhankelijkheid van de geïnduceerde dipool voor gistcellen gesimuleerd. De minimale DEP kracht nodig om de Brownse beweging te domineren werd bepaald. Voor een accurate en gevoelige detectie wordt een vierpunts contactloze geleidbaarheidsdetectie voorgesteld. Uitleescircuits en meetopstellingen werden geverifieerd m.b.v. ideale weerstanden die de omgeving van de vloeistofsuspensie nabootsten. Voorgesteld wordt om deze methode verder te onderzoeken aan een echte opstelling met levende gistcellen.



# Acknowledgements

This thesis could not have been accomplished without the assistance of many people, to whom I would like to express my gratitude.

First of all, I am heartily thankful to my supervisor Andre Bossche who accepted me to this laboratory and led me into the world of microfluidics. His constant scientific guidance and support were essential to me during the entire period of my research. He could always come up with new ideas, but he never imposed his ideas upon me. On the contrary, he gave me a lot of freedom to make decisions. He was very generous with his praises when I made progress, because of which my confidence and self-esteem were boosted. He was full of forgiveness and pardon when I made mistake, from which I learned what is mercy and generosity.

I am very thankful to my former colleague Peter Turmezei who passed on a lot of his simulation and fabrication knowledge to me at the beginning of my work.

My thanks also go to another former colleague Florin Tatar who worked as a postdoc on this project a couple of years ago and contributed a lot of effort to the development of moving field CE.

I would like to thank Prof. Paddy French for creating such a relaxing but inspiring laboratory environment for every student. I also thank him for his valuable suggestions on my proposition.

I am very grateful to Prof. Lina Sarro who gave me many advices on the device fabrication, and especially on the bonding process. I'm still regretting that I didn't talk to her earlier and more proactively.

My work in this laboratory would not have gone so smoothly without the technical support of Jeff Mollinger, Jeroen Bastemeijer, who helped me to solve the problems with my computer, network and measurements.

During my Ph.D. research I had a lot of collaboration and communication with people outside our lab. Thanks to the people from Aero and Hydrodynamics Group: Ralph Lindken for teaching me the PIV technique and offering me the free particles, Ulrich for help on images processing, and Vincent for information on chemical issues. Thanks to the people from Biotechnology Group: Prof. Peter Verhaert for teaching me biology and I would never forget the moment when

a professor freshen the drink for a Ph.D. student, Gert van der Steen for help on electrolyte preparation in spite of illness, and Herman for discussion on wafer bonding. Thanks to Gea Parikesit from Quantitative Imaging Group for providing me the distilled water. Thanks also to Marko Blom from Micronit for his helpful discussion on the fabrication.

I would like to thank all the people in DIMES. Special thanks to Bert for letting me work in cleanroom class 100, Charles for his constant smiling help, Silvana for the cleanroom course, Tom for the safety course, Wim and Ruud for help on wafer dicing, Hugo for help on metal sputtering, Alex and Cassan for letting me access MEMS lab, Jan and Jan Cornelis for help on mask fabrication, Mario for his clear and detailed explanation on equipments, Johan for lending me the injector, Henk for discussion on wafer bonding, Peter for teaching me CV measurement.

The work would not have been so pleasant if without my roommates. Thanks to Mohammad for sharing those funny Persian stories, Qinwen for all those relaxing chats, Hamed for help on data plotting, and the former roommate Dedy for friendly push on thesis writing.

I also wish to thank all past and present members of the Electronic Instrumentation Laboratory for their contribution to such a good working atmosphere. Special thanks to Oana, Sharma, Berenice, Luca, XiuJun, Guijie, Lukasz, Eduardo, Vijaye, CK, Lukas, Qi, Rong, Yue, Zili, Huaiwen, Sha, Ning, Caspar, Jiaming, Zhichao, Maureen, Zuyao, Gayathri, Ali. For administrative support, I would like to thank Willem, Joyice, Ilse, Inge and Trudie. I thank Piet for lending me the camera and the beamer, Ger for helping me on ISBN number application.

I express my thanks to all the committee members for spending time on my thesis review and for their important comments.

I would like to thank the Dutch Technical Foundation (STW) for the financial support.

Thanks go to Yuguang Yang for his valuable suggestions on the cover-page design.

I am also grateful for the support and friendship from my Chinese friends, which made me feel like at home. I'm afraid that the list might be too long and by fear of leaving someone out, I would simply say thank you very much to all of you.

Last but not the least, I would like to manifest my deep gratitude to my parents for their endless support and sacrificial love, and my beloved wife Jinghua who is the source of joy and the biggest spiritual pillar of mine.

*Lujun Zhang*  
*October, 2009*

*Delft, the Netherlands*

# List of Publications

## Patents

1. A. Bossche, F. Tatar and **L. Zhang**. Effective use of dielectrophoresis in serpentine micro-channels. Publication number: WO2008033009, Publication date: 2008-03-20.
2. A. Bossche, F. Tatar and **L. Zhang**. Moving field capillary electrophoresis with sample plug dispersion compensation. Publication number: WO20080-33021, Publication date: 2008-03-20.

## Journal papers

1. **L. Zhang**, F. Tatar, P. Turmezei, J. Bastemeijer, J.R. Mollinger, O. Piciu and A. Bossche. Continuous electrodeless dielectrophoretic separation in a circular channel. *Journal of Physics: Conference Series*, 34:527-532, 2006.
2. D.H.B. Wicaksono, **L. Zhang**, G. Pandraud, J.F.V. Vincent, and P.J. French. Fly's proprioception-inspired micromachined strain-sensing structure: idea, design, modeling and simulation, and comparison with experimental results. *Journal of Physics: Conference Series*, 34:336-341, 2006.
3. **L. Zhang** and A. Bossche. Fabrication of a microfluidic device with insulated electrodes on top and bottom sides of the channel. *Advanced Materials Research*, 74:183-186, 2009.
4. **L. Zhang** and A. Bossche. A novel dielectrophoresis-based batch separation in microfluidic devices aiming for in-line application. *Lab Chip*, submitted.
5. **L. Zhang** and A. Bossche. Flow distortion compensation for low-voltage moving field capillary electrophoresis application. *Sensors and Actuators B*, submitted.

## Book chapter

1. **L. Zhang**, J.R. Mollinger, J. Bastemeijer, A. Bossche. Microfluidic prototype fabrication in dry film resist. *MEMS Technology and Devices*, Pan Stanford Publishing, Singapore, pp. 414-417, June 2007, ISBN 978-981-270-960-8, ISBN 981-270-960-6.

## Conference proceedings

1. **L. Zhang**, F. Tatar, P. Turmezei, J. Bastemeijer, J.R. Mollinger, and A. Bossche. Particle separation by dielectrophoresis. *Proceedings of Annual Workshop on Semiconductor Advances for Future Electronics and Sensors (SAFE) 2005*, 17-18 November 2005, Veldhoven, the Netherlands, pp. 186-191.
2. **L. Zhang**, F. Tatar, J.R. Mollinger, A. Bossche. Continuous electrokinetic separation by electrodeless dielectrophoresis. *Proceedings of EUROSENSORS XX*, 17-20 September 2006, Goteborg, Sweden.
3. D.H.B. Wicaksono, **L-J. Zhang**, N. Gharbage, Y. Chen, J.F.V. Vincent, and P.J. French. Numerical modelling of biomimetics strain-sensing Microstructure. *Proceedings of EUROSENSORS XX*, 17-20 September 2006, Goteborg, Sweden, T2B-P13, pp. 1-4.
4. F. Tatar, P. Turmezei, **L. Zhang**, J.R. Mollinger, J. Bastemeijer, A. Bossche. Plug dispersion compensation technique in moving field capillary electrophoresis applications. *Proceedings of EUROSENSORS XX*, 17-20 September 2006, Goteborg, Sweden.
5. **L. Zhang**, F. Tatar, J.R. Mollinger, and A. Bossche. Design, Simulation and fabrication of a dielectrophoretic separation device using topographic channel structure. *Proceedings of the 5th Annual IEEE Conference on Sensors (IEEE SENSORS 2006)*, October 22-25, 2006, Daegu, Korea, pp. 435-438.
6. **L. Zhang**, F. Tatar and A. Bossche. High throughput continuous separation by electrodeless dielectrophoresis. *Proceedings of MiroTAS2006 Conference*, Nov. 5-9, 2006, Tokyo, Japan, pp. 909-911.
7. D.H.B. Wicaksono, N. Gharbage, **L-J. Zhang**, Y. Chen, and P.J. French. Influence of structural parameters on stress/strain amplification property of biomimetics membrane-in-recess Si microstructure. *Proceedings of Annual Workshop on Semiconductor Advances for Future Electronics and Sensors (SAFE) 2006*, 23-24 November 2006, Veldhoven, the Netherlands, pp. 398-403.

8. Y. Chen, D.H.B. Wicaksono, **L.-J. Zhang**, J.F.V. Vincent, and P.J. French. Strain amplifying property of bioinspired membrane-in-recess microstructure: analytical modelling. *Proceedings of Annual Workshop on Semiconductor Advances for Future Electronics and Sensors (SAFE) 2006*, 23-24 November 2006, Veldhoven, the Netherlands, pp. 373-378.
9. Y. Chen, D.H.B. Wicaksono, **L.-J. Zhang**, J.F.V. Vincent, and P.J. French. Preliminary study on the design of a silicon bio-inspired MEMS gyroscope. *Proceedings of Annual Workshop on Semiconductor Advances for Future Electronics and Sensors (SAFE) 2006*, 23-24 November 2006, Veldhoven, the Netherlands, pp. 379-383.
10. **L. Zhang** and A. Bossche. An investigation on the particle movement in the slanted planar electrode arrays. *Proceedings of the 4th Asia-Pacific Conference on Transducers and Micro-Nano Technology (APCOT 2008)*, 22-25 June 2008, Tainan, Taiwan.
11. **L. Zhang**, J. Bastemeijer, J.R. Mollinger and A. Bossche. Continuous dielectrophoretic separation in the iterative curves using dc-biased ac electric fields. *Proceedings of the 3rd IEEE International Conference on Nano/Micro Engineered and Molecular Systems (IEEE-NEMS 2008)*, 6-9 January 2008, Sanya, China, pp. 864-868.
12. **L. Zhang** and A. Bossche. Particle deflection in the electrode arrays by dielectrophoresis and ac electroosmosis. *Proceedings of EUROSENSORS XXII*, 07-10 September 2008, Dresden, Germany, pp. 321-324.
13. V.R.S.S. Mokkapati, O.M. Piciu, **L. Zhang**, J. Mollinger, J. Bastemeijer, A. Bossche. Lab-on-a-chip device for single cell analysis: trapping polystyrene beads. *Proceeding of APCTP-ASEAN Workshop on Advanced Materials Science and Nanotechnology (AMSN2008)*, 15-21 September 2008, Nha Trang, Vietnam, pp. 1-5.
14. V.R.S.S. Mokkapati, **L. Zhang**, J. Mollinger, J. Bastemeijer, A. Bossche. Fabrication of nanochannels with nearly-flat walls and embedded titanium nitride electrodes for nano-bio sensing. *Proceedings of the 19th MicroMechanics Europe Workshop (MME 2008)*, 28-30 September 2008, Aachen, Germany.
15. V.R.S.S. Mokkapati, O.M. Piciu, **L. Zhang**, J. Mollinger, J. Bastemeijer, A. Bossche. PDMS-glass bonded lab-on-a-chip device for single cell analysis. *Proceedings of the 7th International Conference on Advanced Semiconductor Devices and Microsystems (ASDAM 2008)*. 12C16 October 2008, Smolenice, Slovakia, pp. 211-214.
16. **L. Zhang**, R. Lindken and A. Bossche. Plug dispersion compensation for moving field capillary electrophoresis by low voltage electroosmotic pump.

- Proceedings of the 7th Annual IEEE Conference on Sensors (IEEE SENSORS 2008)*, 26-29 October 2008, Lecce, Italy, pp. 1175-1178.
17. V.R.S.S. Mokkalapati, O.M. Piciu, **L. Zhang**, J. Mollinger, J. Bastemeijer, A. Bossche. PDMS-glass bonded microfluidic device for single cell analysis: testing, alignment, bonding and trapping of polystyrene beads. *Proceedings of the 11th annual workshop on semiconductor advances for future electronics and sensors (SAFE 2008)*, 27-28 November 2008, Veldhoven, the Netherlands, pp. 415-419.
  18. V.R.S.S. Mokkalapati, **L. Zhang**, F. Postma, J. Bastemeijer, J. Mollinger, A. Bossche. Fabrication of a lab-on-a-chip device for single cell analysis using TMMF S2030. *Proceedings of the International Conference on MEMS (ICMEMS 2009)*. 3-5 January 2009, Chennai, India.
  19. **L. Zhang** and A. Bossche. Low voltage plug dispersion compensation for moving field capillary electrophoresis with flow loss via the side channels. *Proceedings of the 4th IEEE International Conference on Nano/Micro Engineered and Molecular Systems (IEEE-NEMS 2009)*, 5-8 January 2009, Shenzhen, China.
  20. V.R.S.S. Mokkalapati, **L. Zhang**, R. Hanfoug, J. Mollinger, J. Bastemeijer, A. Bossche. Fabrication and testing of a TMMF S2030 based micro fluidic device for single cell analysis. *Proceedings of the 3rd International Conference on Quantum, Nano and Micro Technologies (ICQNM 2009)*, 1-7 February 2009, Cancun, Mexico, pp. 86-89.
  21. **L. Zhang** and A. Bossche. A novel device for particle batch separation based on dielectrophoresis. *Proceedings of the 15th International Conference on Solid-State Sensors, Actuators and Microsystems (Transducers 2009)*, 21-25 June 2009, Denver, Colorado, USA.
  22. **L. Zhang**, J. Bastemeijer, J.R. Mollinger, and A. Bossche. Fabrication and experimental verification of a dielectrophoretic separation device. *Proceedings of the 8th Annual IEEE Conference on Sensors (IEEE SENSORS 2009)*, 25-28 October 2009, Christchurch, New Zealand.

# About the author

Lujun Zhang was born in Shanghai, China, in 1981. In 2003, he received his B.E. degree in Electronics and Information Technology from Tongji University, Shanghai. He moved to Stockholm, Sweden, in 2003 to follow his studies in Royal Institute of Technology. In 2005, he earned his M.Sc. degree in System-on-Chip Design from Royal Institute of Technology, Sweden. He spent the last 6 months of master studies doing thesis work at the Electronics Research Laboratory, Delft University of Technology, as an exchange student on the topic of "Design of an analog delay for an UWB autocorrelation receiver". In June 2005, he joined the Electronic Instrumentation Laboratory in Delft University of Technology as a Ph.D. student. His work focused on Microfluidics and Bio-MEMS, and his doctoral research project was the investigation of bioparticle separation in microfluidic devices for in-line application.